MASTER OF SCIENCE BY RESEARCH

Bird strike damage analysis on a model of a business jet composite wing leading edge

Ansari, Husain

Award date:
2016

Awarding institution:
Coventry University

Bird strike damage analysis on a model of a business jet composite wing leading edge

By

Husain Ansari

June 2016

Bird strike damage analysis on a model of a business jet composite wing leading edge

By

Husain Ansari

June 2016

A thesis submitted in partial fulfilment of the University's requirements for the Degree of Master of Research

Abstract

Bird strikes are issues as old as aviation dating back in 1912 and is still apparent in day-to-day aircraft incidents that costs revenue to the aerospace industries. Aircraft wing is one of the most critical components of aero structures, which provides support to the entire aircraft. In this study, a crash and impact analysis of a high velocity business aircraft composite wing leading edge has been performed with a numerical bird model using advanced simulation software LS-DYNA. The failure criteria are assessed using maximum stress theory and Chang-Chang failure criteria.

The numerical hemispherical-ended cylinder shape bird was modelled using Smooth Particle Hydrodynamics (SPH) method which is a meshless approach and gives the possibility of dealing with larger distortion compared to grid-based methods. The ribless leading edge of the wing was modelled in CATIA V5 and meshed with shell elements in Hyper Mesh. Glass Laminate Aluminium Reinforced Epoxy (GLARE), which is composed of several very thin layers of aluminium interspersed with layers of glass-fibre was used for the deformation analyses after impact. The layup of the GLARE was similar to the C-27J aircraft wing leading edge outboard layup and in the order of A/0/90/A/90/0/A where A is for Aluminium alloy 2024-T3 and 0/90/90/0 are the fiber orientations of the Glass-Fibre Reinforced Plastic (GFRP) also known as fiberglass. Johnson-Cook (MAT_015) material card was used for AL2024-T3 whereas Composite Damage (MAT_022) material card was used for GFRP to assess three failure modes - longitudinal tensile failure mode along the fiber, transverse tensile and compressive failure mode along the matrix. Two test cases were considered for the impact assessment – the first test case reflected the landing and take-off scenario in which the bird impact at 116 m/s, whereas the impact velocity of the bird was increased to 129 m/s in the second test case. The second test case results were compared with the theoretical and numerical result obtained from the C-27J aircraft certification. In both the test cases, all the fiberglass plies failed and the aluminium alloy plies plastically deformed but without the bird SPH particles penetration through the leading edge. The leading edge was able to absorb the impact energy but with permanent deformation.

Acknowledgments

First of all, I would like to thank Almighty Allah for His gracious and mercy. Secondly, I would like to thank my late mother who always appreciated my work and believed in me. I miss you mum. I would like to thank my father, who is also my mentor for being supportive, caring, and encouraging.

I would like to acknowledge my supervisor Jesper Christensen for his support and guidance. I am thankful to him for sharing his experience, ideas and orienting me in right direction. I am also grateful to aerospace staff members of the Delft University of Technology (Netherlands) for their collaboration and technical assistance related to bird strike and composites numerical modelling.

Last but not the least, I would like to extend my appreciation to all my friends for their moral support and advice.

Table of Contents

List of Figures

List of Tables

Abbreviations

Al	Aluminium
ALE	Arbitrary Lagrangian Eulerian
CAE	Computer Aided Engineering
CT	Computerised Tomography
DEM	Discrete Element Model
DICOM	Digital Imaging and Communications in Medicine
DOF	Degrees of Freedom
EASA	European Aviation Safety Agency
EOS	Equation of State
FAA	Federal Aviation Administration
FEA	Finite Element Analysis
FEM	Finite Element Method
FML	Fiber Metal Laminate
FRP	Fiber Reinforced Plastic
GFRP	Glass Fibre Reinforced Plastic
GLARE	Glass Laminate Aluminium Reinforced Epoxy
HCP	Hexagonal Close Packed
HG	Hourglass
ICAO	International Civil Aviation Organisation
IE	Internal Energy
J	Joules
JC	Johnson Cook
KE	Kinetic Energy
LE	Leading Edge
N	Newton
NACA	National Advisory Committee for Aeronautics
SPC	Single Point Constraints
SPH	Smooth Particle Hydrodynamics
TE	Total Energy
V_{FE}	Maximum flap extended speed
VM	Von Mises

This page is intentionally left blank.

1. Introduction

Bird strikes are issues as old as aviation dating back in 1912. During an exhibition flight over Long Beach in California, a gull lodged in the flight controls of Orville Wright powered aircraft that led to the death of Cal Rodgers, the first person to fly across USA (Early Aviators n.d.). On January 15th 2009, an US Airways Flight 1549 was ditched into Hudson River after experiencing loss of both turbines at an altitude of about 975m shortly after take-off caused by running into a flock of geese (CBS 2009). Bird strike significance as hazard has not yet diminished and this can be realised from both past and recent air accidents. During the period from 1912 to 1995 International Bird Strike committee has recorded a total of 42 fatal accidents killing 231 people and a total of 80 aircraft destroyed, which costs around $1.2 billion to the commercial aircrafts worldwide (Thorpe 2003, Allan and Orosz 2001). In UK itself, bird strikes are very common and there is at least one major incident every year. Although millions of pounds are spent each year to counter the threat, bird strikes still remain a regular occurrence according to Dr Rob Hunter, former pilot and head of flight safety at the British Airline Pilots Association (Smith 2012). Therefore, bird strike is a major threat to aircraft structures and aviation authorities require certain level of bird strike resistance certification test before operational use.

In past years, a common practice was to build a bird proof design of aircraft components and test, then redesign and test it again. This procedure was not only time consuming but also cost intensive. Numerical methods are put into practice for the purpose of rapid and optimised design, which has now steered the need to understand and evaluate the structural integrity of composite structures. Composite materials are increasingly being used for aircrafts primary structures such as wing components and fuselage panels, but have a major drawback of being vulnerable against transversal impact loads (Smojver and Ivancevic 2011). Hence, this study looks into the bird strike after impact behaviour on the composite structure as it is widely in use by the aerospace industries.

1.1 Project Aims and Objectives

Aircraft wing is one of the most critical structural components of an aircraft and impacts, including bird strikes can cause catastrophic failure. Therefore, the main aim

of this project is to investigate and analyse the effects of bird strike upon the structural integrity of an aircraft composite wing leading edge.

The project objectives are as follows:

1. Understanding the underpinning physics and mechanics behind bird strike scenarios.
2. Analyse and evaluate real world bird strike scenarios to determine the most influential factors/parameters that leads to composite structural failure; this will include the definition(s) of structural failure.
3. Based on point 1 and 2 above; create, correlate and verify a Finite Element (FE) model for advanced numerical analysis of bird strike scenarios and the associated damage on an aircraft composite wing structure.
4. Based on points 1, 2 and 3 define and conduct a series of case studies to determine and analyse the failure criteria on the composite wing structure.

1.2 Thesis Structure

Chapter 1 Introduction: A general introduction about the bird strike, use of composite materials in the aerospace industries and project aims and objectives.

Chapter 2 Background: Statistical analyses of bird strike on the aircraft categories and structural parts. Justification for the study of bird impact on high velocity business jet aircraft wing structure and the relevant EASA regulations. The chapter also briefly describes the use of KE as equivalence of bird strike impact energy followed by numerical method in CAE and use of LS-DYNA for this research.

Chapter 3 Literature Review: The chapter firstly describes the LS-DYNA explicit time integration loop and equations for crash and impact simulations, impact dynamics of the bird during impact and different numerical approach for the bird modelling. Secondly, it reviews the bird numerical model SPH governing equation, geometry, material and equations of state. Lastly it describes the wing materials that are used for the aircraft wing leading edge and the failure theories associated with composite materials.

Chapter 4 Methodology: The section describes the numerical modelling approach adopted for this research by firstly looking into different type of SPH mesh, the effect of SPH pitch values on the Hugoniot and stagnation pressure values and the wing shell element used for the simulations. Simulation setup section consists of material, contact, control and database cards defined for the two test cases.

Chapter 5 Simulation Results and Analyses: The section presents the results obtained from the composite wing leading for bird impact at 116m/s and 129m/s velocities.

Chapter 6 Conclusion and Recommendation: Detailed summary and conclusion from the study is stated in this chapter with recommendations for future work.

2. Background

2.1 Bird Strike on the Aircraft Categories

In aeronautical specifications, the term ‘bird strike’ means the collision between a bird and an aircraft. Due to remarkable increase in air traffic recently, the probability of an accident is higher especially in the airport area during take-off and landing which accounts for 48% and 30% of total accidents respectively (RGN 2014). Although numerous measures have been implemented by several airports across the globe to prevent bird strikes from occurring, it is still inevitable and the damage caused due to these collisions is catastrophic.

In order to evaluate the underpinning physics, it’s very important to firstly understand the type of aircraft / aircraft category that have the highest % of damage in an event of bird strike(s). According to RGN, an aviation news service, large transport aircrafts have the highest rate of reported bird strikes and it counts up to 186 per million flying hours (RGN 2014). Unfortunately, the bird strike data are not recorded around the world by ICAO (International Civil Aviation Organisation) and hence it’s not possible to validate the above statement as true for all the other countries. However, a report published by Atkins Limited (2003) on Bird Strike Damage & Windshield Bird Strike evaluated bird strikes that were reported from the year 1990 to 2007 covering countries such as US, Canada and UK in line with EASA aircraft classifications. In the report, a vibrant picture of the aircraft categories with % damage dependent on number of bird strikes was published and is shown in Table 1 which provides an adequate source for analysis.

Table 1 Aircraft classification related to bird strike damage (Atkins Limited 2003)

The above % damage was calculated by the damage caused to the overall aircraft including parts that were struck and non-functional. From the Table 1 statistics, it can be seen that CS-27 type small helicopters encountered the maximum percentage of damage (49.2%) but with least number of bird strikes i.e. 0.6% (65 strikes out of 10919 total strikes). Second highest percentage of damage, 34.6% was recorded for CS-23 type light aircraft with 12% of recorded strike. There were other aircraft subtypes under CS-23 category which suffered high percentages of damage such as 29.2%, 27.5% and 26.6% for total of 6.6% recorded strike. CS-25 type large transport aircraft had maximum number of strikes, 66.54% due to their size and flight altitude but with minimum damage (9.3%). One third of the strikes reported for CS-25 category aircraft involved multiple birds that resulted in twice the damage than a single strike (Atkins Limited 2003). Therefore, it can be concluded that CS-23 aircraft category (including propeller, jet, commuter and business jets) has comparatively low number of bird strikes compared to CS-25 aircraft category. Although CS-27 aircraft category such as helicopter has comparatively high damage percentage in comparison to CS-23 aircraft, helicopters usually fly at low altitude and speed than the light aircrafts.

Aviation Authorities such as Federal Aviation Administration (FAA) and European Aviation Safety Agency (EASA) introduced a certain level of bird strike resistance in certification tests for CS-25 category aircraft which is large turbine powered transport aircrafts; before they are allowed for operational use. EASA or FAR Part 23 requirement related to bird strike certification for CS-23 type aircraft that includes normal utility, acrobatic and commuter category aircrafts, and addresses only the windshield, windows and pitot tubes (JAR/FAR/CS-23.775). A nominal value for a single impact on a CS-23 type aircraft windshield is around 2lb (0.91 kg) which means the windshield should be able to withstand a 0.91 kg bird strike without penetration for a flap extended maximum speed approach (EASA Certification Memorandum 2012).

The requirements for CS-23 are less stringent than those of CS-25 category aircraft, which not only increases the personal risk to CS-23 aircraft occupants but also leads to economic losses in an event of catastrophic failure. High performance light aircraft such as business jets have high cruise speeds, and consequently the likelihood of severe damage resulting from a bird strike is greater. Therefore, this research

concentrates on damage caused by bird strikes on high speed business jets under CS-23 category. Author of this study performed a trade-off studies comparing light aircrafts such as Gulfstream, Piper, Cirrus and Cessna to identify high velocity aircraft which falls under CS-23 category and also commercially in use for passenger transportation. After comparison, Gulfstream G650ER shown in Figure 1 proved to be an appropriate choice for this study due to its high operating speed of Mach 0.925 (Gulfstream 2015).

Figure 1 Gulfstream G650ER business jet (Gulfstream 2015)

2.2 Bird Strike on the Aircraft Structures

A report published by Maragakis (2009) from EASA Safety Analysis and Research Department, evaluated bird population trends and their impact on Aviation Safety. Maragakis (2009) also investigated number of bird strikes from the year 1999 to 2008 and specified aircraft parts that are susceptible to bird strikes. Aircraft structures such as windshields, nose, wing and tail plane leading edge, antennas, engines and fuselage are more likely to get struck by bird and sustained damage as shown in Figure 2. Out of the documented strikes, three quarters of bird strikes are on wing and engine, whereas some forms of damage to the other aircraft parts (Boeing 2011).

Figure 2 Locations of bird strike damage (Boeing, 2011)

Although the report by Maragakis (2009) covered different trends of bird impact such as various altitudes and regions, it failed to remark the number of strikes that actually caused damage to these aircraft structures. Table 2 shows aircraft parts struck by birds in terms of number of strikes and the percentage of strikes that caused this damage.

Table 2 Percentage of strikes causing damage to specific aircraft part (Atkins Limited 2003)

Aircraft part with highest percentage of strike causing damage is navigation lights (71%) but for lowest number of recorded strikes (183 out of 14,104) i.e. 1.29%. The other parts that encountered high % of damage when struck are tail (30%) and wing/rotor (25%). One of the world's largest aero engine manufacturers, Rolls Royce already invested a huge capital to test simulated bird strike on its advanced lightweight carbon-titanium fan blades to mitigate the risks of engine failure in bird strike scenarios (Reuters 2014). Therefore, the focus of this study is on aircraft wing structure which has 25% of strikes causing damage out of the 3,006 (21%) total number of strikes recorded. There are currently no EASA certification test requirements for CS-23 aircraft category for bird strike resistance on an aircraft wing and hence recommendations are put forward as part of this study.

2.3 Aircraft Wing Structure

In order to understand the impact of bird strike on an aircraft wing, it is very important to recognise the aircraft wing components. Figure 3 shows internal structures of a general aircraft wing structure that consists of ribs, spar, stringers and skin. Each component of an aircraft wing has a basic function of transmitting and resisting the applied loads, providing an aerodynamic shape and also to protect the passengers and payload from in-flight environmental conditions. The forward and rear spars transverses the entire span of the wing, ribs provide the aerodynamic cross-section shape to the wing, and stringers offers additional support between the ribs to strengthen the outer skin that covers the wing (Megson 2007). Modern aircraft wings are much more complex because of other characteristics such as aspect ratio, wing sweep and chord variation along the span. Aircraft manufacturers do not publish the wing's sensitive information such as ribs aerofoil NACA number, stringer or spar dimensions in the public domain. Due to inaccessibility of all the G650ER aircraft wing internal structure specifications, this research focuses on a simplified ribless leading edge wing. This is not only used to numerically model and examine the after impact damage, but also for correlation and validation of the numerical results. The correlation and validation is achieved by comparison to publically available experimental test from Guida et al. (2013), which utilised a ribless leading edge with similar materials to those use in the numerical model. The leading edge aerofoil surface is derived from the available data of a predecessor aircraft type Gulfstream III and the detailed numerical approach is discussed in Section 4.2.

Figure 3 Aircraft wing internal structure (Nomenclaturo 2007)

2.4 Use of Kinetic Energy as equivalence of Bird Strike

Depending on the impactor speed and mass of the body, all the impact events are defined into three categories (Mithun and Mahesh 2012):

- Elastic impact
- Plastic impact and
- Hydrodynamic Impact

In low speed event where the generated stresses due to collision is lower than the material yield stress is termed as elastic impact. In this impact, the nature and duration of the impact depends on the material's elastic modulus and the elastic wave velocity. For a comparatively high speed impact, the stresses produced cause a plastic deformation of the target material and hence termed as plastic impact. For a higher velocity impact, the stresses generated by the deceleration of a projectile greatly exceeds the yield stress representing a fluid like behaviour and is termed as hydrodynamic impact. Bird impact falls under the hydrodynamic impact category where the material density dominates the behaviour instead of material strength (Mithun and Mahesh 2012). In this occurrence, bird does not bounce after the impact and this was substantiated by high-speed photographic studies by Schuette (1990) during his explicit numerical simulations of bird strike on a fan blade.

The damage on an impact depends on various factors such as the speed and altitude of the aircraft, mass of the bird and type of aircraft (light or transport). Some of the accidents involved bird masses above 0.78 kg that resulted into high kinetic energy impact (Atkins Limited 2003). The severity of damage has increased due to recent advancement in aircraft performance such as velocity and has led to augmentation of impulsive loads during the impact (Mithun and Mahesh 2012). The damage for aircraft flying over 800 ft. is also higher because it is dominated by heavier birds like Canada Geese and Turkey vultures (Atkins Limited 2003).

The certification requirement comprises of a bird mass and impact velocity that relates to energy of the collision between the bird and the aircraft. Assuming for simplicity that the bird does not deflect from the airframe, then the regulatory definition for this impact energy can be given by the equation (2.4.1).

$$KE = \frac{1}{2} mv^2 \quad (2.4.1)$$

where,

m is the bird mass and v is the true air speed of the aircraft

Kinetic Energy (KE) is a better indicator of damage likelihood than the bird mass because it takes aircraft speed into consideration, thereby makes it a useful safety indicator for aircraft certification requirements. Table 3 demonstrates the percentage damage to the wing or rotor for each aircraft category for a range of impact energy (KE in Joules). The total number of strikes for each case is presented in brackets.

Table 3 Kinetic Energy range for different aircraft categories (Atkins Limited 2003)

From the KE range statistics, it can be concluded that the CS-23 light aircraft category (within the red rectangular box), have the highest percentage of damage between 12.5% and 23.8% even for a low KE impact of less than 250 Joules. There is also increase in percentage of damage for higher KE values from 500 Joules to 10000 Joules; and in some cases 100% damage which is basically a catastrophic failure. Therefore, KE is considered as a safety indicator for this research and recommendations are based on the maximum KE range (Joules) the aircraft structure can withstand.

2.5 Numerical Method in CAE

In past years, it was a common practice for bird-proof design of aircraft components to be build and tested, then redesign and retested. It was not only a very time-consuming process but also a costly practice (Nizampatnam 2007). Computer Aided

Engineering (CAE) Driven Design Process has gained significant attraction in aerospace industries as it has proven to aid the new and inspiring designs, products with better quality and faster design. Figure 4 shows the change from traditional design process to the CAE Driven Design Process.

Figure 4 CAE driven design process (Altair 2012)

Comparing the above two processes, it can be seen that the CAE driven design process gives the flexibility of virtually testing and optimising the component before the actual build and test stage. The same principle is applied for this study, which means before building the actual bird strike proof design, the wing structure can be virtually tested to analyse the after impact behaviour and damage. The results obtained from these analyses can be later utilised to optimise the structure in order to minimise the impact. Consider bird strikes as an engineering problem where the quantitative approach is prioritised over the actual descriptive behaviour. In general, there are three methods to solve any engineering problem and are presented in Table 4.

Table 4 Methods to solve engineering problems

Analytical Method	Numerical Method	Experimental Method
Classical Approach which gives 100% accurate results if it's a closed form solution and applicable only for simple problems like cantilever and simply supported beams etc.	Mathematical representation which gives approximate results based on the assumptions. Applicable for real life complex problems even if a physical prototype is not available. Results obtained from this method must be validated by experiments and/or analytical method.	It gives precise result or actual measurements but time consuming and needs expensive set up. It is applicable only if physical prototype is available unlike numerical method. Results need to be validated by at least 3-5 tested prototypes.

Although the first theoretical bird strike investigations were based on pure analytical calculations, some of the complex problems such as different bird types, velocities and angle of impact are challenging to analyse using the analytical method (Cornell 1976). On the other hand, experimental method to perform number of tests using prototypes can be expensive and time consuming. Therefore, numerical method has been adopted by various aerospace industries and has proved beneficial in virtual tests and analyses of aircraft components and structures. In broad-spectrum, the numerical method consists of the following sub methods:

- Finite Element Method (FEM) – Linear, buckling, thermal, dynamic and fatigue analysis
- Boundary Element Method (BEM) – Acoustics, NVH (Noise, Vibration and Harness)
- Finite Volume Method (FVM) – CFD (Computational Fluid Dynamics) and Computational Electromagnetics
- Finite Difference Method (FDM) – Thermal and Fluid Flow Analysis (combination with FVM)

The finite element method (FEM) was adopted as a bird strike analysis tool in the late 1970s with pioneering work conducted by the US Air Force research laboratories (McCarty 1979). Therefore, FEM is adopted for this research to simulate bird strike impact and the results are validated with the help of experimental data.

2.6 Finite Element Method

Role of Finite Element Modelling has become a major part of today's aerospace market processes and this is because of the aerospace products development pace which is accelerating faster than ever. Looking at the general definition of FEM, it only makes calculations at a limited (finite) number of points and then interpolates the results for the entire domain (surface or volume). It involves the following steps (Strand7 2012):

- Dividing the structure into number of small regions (elements)
- Making an assumption about how the variables (example stress) can vary over a single element

- Assembling a matrix that accounts for the interaction between the nodes of the elements
- Solving the matrix to determine the overall response to the applied loads or boundary conditions

Simulation of bird striking an aircraft leading edge in which the impactor is highly deformed or fragmented as shown in Figure 5 is a major challenge for finite element codes, when it comes to fluid-structure interactions, non-linearity due to presence of high strain rates and large deformations.

Figure 5: Bird strike on an aircraft leading edge (Homebuilt Airplanes 2003)

Several commercial nonlinear explicit codes based on FEM are currently available such as LS-DYNA, PAM-CRASH, ABAQUS, DYTRAN, ANSYS, RADIOSS, which have the capabilities to include subsequent penetration of the bird inside the airframe following the initial impact. Heimbs (2011) published a journal article on computational methods for bird strike simulations, where he surveyed all of the above mentioned FEA software and is available in Appendix 1. From the survey, it can be determined that the majority of the numerical simulations were performed with LS-DYNA solver followed by ABAQUS and PAM CRASH. Therefore, for this research LS-DYNA solver is used to simulate the non-linear explicit bird strike impact on CS-23 aircraft category, G650ER composite wing leading edge model. The solver has different discretisation modelling approaches such as Lagrange, Eulerian, Smooth Particle Hydrodynamics, which have its relative advantages and disadvantages and is discussed in Section 3.

3. Literature Review

3.1 Bird Strike Simulation Time-step in LS-DYNA

As mentioned earlier in Section 2.6, there are many commercial finite element software (FEA) packages available in the market for analysing non-linear transient problems, which are used by various researchers and industries and the results have been proved to be a good indicator when compared to the experimental tests. Instead of developing another numerical algorithm for this project, a well-benchmarked commercially available FEA package LS-DYNA that provides combination of both explicit and implicit solvers is used. Implicit solver is basically used for static analysis where there is no effect of mass (inertia) or of damping. In dynamic analysis, not only nodal forces are associated with mass/inertia but also damping is included, and therefore both explicit and implicit solver can be used. Bird strike is a non-linear problem and in nonlinear implicit analysis, solution of each step requires a series of iterations to establish equilibrium. However, in explicit analysis no iteration is required as the nodal accelerations are solved directly. Explicit analysis handles nonlinearities with relative ease compared to implicit analysis. Explicit time integration solver loop in LS-DYNA is presented in Figure 6.

Figure 6 Explicit time integration loop in LS-DYNA (LSTC 2012)

From the Figure 6, it can be seen that the explicit computation solver is time-dependant and can be represented by Newton's Second Law:

$$[\mathrm{M}]\{\ddot{\mathrm{x}}\} + [\mathrm{K}]\{\mathrm{x}\} = \{\mathrm{f_{ex}}\} \quad (3.1.1)$$

Where,

M is the system mass

K is the stiffness matrix

$\ddot{\mathrm{x}}$ and x are the nodal accelerations and displacements respectively

$\mathrm{f_{ex}}$ is the external force vector

Equation (3.1.1) can be re-arranged in order to calculate the acceleration and eliminate the need to generate and invert large matrices (decoupled).

$$[\mathrm{M}]\{\ddot{\mathrm{x}}\} = \{\mathrm{f_{ex}}\} - [\mathrm{K}]\{\mathrm{x}\} = \{\mathrm{f_{ex}}\} - \{\mathrm{f_{in}}\} \quad (3.1.2)$$

During computation, step goes from n to n+1:

$$\{\ddot{\mathrm{x}}\}_{\mathrm{n+1}} = \frac{\{\mathrm{f_{ex}}\} - \{\mathrm{f_{in}}\}}{\mathrm{M}} \quad (3.1.3)$$

The time step size for the calculation increments is $\Delta\mathrm{t}$ as expressed by equation (3.1.4).

$$\Delta\mathrm{t} = \frac{\Delta\mathrm{t_{n+1}} - \Delta\mathrm{t_n}}{2} \quad (3.1.4)$$

The velocity $(\dot{\mathrm{x}})$ and displacement (x) are then evaluated with respect to timestep:

$$\dot{\mathrm{x}}_{\mathrm{n+\frac{1}{2}}} = \Delta\mathrm{t_n} \cdot \ddot{\mathrm{x}}_{\mathrm{n}} + \dot{\mathrm{x}}_{\mathrm{n-\frac{1}{2}}} \quad (3.1.5)$$

$$\mathrm{x_{n+1}} = \Delta\mathrm{t}_{\mathrm{n+\frac{1}{2}}} \cdot \dot{\mathrm{x}}_{\mathrm{n+\frac{1}{2}}} + \mathrm{x_n} \quad (3.1.6)$$

$\Delta\mathrm{t}$ is related to two physical properties of the numerical method, which are the speed of the stress wave travelling inside the structure (c) and length of the smallest element (l), and can be written as:

$$\Delta\mathrm{t} = \frac{\mathrm{l}}{\mathrm{C}} \quad (3.1.7)$$

C is the speed of the stress wave and its different for different element type. For example, beam element type has wave estimation as follows:

$$C = \pm\sqrt{\frac{E}{\rho}} \quad (3.1.8)$$

Where, E is Young's modulus and ρ is density.

Therefore, for explicit time integration to be stable, the time step size should be:

$$\Delta t \leq \frac{l}{C} \quad (3.1.9)$$

The maximum permissible time step is calculated considering the Courant-Friedrichs-Lewy (CFL) constraint for incompressible SPH expressed as:

$$\Delta t_{CFL} \leq 0.1\frac{h}{\|u\|_i} \quad \text{(Goswami and Pajarola 2011:21)} \quad (3.1.10)$$

Where,

0.1 is factor to ensure that the particle moves only a fraction (in this case 0.1) of the particle spacing h per time step

$\|u\|_i$ is the maximum particle velocity in the computation

By default, for crashworthiness problems to be stable, Δt is scaled by 90% but the scale factor changes according to the application (Bastien 2015). Bird strike can be considered as a ballistic problem and, therefore, scale factor should be 67% (default for high explosives). TSSFAC is the scale factor for computed time step and for all the simulations in this research is set to 0.67.

3.2 Bird Strike Test

Bird strike tests are performed in accordance with FAR Part 25 and the tests involves shooting of a bird typically dead or sedated chickens using a high powered gas cannon on the test article (aircraft structure) at a realistic operational velocity as displayed in Figure 7.

Figure 7: Fixture and scenario of a bird strike test. a) air cannon bore; b) velocity measure device; c) test article; d) high speed camera; e) test bed; f) safeguard screen; g) load cell (Guida 2008)

To evaluate the projectile (bird) behaviour after impact, it's important to initially understand the projectile response during the impact in terms of material strength and internal stresses. In Section 2.4, the three main categories of impact elastic, plastic and hydrodynamic have been discussed, but here the emphasis is on the projectile material strength and internal stresses. During an elastic impact, the impactor rebound as the internal stresses in the projectile are below the material strength. An increase of impact velocity causes internal stresses to exceed the projectile strength i.e. plastic response, which results into material density defining the response of the impactor and not the material strength. At impact velocity higher than the plastic response a fluid-like flow occurs, which can typically be observed in high-speed films of bird impact tests. Because of this fluid-like flow behaviour, the bird impactor is treated as 'soft-body' and experimental studies performed by Wilbeck

(1977) are utilised to assess this flow behaviour and pressure loads which are discussed in the next Section 3.3.

3.3 Bird Strike after Impact Behaviour

Because of the limited availability of experimental test data, majority of the studies use the experimental findings of Barber and Wilbeck from the late 1970s for numerical model validations (Heimbs 2011:2096). Wilbeck in 1977 at Wright-Patterson Air Force Base studied the low strength hydrodynamic model after impact behaviour. He used several impactor materials such as birds, gelatine and rubber, which were projected on a rigid plate as a target to validate the after impact fluid flow behaviour theory. The impact behaviour consists of four main phases and is shown in Figure 8.

Figure 8: Shock and release waves in soft body impactor (Heimbs 2011:2095)

(a) Initial shock wave when soft body with an initial velocity u_o hits the rigid target.
(b) Impact shock decays developing a significant pressure gradient which leads to an outward acceleration of the material particles thereby forming a release wave.
(c) The release waves cause a significant decrease in the pressure at the impact point and after several reflections of the release waves, the material flows steadily i.e. constant pressure and velocity.
(d) Pressure decay as shock wave trace is constantly weakened by the release waves.

The flow across the shock wave shown in Figure 8 can be numerically presented considering the process as one dimensional adiabatic and irreversible and is displayed in Figure 9.

Figure 9 One dimensional shock flow: a) shock propagation into fluid at rest, b) flow brought to a rest across the shock, c) standing shock (Wilbeck 1977:18)

Figure 9a represents a shock wave propagating into a fluid (bird) at rest, where u_s is defined as the velocity of the shock propagating into the bird at rest and u_p as the velocity of the particles behind the shock. It can also be determined that the particle velocity is actually the change in velocity across the shock. Figure 9b shows the velocities that are measured relative to the fluid in shocked state and the projectile's initial velocity u_o is brought to rest behind the shock. Figure 9c is steady state shock condition that is used to define the conservation laws across the shock. Therefore, from the Figure 9, the equations of conservation of mass (continuity) and momentum can be written as (Dar et al. 2013:4):

$$\rho_1 u_s = \rho_2 (u_s - u_p) \tag{3.3.1}$$

$$P_1 + \rho_1 u_s^2 = P_2 + \rho_2 (u_s - u_p)^2 \tag{3.3.2}$$

Equations (3.3.1) and (3.3.2) can be combined in order to find the pressure in the shocked region that is often referred to as the Hugoniot pressure (P_H) and is represented by equation (3.3.3).

$$P_H = P_2 - P_1 = \rho_1 u_s u_p \tag{3.3.3}$$

For the impact of a cylinder on a rigid plate, the velocity of the particle behind the shock is brought to rest i.e. $u_p = u_o$ and thus equation (3.3.3) can be written as:

$$P_H = \rho_1 u_s u_o \tag{3.3.4}$$

Equation (3.3.4) is used to find the theoretical Hugoniot pressure generated for any soft body impact, in which the shock pressure generated during the impact are much greater than the strength of the projectile, but less than the strength of the target. The shock velocity u_s is a function of impact velocity u_o and is obtained by solving the nonlinear equation (3.3.5) (Hedayati et al. 2014:262).

$$\frac{u_s}{u_s - u_o} = (1 - \alpha)\left(\frac{u_s u_o (4k-1)}{c_o^2}\right)^{-\frac{1}{4k-1}} \quad (3.3.5)$$

As seen in equation (3.3.5), c_o is the speed of sound in medium, k is an experimental constant, and α is the porosity of material (for example, $\alpha = 0.1$ for 10% porosity). The variation of shock velocity with respect to initial impact velocity for $\alpha = 0.1$ is given by Dar et al. (2013) and is presented in Figure 10. Although this shock velocity value can be substituted in the equation (3.3.4) to calculate the theoretical Hugoniot pressure, it is only valid for bird model with 10% porosity.

Figure 10 Shock velocity as function of impact velocity (Dar et al. 2013)

An alternative method to calculate shock velocity at different impact speed was proposed by Wilbeck (1977), which considers both particle velocity and speed of sound in water as shown in equation (3.3.6).

$$u_s = c_w + 2\,u_p \quad (3.3.6)$$

Where,

c_w is the normal sound speed in water and is 1482.9 m/s

u_p is the particle velocity

Barbar et al. (1978) found that the peak or Hugoniot pressures (P_H) generated by the bird impact against a rigid circular plate were independent of the bird size and consists of steady flow pressure towards the end as shown in Figure 11.

Figure 11: Pressure profile at the centre for normal soft body impact on a rigid plate (adapted from Wilbeck 1977)

This steady flow pressure, P_s can be calculated theoretically using the Bernoulli's equation, which is pressure being directly proportional to the square of the impact velocity and density of the bird and is given by equation (3.3.7).

$$P_s = \frac{1}{2}\rho_1 u_o^2 \qquad (3.3.7)$$

In a similar bird impact test on a rigid plate by McCarty (1980:843), pressure was applied as a uniform force over a specified area termed as 'bird impact footprint'. Although the uniform pressure vs. time curve result obtained from the bird impact in normal direction test ignored the initial peak pressure and tangential loads, the steady-flow pressure profile supported the Barbar et al. (1978) theory of stagnation pressure towards the end. However, there is a problem associated with the approach of applying pressure as a uniform force because Hugoniot pressure is largely dependent on the bird initial surface area contact. Section 3.4 further evaluates the development of bird strike simulation modelling approaches adopted in the recent years to mitigate the problem associated with the applied uniform force in order to obtain Hugoniot pressure.

3.4 Bird Strike Simulation Methods

Several bird strike simulations using computational methods have been produced in the past to simulate the real life bird strike problem. The first attempt to actually model the soft body impactor was in 1984 based on Lagrangian eight node solid elements that consisted of explicit time integration and mesh regeneration instead of applying pressure loads as discussed in Section 3.3 (Brockman 1984:6). Not only the explicit time integration was seen to be more appropriate for the transient bird strike problem than the implicit integration procedure but also mesh regeneration proved appropriate to avoid excessive mesh distortion (Heimbs 2011:2097). However, for the stability of explicit time integration, the time steps used were shorter than the smallest element of the model to allow the wave propagation in the smallest element (Martinez et al. 1995).

3.4.1 Lagrangian model and its applications for bird strike simulations

Lawson and Tuley (1987) adopted the Lagrangian elements approach in the early 1990s for the bird strike simulation on a Rolls Royce turbofan aero engine. The large wide chord fan blade of the aero engine was tested for its aerodynamic performance in an event of bird strike with Lagrangian element for the impactor in DYNA3D. The bird's slicing effect by the blade was simulated which achieved good agreements with their respective experimental tests (Mao, Meguid and Ng 2008:81). In the Lagrangian formulation, the mesh nodes are associated to the material and therefore each mesh node follows the material under motion and deformation as shown in Figure 12.

Figure 12: Lagrangian model (Heimbs 2011:2097)

The advantages and disadvantages associated with the Lagrangian formulation approach is discussed in Table 5.

Table 5 Lagrangian method advantages and disadvantages

Advantages	Disadvantages
Simplified boundary of the body because the boundary nodes remain on the material boundary.	Severe mesh deformations can introduce an artificial stiffening effect into the soft body finite element model affecting the impact pressure curve thereby leading to inaccurate results. Extensive compression of solid elements can lead to time step in explicit calculations drastically decrease, since the time step depends on the shortest element length in the model.

The flexibility of the mesh movements with the material under motion and deformation made Lagrangian a standard approach for bird impactor modelling in the 1990's. However, researchers' soon realised one of the major problems associated with the approach, which was severe mesh deformations. Several resolutions were put forward to solve the mesh distortion problem such as adaptive remeshing and element erosion but all came with a price of increased numerical errors and expensive computation (Hachenberg et al. 2003). Another problem associated with the Lagrangian approach was extensive compression of solid elements and is presented in Figure 13 for a bird strike impact on a rigid circular plate.

Figure 13: Bird strike simulation on a rigid circular plate with Lagrangian impactor (Heimbs 2011:2098)

The extensive compression of solid elements led to the increased surface area contact, which resulted into high impact on the rigid plate because of pressure loads. Although the problems associated with the Lagrangian method such as - large deformations of the elements, severe hour glassing and even error termination due to negative volume elements were known; the method was still used for bird impact simulations on aircraft windshields, engine fan blades, radomes, fuselage panels and leading edges of wind/tail plane until the evolution of Eulerian modelling technique (Heimbs 2011:2097-2098).

3.4.2 Eulerian model and its applications for bird strike simulations

The major limitation of reduced time steps due to excessive mesh distortion made Lagrangian modelling technique typically a good choice for solid materials but not for fluid-flow behaviour. In order to obtain a fluid like behaviour an alternative approach was adopted in the late 1990's and that was based on Eulerian formulation. In the Eulerian method, the material under study flows through the mesh while the mesh remains fixed as shown in Figure 14 (Huertas 2010).

Figure 14: Eulerian model (Heimbs 2011:2097)

Eulerian model solved the problem of severe mesh distortion but there were other problems associated with the approach. Table 6 discusses the Eulerian method advantages and disadvantages. To simulate a bird impact model using Eulerian method typically involves high number of elements with very small size in order to achieve accurate results. Due to element volume fractions and interactions it can also lead to dissipation and dispersion problems associated with the flux of mass between elements also known as numerical leakage (Heimbs 2011:2099).

Table 6 Eulerian method advantages and disadvantages

Advantages	Disadvantages
More stable than Lagrangian approach because the mesh does not move and hence excessive element deformation cannot occur.	The body's boundary condition is not well defined as the body moves within the mesh and depends on the mesh size.
Explicit time step is not influenced due to fixed mesh or mesh non-deformation.	The computation time with the Eulerian technique is much larger than the Lagrangian approach.

The high computation time in Eulerian model is due to mesh being fixed in space and this space covers both the regions where the material currently exists, and also the voids, where material may exist at a later time of interest and is displayed in Figure 15 (Simulia 2011:4).

Figure 15: Bird strike simulation on a rigid plate with Eulerian impactor (Heimbs 2011:2099)

In order to overcome the fixed mesh nodes problems associated with the Lagrangian approach, high computational time and numerical leakage problems associated with Eulerian approach; a hybrid approach was adopted called Arbitrary Lagrangian-Eulerian (ALE) formulation to make the simulations more efficient.

3.4.3 Hybrid Lagrangian Eulerian method and its applications for bird strike simulations

The first Arbitrary Eulerian Lagrangian (ALE) method with a moving Eulerian mesh was adopted in LS-DYNA software by Livermore Software Technology Corporation in the late 1990s. It was used for the first time in bird strike modelling and the results were compared with the fixed mesh, Eulerian model. In the ALE method, a bird is model with the Eulerian elements and enclose in a layer of void (vacuum). When the bird model hits the rigid plate modelled in Lagrangian elements, the mesh expands due to automatic mesh moving technique and is presented in Figure 16 (Olovsson and Souli 2000:42).

Figure 16: Bird strike simulation using ALE method (Heimbs 2011:2099)

ALE is similar to the Eulerian method except the surrounding Eulerian box, which moves and stretches if needed. As the background mesh can move in the same direction as the projectile and not fixed in space, number of elements required to model the bird impact simulations is significantly reduced, thereby solving the problem of high computation time. Hanssen et al. (2006) conducted both experimental and numerical bird strike studies using ALE approach on aluminium foam-based sandwich panels, and found that the coupled-field ALE method resulted in better agreement with Wilbeck (1977) experiments compared to both Lagrangian and Eulerian method when implemented separately. However, there are problems associated with Hybrid Eulerian-Lagrangian approach such as significant lateral expansion of the Eulerian box and accuracy of the results being strongly mesh dependent, and therefore requires fine meshes (Heimbs 2011:2100). These problems identified the need for Smooth Particle Hydrodynamics (SPH) method.

3.4.4 Smooth Particle Hydrodynamics (SPH) method and its applications for bird strike simulations

Smooth Particle Hydrodynamics (SPH) originally developed for simulating astrophysical problems, is a mesh-free Lagrangian method based on pseudo-particle interpolation theory and smoothing kernel functions compared to fixed mesh approach (Lucy 1977). The first SPH method adopted for bird strike simulation was documented in the early 2000s for a fan blade impact studies by Audic et al. (2000). In SPH method, each particle is essentially discretised and 'smoothed' over a finite volume of fixed mass. All these particles are independent from each other and are carried with the flow covering large deformations without the problem of mesh distortion as shown in Figure 17 (Shmotin et al. 2009). The hydrodynamic and other properties are evaluated at the particle positions and then calculated from weighted average of the values on other local particles (Cossins 2010).

Figure 17: Bird strike simulation using SPH model (Johnson and Holzapfel 2003:109)

A major advantage of the SPH method is its high stability. Due to absence of grid/mesh, this method allows solving many problems related to irregular geometry, large mesh deformation or tangling; which are hardly reproducible in other classical methods such as Lagrangian and Eulerian method. A disadvantage in SPH method is the demanding computation time both in memory and CPU. However, advancement in High Performance Computers (HPC) such as use of parallel analysis with more than one CPU can overcome the computation time problem.

Heimbs (2011) from European Aeronautic Defence and Space Company reviewed the development, characteristics and applications of different soft body impactor modelling methods using different solvers. For one of the benchmark tests, an experiment was performed with a 4 lb (1.81 kg) bird on a rigid plate at an impact angle of 30^{o}. In this experiment, five established bird modelling approaches were used namely:

- Lagrangian
- Classic Eulerian
- ALE (Arbitrary Lagrangian-Eulerian)
- SPH (Smooth Particle Hydrodynamics)
- DEM (Discrete Elements Model)

Out of these five approaches, SPH method was recommended for this benchmark test due to its good correlation with experimental observations for a slightly higher computational time than Lagrangian approach. DEM-based nodal mass model provided poor results due to lack of internal interaction and unrealistic behaviour of the bird, and hence it is not used for bird strike simulations (Heimbs 2011:2102). The accuracy of the SPH model was further evidenced by Guida et al. (2011) in an experimental test which was developed as a reference to validate the numerical simulation required for an aircraft certification. In this test, both Lagrangian and SPH method were adopted using two different explicit finite element software MSc-Dytran and LS-DYNA respectively to develop and validate a bird strike simulation methodology for the C-27J aircraft fin certification.

The experimental bird-strike test was conducted using a dead chicken of 8 lb (3.62 kg), which hit the composite leading edge bay of a C-27J aircraft at 250 knots (128.61 ≈129 m/s) speed. The results obtained from this experimental test was later used to validate the numerical model. The numerical model consisted of an assembly in FE software with leading edge as shell elements and rivets modelled in beam elements and is displayed in Figure 18. The composite material properties included aluminium alloy (Al2024-T3), core panel of honey-comb and Glass Laminate Aluminium Reinforced Epoxy (GLARE) cover plates. A right circular cylinder with hemispherical ends was used for the bird geometry and the bird length was equal to twice the diameter. The SPH model used in LS-DYNA was an elastic-plastic

hydrodynamic material with density equal to 923.7 kg/m^3 to replicate the after impact bird strike phenomena discussed in Section 3.3.

Figure 18: Leading edge FE model for C-27J aircraft certification (Guida et al. 2011)

The results obtained from the Lagrangian and SPH impactor at 2 ms and 3.6 ms from both the FEA softwares are shown in Figure 19 and Figure 20. The impact evolution can be evaluated and it can be seen that the aircraft structure deformation behaviour using the Lagrangian approach appeared to be in excellent agreement with the SPH model except the bird numerical model deformation.

Figure 19 Lagrangian model impact in MSc-DYTRAN at 2 ms and 3.6 ms (Guida et al. 2011:1068)

Figure 20 SPH model impact in LS-DYNA at 2 ms and 3.6 ms (Guida et al. 2011:1068)

From the Figure 19, the bird modelling in Lagrangian formulation deformed after it impacted the target and large FE mesh distortions can be seen but without the bird model breaking up into debris particle similar to fluid-like behaviour. In Figure 20, the numerical SPH bird model diffused around the structure and broke up into debris particle in a way similar to fluid-like behaviour discussed in Section 3.3. Therefore, it can be concluded that the Lagrangian approach is feasible only in the early stages of the impact. The numerical models were further compared and validated with the experimental test maximum deformation value of 305 mm at 3.6 ms. The maximum deformation obtained from the Lagrangian approach was 320 mm, whereas from SPH model was 297 mm as shown in Figure 21. SPH approach somehow underestimated the deformation but still it gave a more realistic level of damage and behaviour than the Lagrangian approach.

Figure 21 SPH model maximum deformation at 3.6 ms (Guida et al. 2011:1069)

Similar difference in the deformation by SPH approach was observed in another experimental test conducted by Georgiadis et al. (2008) on Bird-Strike Simulation for Boeing 787 Composite moveable trailing edge certification. A bi-phase material properties obtained from the manufacturer Hawker de Havilland was used to replicate the non-linear behaviour of a real composite material under in-plane and impact loading. Joints were modelled in the PAM-CRASH PLINK element, because of its improved and satisfactory representation of mechanically fastened joint in composite structure for crash and impact analysis. The tests were performed on the pre-production outboard flap measuring 10 metre in length at different bird velocities and using gel-pack bird. During the test, bird deformation was seen on the outboard flap and is shown in Figure 22. The bird after impact behaviour and the damage to the structure was similar to the test by Guida et al. (2011) discussed earlier.

Figure 22: Bird deformation during the test on an outboard flap - high speed video camera (above) and simulation (below) (Georgiadis et al. 2008:267)

The force-time data of the reaction loads both from numerical simulation and experimental test by Georgiadis et al. (2008) is shown in Figure 23. The force-time history result does not have any numerical values but can be used as a reference to comprehend the offset in impact forces obtained from SPH bird model. It can be seen that during the initial impact, the force produced by the SPH bird model impact on the structure matched with the experimental test. However, the measured reaction loads varied at midway where lower force can be seen for the numerical FE data. Towards the time end, the simulation reaction loads kept increasing in contrast to the experiment.

Figure 23 Force-time history of the reaction loads (Georgiadis et al. 2008:267)

SPH model depicted the loads on the target structure as well as kinematics of the event closely to the experimental result and hence it is considered as a good substitute to simulate the bird-strike scenario. However, in the above test the concentration was on PAM-CRASH software FEA model endorsement over traditional cannon ball tests. The difference in results can be further analysed by looking at the equation of state, bird geometry, mass distribution and velocity of the bird to evaluate the outcome of the different numerical modelling approaches currently in practice. The next Section 3.5 reviews the SPH governing equations followed by Section 3.6, bird geometry used for bird-strike simulations and differences in Hugoniot and steady pressure profiles obtained from the theoretical and experimental results.

3.5 SPH Governing Equations

Smooth Particle Hydrodynamics technique has its foundation in the interpolation theory, which represents fluid as a set of moving particles and the field variables of these particles are computed through interpolation of the neighbouring particles. The particles in the SPH method carry information about their both hydrodynamic and thermodynamic states. The nodes in SPH method are similar to nodes in a mesh except that these nodes can continuously deform and automatically distort to put more of the computational effort in relatively high density regions.

The moving particles in SPH method can be described as:

$$(\mathrm{r_i}(\mathrm{t}), \mathrm{m_i}(\mathrm{t}))_{\mathrm{i}\in\mathrm{P}} \qquad (3.5.1)$$

Where,
P is the set of moving particles,
$\mathrm{r_i}(\mathrm{t})$ is the location of particle i and
$\mathrm{m_i}(\mathrm{t})$ is the weight of the particle

The movement of each particle and the change of the weight is given by Guida (2008) and is shown by equation (3.5.2).

$$\frac{\mathrm{dm_i}}{\mathrm{dt}} = \nabla \cdot \mathrm{V}(\mathrm{r_i}, \mathrm{t})\mathrm{m_i} \qquad (3.5.2)$$

The quadrature formula can be written as:

$$\int_{\text{Space}} f(r)dr \approx \sum_{j\in P} m_j(t) f(r_j(t)) \quad (3.5.3)$$

The integral interpolant of any function $f(r)$ can be written as:

$$f(r) = \langle f(r)\rangle = \int_{\text{Space}} f(r_j) W(r_i - r_j, h) dr' \quad (3.5.4)$$

Where,
W is the kernel function,
r is a three-dimensional co-ordinate system ranging over a defined space
dr' is volume
h is the characteristic width or the smoothing length of the kernel

A useful concept in SPH is the smoothing kernel and the auxiliary B-spline function provides some good properties of regularity to this smoothing kernel expressed as:

$$W(r,h) = \frac{\sigma}{h^v}\begin{cases}\left(1 - \frac{3}{2}s^2 + \frac{3}{4}s^3\right), 0 \le s \le 1\\ \frac{1}{4}(2-s)^3, 1 \le s \le 2\\ 0, \text{ otherwise}\end{cases} \quad (3.5.5)$$

Where,

$s = \frac{r}{h}$, v is the number of dimension and σ is a normalisation constant

The above kernel function W is similar to a weight function and can be generalise with the smoothing length such that:

$$\lim_{h\to 0} W(r_i - r_j, h) = \delta(r_i - r_j) \quad (3.5.6)$$

$\delta(r)$ is the Dirac delta function and subject to normalisation as shown:

$$\int_{\text{Space}} W(r_i - r_j, h) dr' = 1 \quad (3.5.7)$$

However, for numerical computations the discrete kernel approximation of $f(r)$ can be represented in the continuous scalar field f at position r in the computational domain or space and written as:

$$f(r) \approx \sum_{j=1}^{N} \frac{m_j}{\rho_j} f(r_j) W(r_i - r_j, h) \quad (3.5.8)$$

Where,

$f(r_j)$, m_j, and $\rho_j = \rho(r_i)$ are the scalar value, mass and density of the j^{th} particle, and j ranges over all particles with the smoothing kernel. The equation (3.5.8) forms the basis of all SPH formulations and the mass density equation for this formulation is defined as:

$$\rho(r) = \sum_{j=1}^{N} m_j W(r_i - r_j, h) \quad (3.5.9)$$

Initially in the SPH method, the smoothing length was defined as a constant during the entire simulation. But, it was soon discovered that to have smoothing length dependent on the local number of particles is better and can be calculated by $h = h(r_i)$. In the formulation (3.5.8), each particle is assumed to be a small volume element and both density and mass of each element effects this smoothing kernel. Figure 24 shows the particle neighbourhood for SPH particle j inside a sphere of radius 2h. Within this circular neighbourhood, it is usually assumed that there is one SPH particle for an approximate spacing of the parameter h, which influences the overall density defined in equation (3.5.9) (Lacome 2001:10).

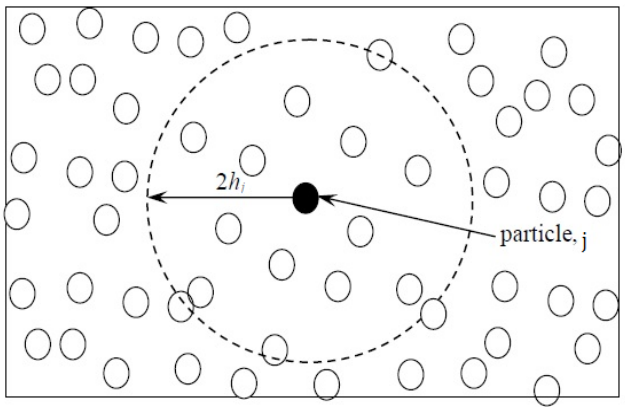

Figure 24 Particle neighbourhood for a SPH particle j inside a 2h radius sphere

3.6 SPH Bird Impactor Geometry

Although bird geometry is a very important aspect of numerical modelling, there are no standardised artificial bird shapes. The four most established bird impactor geometry substitutes are show in Figure 25. One of the main advantages of using such simple geometries is ease of manufacturing for both numerical simulation and experimental test and therefore have been used for many years.

Figure 25 Bird impactor geometries (Heimbs 2011:2103)

One of the first experimental bird-strike studies by Wilbeck (1977) was performed with cylindrical projectiles, which largely influenced the use of cylindrical bird impactor in the early development of numerical simulation. Nizampatnam (2007) investigated the influence of these four projectile geometries on the shock and stagnation pressures for a range of velocities and is shown in Figure 26 and Figure 27 respectively.

Figure 26 Effect of projectile shape on shock pressure (Nizampatnam 2007:99)

Figure 27 Effect of projectile shape on stagnation pressure (Nizampatnam 2007:99)

From the Figure 26 and Figure 27, it can be seen that the cylindrical and hemi-spherical cylinder have almost similar shock and steady state pressure results at low impact velocities. But at higher velocities, high shock pressures were observed for the cylindrical shape projectiles, which could be due to the large instantaneous surface area contact of the cylinder. On the other hand, the hemispherical cylinder shape projectiles shock and steady state pressures were closest to the experimental tests performed by Barber et al. (1978) and Wilbeck (1977). Although this justifies the reason for considering hemispherical-ended cylinder as a substitute for real bird, a more realistic bird model was constructed by Hedayati et al. (2014) to represent biometric data of a mallard bird in the numerical modelling. Over 1500 DICOM image slices were taken by the CT scan device to accurately model the numerical mallard bird shown in Figure 28. The initial model consisted of 49,302 SPH elements and each element with a mass 0.0162 g. When the cavities were implemented in the initial model, the resultant model consisted of 41,685 SPH elements with each element mass of 0.0191 g. The mass of each element was obtained by dividing the mallard bird total mass by the number of the SPH elements, and the approach is adopted for this study and explained later in Section 4.1.2.

Figure 28 Process of creating SPH particles in the central slice of mallard (a) DICOM image; (b) DICOM image after being checkered; (c) The SPH mallard model without cavities; (d) The SPH mallard model with cavities (Hedayati et al. 2014:263)

To obtain the pressure profile results at the centre of impact, a shell element connected to the target plate was used for the simulation. Pressure profiles from both hemispherical-ended cylinder and mallard model impacting from its tail side at various velocities were compared with Wilbeck (1977) and is shown in Figure 29.

Figure 29 Pressure profile at the centre of impact for initial velocities of (a) 116 m/s, (b) 225 m/s, and (c) 253 m/s (Hedayati et al. 2014)

From the Figure 29, it can be observed that for an initial velocity of 116m/s a maximum pressure of 90 MPa was imposed to the rigid plate by the hemispherical-ended cylinder bird model. Peak pressure of 42 MPa was imposed by the mallard model, which was nearer to the Wilbeck (1977) experimental result of 22 MPa. After the initial impact peak pressure, the mallard bird pressure profile correlated well with the experimental result compared to the hemispherical-ended cylinder. Similarly, for other velocities 225 m/s and 253 m/s, mallard bird model pressure profiles correlated well with the experimental results. Although the above shell element approach gives the pressure values, there are alternative ways to obtain these pressure profiles for the numerical simulation and are mentioned by Hedayati et al. (2014:264) as follows:

1. Obtain contact force diagram and then divide it by the contact area at any instant.
2. Obtain contact force diagram and then divide it by the initial cross section area of the bird.
3. Obtain the contact force diagram and then divide the force with the area of the sensor.

Out of these three methods to obtain pressure profiles for numerical simulations, the first two techniques also called as averaging, are not accurate because of the high pressure gradient at the centre than at the periphery. Hedayati et al. (2014) adopted the third method to obtain the pressure profiles in simulations and Figure 30 evaluates the Normalised Hugoniot pressure.

Figure 30 Normalised Hugoniot pressures (Hedayati et al. 2014: 265)

Figure 30 shows the hemispherical-ended cylinder model normalised Hugoniot pressure close to the theoretical values when the pressure was read from the shell sensors fixed to the rigid plate. Although both mallard and hemispherical-ended cylinder model results were close to the Wilbeck (1977) experimental value, the pressure for the hemispherical-ended cylinder model was calculated by averaging, which is not recommended. The Hugoniot pressure calculated from a FE model is an artificial way and the pressure is much higher (close to the theoretical value), whereas the pressure produced by an actual bird strike can be different. Johnson and Holzapfel (2003), Airoldi and Cacchione (2006), Liu et al. (2008), Meguid et al. (2008) in their finite element model used hemispherical-ended geometry as bird impactor and found that the model gives pressure reading near the theoretical values when read by sensor, but gives pressure reading close to the experimental values when calculated by averaging. Furthermore, numerical simulations using hemispherical-ended cylinder as bird geometry by McCarthy et al. (2005), Airoldi and Cacchione (2005) have given them satisfactory results for their studies.

Therefore, considering the complexity of the mallard bird FE model and its early stages of development, hemispherical-ended cylinder is adopted for this study as bird impactor geometry. Although the averaging method gave pressure reading close to the experimental values, the approach of dividing the contact force by the area at that particular instant of time is adopted for this study to obtain the pressure profiles close to theoretical values. In LS-DYNA, this can be performed using INTFOR card and is discussed briefly in Section 4.1.3. The next Section 3.7 discusses material properties and density of the numerical bird model.

3.7 SPH Bird Material

Different approaches for the bird impactor material can be found in numerous numerical models. In general, real birds are mostly composed of water with anatomic structure that includes internal cavities like bones, lungs and air sacs. But to implement these cavities in a bird impactor numerical model, a homogenised bird material with an average density between 900 and 950 kg/m^3 can be used. Furthermore, in several numerical simulations 10%-15% void have been used to give results fairly close to the experimental values (Airoldi and Cacchione 2006:1652, Heimbs 2011:2103). Nizampatnam (2007) in his study based on SPH bird impact simulations on a rigid target varied the material porosity between 0% and 40%, and found that a higher porosity of 30% - 40% agrees well with Wilbeck (1977) tests. Porosity and density of the material is largely dependent on the type of material card used in LS-DYNA and the two most common numerical bird impactor materials available are:

- Elastic- Plastic Hydrodynamic
- Null

3.7.1 Elastic-Plastic Hydrodynamic Material

As discussed in Section 2.4, at low pressure the bird behaves as an elastic-plastic material and the material type MAT_010 in LS-DYNA allows the modelling of it. The material basically considers the deviatoric stress which is linearly proportional to the rate of deformation and is defined in the equation (3.7.1).

$$\sigma_{ij} = 2\mu\varepsilon_{ij} \qquad (3.7.1)$$

where,
μ = dynamic viscosity of the bird material
ε_{ij}= deviatoric strain rate

If the yield stress and plastic hardening modulus are not defined in the material card, then the yield strength of the material can be calculated using the equation (3.7.2).

$$\sigma_y = \sigma_o + E_h\bar{\varepsilon}^p + (a_1 + pa_2)\max[p, 0] \qquad (3.7.2)$$

Where,
σ_o = yield stress

E_h = plastic hardening modulus dependent on E (Young's modulus), and

$$E_h = \frac{E_t E}{E - E_t} \quad (3.7.3)$$

E_t = Tangent Modulus
$\bar{\varepsilon}^p$ = effective plastic strain
p = pressure taken as positive in compression

Zhu, Tong and Wang (2009); Hachenberg, Graf and Leopold (2003) modelled the SPH bird using elastic-plastic hydrodynamic material with a defined failure strain of 16% - 18%. The material failed completely when the plastic strain reached beyond the defined limit and no fluid- like flow response was apparent, except at very low shear modulus (G). This type of material card is usually used for solid propellants or explosives when the shear modulus and yield strength are defined.

3.7.2 Null Material

Unlike Elastic-Plastic Hydrodynamic material type, null material allows equation of state to be considered without computing deviatoric stresses. Null material has no shear stiffness and also allows erosion in tension and compression which gives the fluid-like behaviour with no yield strength. As the bird model involves cavities, cut-off pressure should be defined to allow material numerically cavitate. Elastic-Plastic material generally resist dilatation at certain magnitude. On the contrary, null material with the cut-off pressure values set to a very small negative number can undergo dilatation without any resistance below this fixed negative value. In LS-DYNA, the null material is implemented by using MAT_009 material card with a suitable Equation of State (EOS) card.

Out of the two material types, null material (MAT_009) is used for this research as numerical bird material. It requires an EOS and its further discussed in Section 3.8.

3.8 SPH Bird Model Equation of State

The constitutive behaviour of the fluid-like materials is most commonly governed by hydrodynamic material models. Equation of State (EOS) is basically a thermodynamic equation of the homogenous material which defines the volumetric strength and does not undergo any chemical reactions or phase changes. This constitutive equation consists of pressure-volume relationship with water parameters at room temperature, thereby making it appropriate for bird numerical modelling as real birds consists of water and trapped air inside internal cavities. Comparison of the three most commonly and currently used EOS for null material SPH bird modeling are discussed in the Sections from 3.8.1 to 3.8.3.

3.8.1 Polynomial EOS

In several studies, polynomial form was used for bird strike simulations due to its simplicity and hence is one of the most popular equations of state. The pressure P of the bird model can be calculated using the equation (3.8.1).

$$P = C_0 + C_1\rho_d + C_2\rho_d^2 + C_3\rho_d^3 \text{ (Ensan et al. 2007:285)} \quad (3.8.1)$$

$C_{0,1,2,3}$ = material constants

$$\rho_d = \frac{\rho}{\rho_o} - 1 \quad (3.8.2)$$

ρ_d is dimension-less parameter and it is ratio of current density (ρ) to initial density (ρ_o)

The values used by Meguid, Mao and Ng (2008:490) to calculate the pressure using the equation (3.8.1) are as follows:

Table 7 Polynomial equation of state values

Parameters	Value
C_o	0
C_1	2323 MPa
C_2	5026 MPa
C_3	15180 MPa
ρ_o	934.3 kg/m^3

3.8.2 Gruneisen EOS

In studies by Hedayati and Ziaei (2013), and McCallum and Constantinou (2005), Gruneisen equation of state (also called v_s-v_p equation of state) was used. It describes a linear relationship between the shock and particle velocities and the equation that defines the pressure for compressed materials can be written as:

$$P = \frac{\rho_o c^2 \rho[1+\left(1-\frac{\gamma_0}{2}\right)\rho-\frac{a_e}{2}\rho^2}{[1-(S_1-1)\rho-S_2\frac{\rho^2}{\rho+1}-S_3\frac{\rho^3}{(\rho+1)^2}]^2} + (\gamma_0 + a_e\rho)E_i \quad (3.8.3)$$

Equation (3.8.4) represents the pressure for expanded material.

$$P = \rho_o c^2 \rho + (\gamma_0 + a\rho)E_i \quad (3.8.4)$$

where,
c = intercept of the shock (v_s) and particle (v_p) velocity curve
$S_{1\text{-}3}$ = coefficients of the slope of the v_s-v_p curve
γ_0 = Gruneisen gamma
ρ_o = material initial density
ρ = material final density
E_i = internal energy
a_e = experimental constants

Hedayati and Ziaei (2013) determined the following values for the Gruneisen equations (3.8.3) and (3.8.4):

Table 8 Gruneisen equation of state values

Parameters	Value
C	1480
S_1	1.92
$S_{2,3}$ and γ_0	0
ρ_o	938 kg/m^3

3.8.3 Murnaghan EOS

In other studies, by Kermanidis et al. (2005) and Liu, Li and Gao (2014), a simpler equation of state called Murnaghan was used. The Murnaghan equation to envisage the pressure can be written as:

$$P = P_o + B_m \left[\left(\frac{\rho}{\rho_o}\right)^{\gamma_m} - 1\right]$$ (Guo et al. 2012:675, Liu and Li 2013:927) (3.8.5)

where,
P_o= reference pressure
B_m and γ_m = material constants

Liu, Li, Gao and Yu (2014:547) determined the optimum values for γ as 7.14 and B as 9.3 GPa from his bird strike experiment on a flat plate.

All the three equations of state (3.8.1), (3.8.3) and (3.8.5) have one variable common, which is material constant(s) and it cannot be measured directly. Different commercial software can use either one or all formulations. Therefore, it often depends on the individual software codes, if the desired EOS can be implemented. Gruneisen EOS is valid only for solid material that remains in their solid state throughout the impact and according to Heimbs (2011:2104) should be used with care for bird strike simulations. Murnaghan EOS is currently unavailable in LS-DYNA and also not many experimental results are available, which could make the numerical model validation a difficult task. Therefore, for this study Polynomial EOS shown in equation (3.8.1) with material constants values from Table 7 is used.

3.9 Wing Material and Failure Criteria

Aircraft wing skins have traditionally been made out of metals and usually aluminium alloys; now however, aircraft engineers are increasingly working with composites. A composite material can be defined as a combination of two or more materials that results in better properties compared to that one material used individually. It has played a major part in aircraft total weight reduction by continuously striving to improve the lift to weight ratio making aerospace market as one of the largest and arguably the most important to the composites industry. Commercial and military aircraft, helicopters, business jets and spacecraft all make substantial use of composites, both inside and outside. In order to understand why composites are able to meet the aircraft structural integrity demands, it is firstly important to anticipate the aircraft structure requirements and its effects on the design which is discussed in Table 9.

Table 9 Features of aircraft structure (adapted from Nayak 2014)

From the Table 9, it can be concluded that the aerospace structural material requires a number of physical, mechanical and chemical properties. But the two main principle

characteristics that are significantly important for structural integrity are the stiffness and strength. Composite materials offer the capability of high degree of optimisation by tailoring the directional strength and stiffness. It also has the capability to mould large complex shapes in small cycle time reducing both part count and assembly time, and hence, is beneficial for thin-walled or curved construction (Nayak 2014). Because of all these reasons, composites are widely adopted by aerospace industries especially for aero structures.

Composites can be classified into two main constituents - reinforcement and matrix. Reinforced composite material consists of fiber such as glass, aramid and carbon, and is either continuous or discontinuous. Fibers have length much greater than its diameter and the ratio of length-to-diameter is known as aspect ratio that can vary greatly. Discontinuous fiber composites have fibers with low aspect ratio and randomly aligned, which dramatically reduces their strength and modulus. Continuous fibers have high aspect ratio, preferred orientation and possess high strength and stiffness due to far fewer defects (normally surface defects) in smaller diameter compared to the materials produced in bulk. The fewer defects of the fiber also plays a significant role in resisting impact by carrying most of the applied loads. However, this is often expensive due to the high manufacturing cost of the smaller diameter fiber (Kassapoglou 2010). The continuous phase is the matrix which can be a polymer, metal or ceramic. Polymers have low strength and stiffness, metals have intermediate strength and stiffness, but high ductility; whereas ceramics have high strength and stiffness but are brittle. The critical function of the matrix is to maintain the fibers in the suitable orientation and spacing while protecting them from abrasion and the environment. In polymer and metal matrix composites, the fiber and the matrix forms a strong bond, which is beneficial for the transmission of loads from the matrix to the fibers through shear loading at the interface. If the toughness is the main objective rather than the strength and stiffness, then a low interfacial bond can be obtained using ceramic matrix composites (Campbell 2010). As a conclusion, the reinforcing phase provides the strength and stiffness and in most cases are harder, stronger and stiffer than the matrix.

A laminated composite material can be defined as layers of at least two different materials that are bonded together. A lamina is a lay-up of either a single ply or plies

that are stacked in the same orientation, whereas plies that are stacked at various angles is called laminate. Difference in the lay-up between lamina and laminate is presented in Figure 31.

Figure 31 Lamina and laminate lay-ups (Campbell 2010)

3.9.1 Composite Materials Behaviour and Constitutive Equations

There are 5 different types of material behaviour - isotropic, transversely isotropic, orthotropic, monoclinic and anisotropic. Isotropic materials have identical properties in all directions, i.e. infinite planes of material property symmetry and typical examples are steel and aluminium. Transversely isotropic materials have identical in-plane material properties in one plane at every point and piezo-electric materials such as Barium-titanate is a good example. When materials have different properties in the 3 principle directions as well as 3 planes of material property symmetry, it is called Orthotropic and materials such as graphite and carbon demonstrate these characteristics. Monoclinic materials have different material properties in all directions except for 1 plane of symmetry and Zirconium oxide (ceramic) depicts this behaviour. Anisotropic materials have different material properties in all directions and natural material such as wood is a good example. Materials that retain any of

these five behaviours can be used in a laminate composite and hence it is important to understand the constitutive equations for the material deformation state.

In three dimensions, the normal and shear stresses on a material can be represented as displayed in Figure 32.

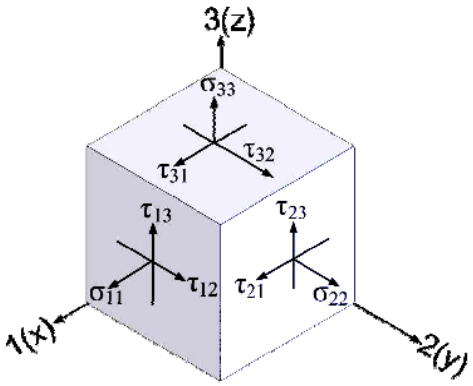

Figure 32 Normal and Shear stress

The engineering stresses and strains that describes the complete state of deformation are denoted in matrix forms as follows:

$$[\sigma_{11}\ \sigma_{22}\ \sigma_{33}\ \tau_{12}\ \ \tau_{23}\ \ \tau_{31}] \quad (3.9.1)$$

$$[\varepsilon_{11}\ \varepsilon_{22}\ \varepsilon_{33}\ \gamma_{12}\ \gamma_{23}\ \gamma_{31}] \quad (3.9.2)$$

In equation (3.9.1), the first three are the normal stresses and the last three are the shear stresses. In equation (3.9.2), the first three are normal strains and the last three are shear strains. Also from the equations (3.9.1) and (3.9.2), the following conditions hold true for the shear stresses and strains.

$$\tau_{12} = \tau_{21},\ \tau_{13} = \tau_{31},\ \tau_{23} = \tau_{32} \quad (3.9.3)$$

$$\gamma_{12} = \gamma_{21},\ \gamma_{13} = \gamma_{31},\ \gamma_{23} = \gamma_{32} \quad (3.9.4)$$

These stresses and strains are related through the generalised stress-strain relations also known as Hooke's law and can be represented in stiffness form as shown in equation (3.9.5).

$$\begin{Bmatrix} \sigma_{11} \\ \sigma_{22} \\ \sigma_{33} \\ \tau_{12} \\ \tau_{13} \\ \tau_{23} \end{Bmatrix} = \begin{bmatrix} E_{11} & E_{12} & E_{13} & E_{14} & E_{15} & E_{16} \\ E_{21} & E_{22} & E_{23} & E_{24} & E_{25} & E_{26} \\ E_{31} & E_{32} & E_{33} & E_{34} & E_{35} & E_{36} \\ E_{41} & E_{42} & E_{43} & E_{44} & E_{45} & E_{46} \\ E_{51} & E_{52} & E_{53} & E_{54} & E_{55} & E_{56} \\ E_{61} & E_{62} & E_{63} & E_{64} & E_{65} & E_{65} \end{bmatrix} \begin{Bmatrix} \varepsilon_{11} \\ \varepsilon_{22} \\ \varepsilon_{33} \\ \gamma_{12} \\ \gamma_{13} \\ \gamma_{23} \end{Bmatrix} \quad (3.9.5)$$

Looking at the equation (3.9.5), it can be concluded that there are 36 independent constants. The inverse of equation (3.9.5) expressing the strains in terms of the stresses via the compliance tensor S_{ij} is also often used and is shown in equation (3.9.6).

$$\begin{Bmatrix} \varepsilon_{11} \\ \varepsilon_{22} \\ \varepsilon_{33} \\ \gamma_{12} \\ \gamma_{13} \\ \gamma_{23} \end{Bmatrix} = \begin{bmatrix} S_{11} & S_{12} & S_{13} & S_{14} & S_{15} & S_{16} \\ S_{21} & S_{22} & S_{23} & S_{24} & S_{25} & S_{26} \\ S_{31} & S_{32} & S_{33} & S_{34} & S_{35} & S_{36} \\ S_{41} & S_{42} & S_{43} & S_{44} & S_{45} & S_{46} \\ S_{51} & S_{52} & S_{53} & S_{54} & S_{55} & S_{56} \\ S_{61} & S_{62} & S_{63} & S_{64} & S_{65} & S_{66} \end{bmatrix} \begin{Bmatrix} \sigma_{11} \\ \sigma_{22} \\ \sigma_{33} \\ \tau_{12} \\ \tau_{13} \\ \tau_{23} \end{Bmatrix} \quad (3.9.6)$$

The compliance matrix is the inverse of the stiffness matrix and is presented by equation (3.9.7).

$$[S] = [E]^{-1} \quad (3.9.7)$$

According to the theory of elasticity, conservative materials have strain energy density function and as a result of this function, the stiffness and compliance matrices are symmetric i.e. $S_{ij} = S_{ji}$. Thus for a general anisotropic body, there are 21 independent compliance constants, which are highlighted in the Figure 33.

This item has been removed due to 3rd Party Copyright. The unabridged version of the thesis can be viewed in the Lanchester Library Coventry University.

Figure 33 Compliance matrix in general (Christensen 2014)

Fully anisotropic materials have a very limited usage in engineering disciplines. For this study, orthotropic composite material is used and the shear–extension coupling terms are zero and is given by equation (3.9.8).

$$S_{14} = S_{15} = S_{16} = S_{24} = S_{25} = S_{26} = S_{34} = S_{35} = S_{36} = 0 \quad (3.9.8)$$

In addition to this, for an orthotropic body, shear stresses in one plane do not cause shear strains in another and is expressed in the equation (3.9.9).

$$S_{45} = S_{46} = S_{56} = 0 \quad (3.9.9)$$

With these simplifications, the compliant matrix is defined by 9 independent constants and is presented in Figure 34.

Figure 34 Compliance matrix for orthotropic materials (Christensen 2014)

Therefore, for this research, 9 constants mentioned in Table 10 are used to define the orthotropic material properties in LS-DYNA.

Table 10 Orthotropic material constants

Young's Moduli	E_{11}, E_{22}, E_{33}
Shear Moduli	G_{12}, G_{23}, G_{31}
Poisson's ratio	$\gamma_{12}, \gamma_{23}, \gamma_{31}$

3.9.2 GLARE Material Properties

One of the main challenges for the wing skin numerical modelling is to obtain the comprehensive material properties. Author of this study after searching through different journal articles and papers identified that for business jets such as Cirrus, Cessna and Liberty aircrafts wing skins are made from Glass-Fiber Reinforced Polymers (GFRP). The two types of glass fibers commonly used in the Fiber Reinforced Plastics (FRP) industries are E-glass and S-glass (Kumar et al. 2013:251). S-2 Glass with carbon/epoxy prepreg are used strategically for added stiffness and strength (Composites World 2015). Triumph currently manufactures the wing for Gulfstream G500 and G550 aircrafts - predecessors of G650ER. The upper wing skin for these aircrafts are made from a single sheet of machined aluminium using technique called age-creep forming (Triumph Group Inc 2015). GKN aerospace produces the upper and lower wing skins for the G650ER. The upper skin is produced without fasteners and joints to reduce its weight and maintenance, whereas lower wing skins incorporates several panels and complex design features (Aerospace-Technology 2015). There is no information provided by GKN on the materials used for either upper or lower wing skin. However, trends can be seen changing as companies are moving towards composites because it is lighter and exceeds the metals mechanical properties. Therefore, layer of glass fibre reinforced epoxy layers sandwiched between aerospace grade aluminium layers also known as GLARE is used for this study. The orientation of the layers is similar to the outboard layup used in C-27J aircraft and is displayed in Figure 35.

Figure 35 C-27J ribless wing leading edge configuration (Guida et al. 2013:107)

The outboard Fiber Metal Laminate (FML) layup consists of A/0/90/A/90/0/A, where A is referred to layer of aluminium alloy (2024-T3) with thickness of 0.3 mm and 0/90 are the glass/epoxy layer orientation (FM 94-27%-S2 Glass 187-460) with each glass

layer thickness of 0.125 mm, thereby total specimen thickness of 1.4 mm (Guida et al. 2013:107). The detailed mechanical properties for this outboard sheet (FML) is obtained from two journal articles, 'Certification by bird strike analysis on C-27J full-scale ribless composite leading edge' by Guida et al. (2013:109); and 'FEM simulation of a FML full scale aeronautic panel undergoing static load' by Citarella et al. (2014:3) and the values are populated in Table 11.

Table 11 Wing leading edge – GLARE material properties

	Aluminium Alloy 2024-T3		Glass Fabric (FM-94-27% - S2 Glass 187-460)
Young's Modulus, E	73,000 MPa	E_{11}	53,200 MPa
Poisson's ratio, ν	0.33	E_{22}	9,300 MPa
Shear Modulus, G	28,000 MPa	E_{33}	9,300 MPa
Density, ρ	2.7E-9 tonne/mm^3	ν_{12}	0.279
Yield Stress,σ_y	369 MPa	ν_{13}	0.279
Ultimate Tensile Strength, σ_{UTS}	516.6 MPa	ν_{23}	0.49
Failure Strain, ε_t	0.18	G_{12}	5,495 MPa
Bulk Modulus, K	71,000 MPa	G_{13}	5,495 MPa
		G_{23}	3,121 MPa
		Density, ρ	1.9 E-9 tonne/mm^3
		X_t	725 MPa
		X_c	725 MPa
		Y_t	75 MPa
		Y_c	75 MPa
		S	75 MPa

The residual strength of the laminate is directly related to the strain hardening capacity of the aluminium layers; higher the strain hardening, higher the residual strength (Vlot and Gunnink 2001:89). The strain-rate also effects the yield strength, hardening and ultimate tensile strength of the Al-2024 material and is shown in Figure 36. Several material cards are available in LS-DYNA to estimate the strain response of the metal under various loading rate. In this research, Johnson-Cook (JC) material card is adapted for Al-2024 to incorporate temperature sensitivity plasticity and cut off of element strength at high strain values. During impact, the strain rates vary over a large range and adiabatic temperature increases. Also material softening occurs due to this plastic heating, and thus, JC material card seemed suitable for this crash simulation.

Figure 36 Al-2024 stress vs strain curve for different strain rates (Ivancevic and Smojver 2011:16)

Johnson and Cook express the flow stress in terms of elastic plastic behaviour and is given by equation (3.9.10).

$$\sigma = (A_y + B_h \varepsilon_p^n)(1 + C_s \ln\left(\frac{\dot{\varepsilon}}{\dot{\varepsilon}_0}\right)(1 - T^{*m}) \quad (3.9.10)$$

where,

A_y = Yield Strength

B_h = Hardening Modulus

C_s = Strain rate sensitivity coefficient

n = hardening coefficient

m = thermal softening coefficient

ε_p = effective plastic strain and

T^* = homologous temperature = $\frac{T-T_{room}}{T_{melt}-T_{room}}$ (Martinez et al. 2011:821) (3.9.11)

Input values to calculate stress for the Al-2024 material using JC equation (3.9.10) is shown in Table 12.

Table 12 Aluminium Alloy 2024-T3 JC parameters (Buyuk et al. 2008)

3.9.3 Composite Laminate Strength and Failure Criteria

If the loads applied to a laminate are sufficiently high and exceeds the strength of the material, then the laminate tends to fails. For an orthotropic ply, the strength of the material varies with the fibre orientation and depending on the laminate lay-up and loading, damage may start at a load significantly lower than the load at which the final failure occurs. In order to predict the damage and how it evolves, requires individual modelling of the matrix and fibers. For a unidirectional ply, a simple uniaxial test which consists of longitudinal load in the direction of the fibre and transversal load on the matrix with pure shear but no shear coupling as shown in Figure 37 can identify the failure strengths.

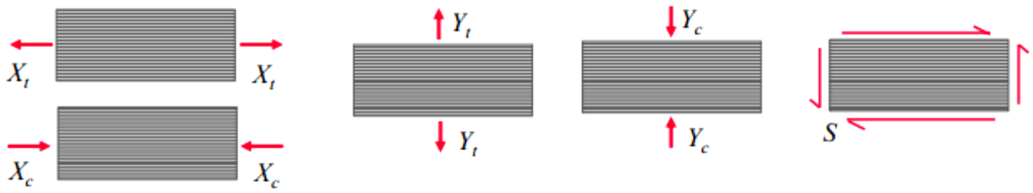

Figure 37 Failure modes in a unidirectional ply

where,

X_t: Strength symbol for tension failure along the fibers
X_c: Strength symbol for compression failure along the fibers
Y_t: Strength symbol for tension failure transverse to the fibers
Y_c: Strength symbol for compression failure transverse to the fibers
S: Strength symbol for pure shear failure of a ply

In this type of test, the damage usually starts in the form of a matrix crack between fibers in plies transverse to the primary load direction. The increase in load leads to increase in crack density which eventually lead to delamination, i.e. plies locally separate from one another or branch out to adjacent plies. Local stress concentrations can also lead to failure of the fiber-matrix interphase and the detailed analysis of damage creation and evolution that accounts for the individual constituents of a ply is a subject of micromechanics (Kassapoglou 2010:55). The situations become more complicated, when all the plies in a laminate do not have the same orientation. Hence, there are large number of failure criteria- stress-based, strain-based, or energy based, which can predict the failure. Below are the six most commonly used lamina(e) failure criteria which are briefly discussed in the subsections from 3.9.3.1 to 3.9.3.5:

- Maximum stress failure criterion
- Maximum strain failure criterion
- Tsai-Hill failure criterion (adaption of VM yield criterion)
- Tsai-Wu tensor failure criterion
- Chang and Chang failure criteria

3.9.3.1 Maximum Stress Failure Theory

In this case, the principal stresses in each ply are compared with their corresponding strength values X_t, X_c, Y_t, Y_c, and S discussed earlier in the Section 3.9.3. A ply would fail if any of the five conditions mentioned below are satisfied:

For tensile stress,

$$\sigma_{11} \geq X_t \text{ and } \sigma_{22} \geq Y_t \quad (3.9.12)$$

For compressive stress,

$$\sigma_{11} \geq X_c \text{ and } \sigma_{22} \geq Y_c \quad (3.9.13)$$

For shear stress,

$$|\tau_{12}| \geq S \quad (3.9.14)$$

In the equation (3.9.14) it can be noted that sign of the shear stress is irrelevant, because its magnitude is compared with the allowable shear, S (Kassapoglou

2010:57). This failure criterion is simple to use without any additional testing requirements. However, the stress must be converged to principal stress and there should not be any coupling between values (Christensen 2014).

3.9.3.2 Maximum Strain Failure Theory

The maximum strain failure theory is in a manner analogous to the maximum stress failure theory. The ply would fail if any of the following five conditions are satisfied:

For tensile strain,

$$\varepsilon_{11} \geq \varepsilon_{Xt} \text{ and } \varepsilon_{22} \geq \varepsilon_{Yt} \quad (3.9.15)$$

For compressive strain,

$$\varepsilon_{11} \geq \varepsilon_{Xc} \text{ and } \varepsilon_{22} \geq \varepsilon_{Yc} \quad (3.9.16)$$

For shear strain,

$$|\gamma_{12}| \geq \varepsilon_{S} \quad (3.9.17)$$

Where,

ε_{11} = stress in material axis 1
ε_{22} = strain in material axis 2
γ_{12} = shear strain in plane 1-2
ε_{Xt} = longitudinal tensile strain in material axis 1
ε_{Yt} = longitudinal tensile strain in material axis 2
ε_{Xc} = longitudinal compressive strain in material axis 1
ε_{Yc} = longitudinal compressive strain in material axis 2
ε_{S} = shear strain

3.9.3.3 Tsai-Hill Failure Theory

The two failure criteria mentioned in subsection (3.9.3.1) and (3.9.3.2) are dependent either on stress or strain, and are individually compared with its respective allowable constituents. A major drawback in these theories is that both stress and strain may interact with each other and lead to failure; even though when compared individually with its respective allowable suggest that there is no failure (Kassapoglou 2010:57). Based on von Mises yield criterion in isotropic materials (expressed by equation

3.9.18), Hill was among the first to suggest a combined failure criterion for composite materials.

$$\frac{\sigma_{11}^2}{\sigma_{yield}^2} + \frac{\sigma_{22}^2}{\sigma_{yield}^2} - \frac{\sigma_{11}\sigma_{22}}{\sigma_{yield}^2} + \frac{3\tau_{12}^2}{\sigma_{yield}^2} = 1 \quad (3.9.18)$$

Where,

σ_{yield} is the material yield strength

Hill's failure criterion is a three dimensional state of stress which is a model of yielding in anisotropic materials and is given by equation (3.9.19).

$$F_{11}\sigma_{11}^2 + F_{22}\sigma_{22}^2 + F_{12}\sigma_{11}\sigma_{22} + F_s\tau_{12}^2 = 1 \quad (3.9.19)$$

Tsai determined the stress coefficients in equation (3.9.19) considering simple loading situations, where σ_{11}, σ_{22} and τ_{12} acts on a ply with corresponding strength X, Y, and S respectively as follows:

$$\sigma_{11}^2 = X^2 \quad (3.9.20)$$

$$\sigma_{22}^2 = Y^2 \quad (3.9.21)$$

$$\tau_{12}^2 = S^2 \quad (3.9.22)$$

Consider that only σ_{11} is acting parallel to the fibers, equations (3.9.19) and (3.9.20) can be linked and it can be established that:

$$F_{11} = \frac{1}{X^2} \quad (3.9.23)$$

If all the cases are considered, then the final form of the Tsai-Hill failure criterion is expressed by equation (3.9.24) and the failure would occur if the condition is satisfied.

$$\frac{\sigma_{11}^2}{X^2} + \frac{\sigma_{22}^2}{Y^2} - \frac{\sigma_{11}\sigma_{22}}{X^2} + \frac{\tau_{12}^2}{S^2} \geq 1 \quad (3.9.24)$$

3.9.3.4 Tsai-Wu Failure Theory

Tsai- Wu failure theory is not entirely based on physical phenomena but an attempt to mathematically generalise the Tsai-Hill failure criterion. It is created on a curve fit based on tensor theory and the fact that composites have different strengths in tension and compression (Kassapoglou 2010:58). Tsai-Wu includes corresponding tensile and compressive strengths that predicts the range from acceptable to excellent compared to other failure criteria. This failure criterion can indicate the ply failure but not the modes of failure, and therefore should be viewed as a useful curve fit more than a physical-based model of failure. The failure would occur only if the following condition is satisfied:

$$\frac{\sigma_{22}^2}{X_t X_c} + \frac{\sigma_{22}^2}{Y_t Y_c} - \sqrt{\frac{1}{X_t X_c}\frac{1}{Y_t Y_c}}\,\sigma_{11}\sigma_{22} + \left(\frac{1}{X_t} - \frac{1}{X_c}\right)\sigma_{11} + \left(\frac{1}{Y_t} - \frac{1}{Y_c}\right)\sigma_{22} + \frac{\tau_{12}^2}{S^2} \geq 1 \qquad (3.9.25)$$

3.9.3.5 Chang and Chang Failure Theory

The Tsai-Wu failure criterion is a quadratic stress-based global failure prediction equation, which is relatively simple to use but does not specifically consider the failure modes observed in composite materials (Zarei 2008:80). Chang and Chang modified the Hashin failure criterion to include the non-linear shear stress-strain behaviour of a composite lamina. Tsai-Wu failure criterion is widely used for composite lamina subjected to soft body impacts because it consists of fiber and matrix failure modes in both tension and compression (Ensan et al. 2007). The failure would occur if any one of the conditions stated from equation (3.9.26) to (3.9.29) is met.

For the tensile fibre mode if $\sigma_{11} > 0$ then:

$$\left(\frac{\sigma_{11}}{X_t}\right)^2 + \left(\frac{\sigma_{12}}{S_{12}}\right)^2 \geq 1 \qquad (3.9.26)$$

For the compressive fiber mode if $\sigma_{11} < 0$ then:

$$\left(\frac{\sigma_{11}}{X_c}\right)^2 \geq 1 \qquad (3.9.27)$$

For the tensile matrix mode if $\sigma_{22} > 0$ then:

$$\left(\frac{\sigma_{22}}{Y_t}\right)^2 + \left(\frac{\sigma_{12}}{S_{12}}\right)^2 \geq 1 \qquad (3.9.28)$$

For the compressive matrix mode if $\sigma_{22} < 0$ then:

$$\left(\frac{\sigma_{22}}{2S_{12}}\right)^2 + \left[\left(\frac{Y_c}{2S_{12}}\right)^2 - 1\right]\frac{\sigma_{22}}{Y_c} + \left(\frac{\sigma_{12}}{S_{12}}\right)^2 \geq 1 \quad (3.9.29)$$

Comparing all the above five failure criteria, it can be concluded that maximum stress failure theory can be easily implemented and the results does not require any further convergence. But maximum stress failure theory does not provide failure either of fiber or matrix, and therefore Chang-Chang failure theory is also adopted for this study to assess the composite leading edge damage after bird impact. In LS-DYNA, Chang-Chang failure is executed using MAT_022 COMPOSITE DAMAGE material card and is further discussed in Section 4.2.

4. Methodology

This section explains the methodology adopted for this study such as bird and wing numerical modelling, simulation setup and settings used for the two test cases.

4.1 Bird Numerical Model

4.1.1 Bird Dimension

As mentioned in the Section 3.6, the bird geometry selected for this research is hemispherical-ended cylinder. Currently there is no EASA certification requirements for bird impact on a CS-23 category (business jet) wing leading edge, and therefore, no specific bird mass is endorsed. However, for this study, bird mass is assumed to be 4 lb (1.81 kg) to compare the results with the Wilbeck (1977) experiments. The International Bird Strike Research Group studied biometric data of different bird species and proposed relationships in order to increase the accuracy of numerical bird model. Equations (4.1.1) and (4.1.2) shows these relationships in terms of bird density and diameter with respect to mass.

$$\rho = -0.063 \text{ x } \log_{10}\text{m} + 1.148 \quad (4.1.1)$$

$$\log_{10}\text{D} = 0.335 \text{ x } \log_{10}\text{m} + 0.900 \quad (4.1.2)$$

where,
m = mass of the bird in grams
ρ = density of the bird in g/cm^3
D = bird body diameter in mm

Using the equations (4.1.1) and (4.1.2), density and diameter of the bird is calculated to be 942.77 kg/m^3 and 0.098 m respectively. Several researchers including Tudor (1968) measured the density of various chicken that are used for bird strike experiments; and found it approximately 1,060 kg/m^3 (without porosity) and with 10% porosity is 950 kg/m^3. However, Wilbeck (1977:115) expressed that chickens can be better approximated by a material with original density of 950 kg/m^3 and without porosity. Therefore, the author of this study selected the bird numerical model density of 950 kg/m^3 rather than 942.77 kg/m^3 in order to validate the results with Wilbeck experimental tests. The straight cylinder length of the numerical bird model is

calculated using the equation (4.1.3) from Walvekar (2007:16) and Australian Transport Safety Bureau (2002:43) and is 0.189 mm.

$$\text{Straight Cylinder Length} = 4 \cdot \left(\frac{\text{Mass}}{\pi \cdot \text{Density} \cdot \text{Diameter}^2} - \frac{\text{Diameter}}{6} \right) \quad (4.1.3)$$

Figure 38 shows the total length of the bird model, which is 0.287 m (287 mm) and consists of hemisphere ends at each end and straight cylinder.

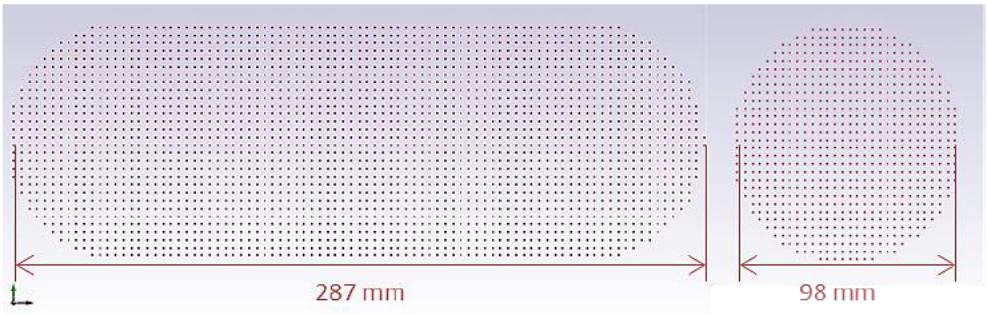

Figure 38 SPH bird model dimensions

The bird physical and material properties are summarised in Table 13.

Table 13 Bird numerical model properties

Properties	Notation	Value
Mass	m	1.81 kg
Density	ρ	950 kg/m^3
Diameter	D	0.098 m
Length	L	0.287 m

4.1.2 SPH Meshing

SPH method in HyperMesh also known as Finite Point Method (FPM) is a technique used for numerical simulation to analyse the bodies that does not have high cohesive forces among themselves and undergo large deformation. The input panel to create SPH mesh using HyperMesh is shown in Figure 39.

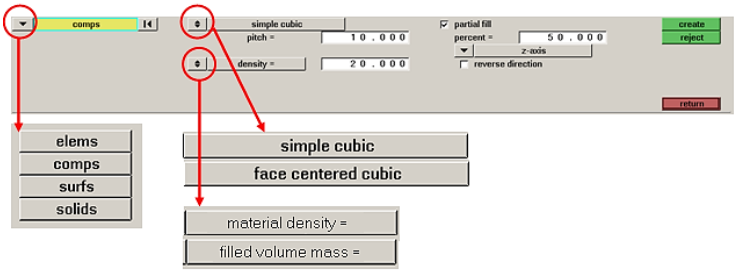

Figure 39 SPH mesh input panel (Altair 2014)

The bird geometry created in CATIA V5 was imported as a single component and meshed using the SPH panel. The particles in SPH meshing are distributed through either simple cubic or face centered cubic (FCC). The difference between the simple cubic and FCC is shown in Figure 40.

Figure 40 SPH mesh - a) simple cubic, b) FCC (Altair 2014)

The data for SPH mesh adopted by various researchers for bird strike simulations was inaccessible, and therefore, it is difficult to justify whether simple cubic or face centered cubic mesh method can give satisfactory results. An evaluation to identify the difference between the two mesh methods is performed by the author of this study. Bird geometry of 287 mm in length and 98 mm in dimension was meshed with a pitch distance of 3.8 mm and filled volume mass of 1.81 kg (100% filled volume and no porosity). The difference in the number of SPH particles with each particle mass is presented in Table 14.

Table 14 SPH element generation

Mesh Mode	Total Number of elements	Mass of each element (kg)	Overall Mass (kg)
Simple Cubic	34018	5.32071E-5	1.81
Face Centered Cubic (FCC)	44315	4.0843958E-5	1.81

From the Table 14, it can be concluded that the FCC method generates more number of elements with reduced mass of each SPH element compared to simple cubic method for the same geometry, pitch and mass. The overall mass of the numerical model from both methods remain the same, because they are governed by the equation (4.1.4).

$$\text{Mass}_{\text{SPHelement}} = \frac{\text{Filled Volume Mass}}{\text{Number of SPH}_{\text{element}}\text{ generated}} \quad (4.1.4)$$

Each SPH element has an effective mass and sum of all the particles mass should be equal to the filled volume total mass. FCC approach is recommended for use in RADIOSS solver (Altair 2014), which eliminated its use for this study and hence simple cubic mesh method is adopted. The second parameter in the panel is pitch that determines the distance between the two SPH elements, has discussed in Section 3.5. A smaller number of pitch results in more elements within the same space but without affecting the bird overall mass or density. The effect of pitch value on the pressure profile is discussed in Section 4.1.3.

4.1.3 SPH Pitch Comparison

The pitch value is selected on the basis of each SPH particle mass equal to that of the numerical mallard bird model mentioned in Section 3.6, because it gave the pressure results close to Wilbeck (1977) experiment. Table 15 shows increment in both number of SPH particles and mass for each pitch value starting from lowest distance of 2.7 mm. Pitch value of 2.7 mm represents mass of each particle equal to that of the mallard bird model i.e. 0.019 g, but with high number of SPH elements.

Table 15 Pitch value and effect on number and mass of each element

Pitch Value (mm)	No. of Particles	Mass of each particle (kg)
2.7	95516	1.905E-5
2.8	85302	2.133E-5
3.0	69242	2.628E-5
3.2	57246	3.179E-5
3.4	47553	3.827E-5
4.0	29278	6.105E-5

Even though the mallard bird model weigh range from 0.72 kg – 1.6 kg which is 13.13% lower than the assumed bird mass of 1.81 kg, there is higher number of particles (93.74%) compared to mallard bird model. One of the reasons for this high number of particles is the 100% filled volume mass. Mallard model has cavities that reduced the number of particles from 49,302 to 41,685 elements, whereas no porosity is reflected in this numerical bird model. The high number of SPH particles is also due to the total volume of the numerical model. Mallard bird has length of 500mm - 600mm with a wing span of 810mm - 980 mm, whereas the numerical bird model for this study has a length of 287 mm and no wing span. Therefore, high number of particles is incongruous as it could have led to high computational time. Table 16 further compares the effect of pitch value on both number of particles and mass of each particle with mallard bird model (49,302 SPH elements).

Table 16 SPH mesh comparison with mallard bird model

Pitch Value (mm)	Difference in number of SPH elements in comparison to mallard model	% change of elements in comparison to mallard model	Difference in mass of each SPH element in comparison to mallard model (kg)	% change in mass of each element in comparison to mallard model
2.7	46214	93.74%	0	0.00%
2.8	36000	73.02%	2.33E-6	12.26%
3.0	19940	40.44%	7.28E-6	38.32%
3.2	7944	16.11%	1.279E-5	67.32%
3.4	-1749	-3.55%	1.92E-5	101.42%
4.0	-20024	-40.61%	4.2E-5	221.32%

From the Table 16, it can be seen that the pitch value of 3.4 mm represents 3.55% lower SPH particles but 101.42% higher mass of each SPH particle compared to mallard bird model. In order to further evaluate an appropriate pitch value, benchmark tests were performed in which the Hugoniot and Stagnation pressure from all the above pitch values impacting on a 200 mm x 200 mm size rigid plate were compared with both Wilbeck (1977) experiments and calculated theoretical values using equations (3.3.4), (3.3.6) and (3.3.7).

Wilbeck (1977) emphasised that the shock duration for small birds with an irregular impact surface and a small radius of curvature was so small that the transducers did not respond rapidly enough to record the shock pressure. For larger birds with larger radii of curvature, the duration of the shock pressure was greater and hence the peak pressure shown in Figure 41, which was measured on several of the 4 kg bird tests approached the predicted values. Towards the impact end, there was a gradual decrease in the flow pressure, which made the measure of the steady flow pressure difficult for birds less than 4 kg (Wilbeck 1977:90). As there are no experimental data available for 1.81 kg birds from Wilbeck (1977) experiment, the Hugoniot pressure value from 2 kg birds is used for the validation. Due to unavailability of stagnation pressure for 2 kg or 1.81 kg bird, stagnation pressure from 4 kg birds as shown in Figure 42 is used for reference purpose.

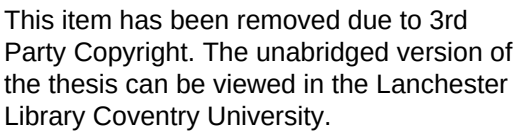

Figure 41 Hugoniot pressures measured at the centre of impact during normal impact of birds (Wilbeck 1977:85)

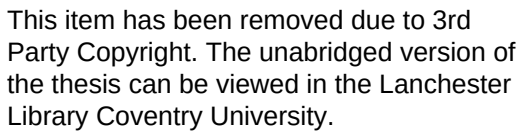

Figure 42 Stagnation pressures measured at the centre of impact during normal impact of birds (Wilbeck 1977:89)

As mentioned in Section 3.6, there are three ways to obtain the contact pressure profiles practiced by the researchers. The first is to obtain the contact force diagram and then divide it by the contact area at any instant. The second way is to obtain the contact force diagram and then divide it by the initial cross-section area of the bird. The third way is to obtain the contact force diagram between the bird and the shell sensor and then divide the force with the area of the sensor (Hedayati et al. 2014). The first two methods also called averaging method are not accurate because pressure is higher at the centre of contact area than the periphery. Also, the contact area will not remain constant due to diffusion of SPH particles after the impact. The third method requires more number of sensors to capture the contact force and area, and not just at the centre to measure the pressure values. Therefore, a new approach for this research is adopted, which is to initiate the contact area capture at each time step through LSDYNA command window using DATABASE_BINARY_INTFOR card. This contact interface database only initiate if the file name is provided on the execution line using S='filename'. The contact area during the impact was collected in a separate file and later divided by contact force to obtain contact pressure, but at a defined time step selected after the convergence.

Emphasis is also on the number of ASCII/Binary data points required from each impact test. An investigation on number of required data points was performed with

the hemispherical ended cylinder bird model and impact velocity of 80 m/s. The SPH pitch value of 2.7mm with Polynomial EOS values mentioned in Section 3.8.1 was used. The bird model was set at a distance of 5mm and was impacted on a rigid plate as shown in Figure 43.

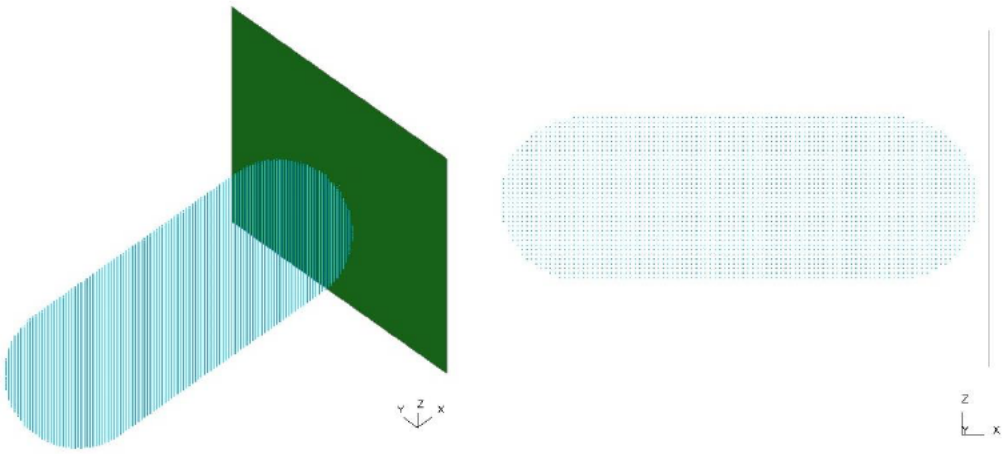

Figure 43 Pitch value 2.7 mm benchmark test setup

The units used in LS-DYNA were consistent for all the simulations and are as follows:

Table 17 LS-DYNA unit for simulation

Mass	Length	Time	Force	Pressure	Density
tonne	mm	second	Newton	MPa	tonne/mm^3

The time step automatically calculated by LS-DYNA was validated using the CFL equation (3.1.10) mentioned in Section 3.1.1. For this benchmark test, h = 2.7 mm and u= 80000 mm/s. Therefore,

$$\Delta t_{CFL} \leq 0.1 \frac{2.7}{8000}$$

$\Delta t_{CFL} \leq$ 3.375 E-6 seconds

However, to guarantee stability, Δt was scaled to 67% because bird strike is considered as a ballistic problem. The model time step automatically computed by LS-DYNA was 2.1E-6 seconds (2.1 μs), which is approximately 67% of the calculated 3.4E-6 seconds (3.4 μs), and hence no further lowering of time step was

required. The termination time of the LS DYNA model was set based on the total impact duration equation given by Wilbeck (1977) and expressed in equation (4.1.5).

$$T_D = \frac{l}{u} \quad (4.1.5)$$

where,

l = effective length of the bird

u= initial velocity of the bird

For this benchmark test, l = 287 mm and u=80000 mm/s and therefore,

$T_D =$ 3.5875E-3 seconds

The termination time was set to 4E-3 s (4 ms), to allow the bird model travel to the rigid wall and also considering the calculated duration impact. Figure 44 shows the bird diffusion at different time on the rigid plate with an increment of 0.001 s (1 ms).

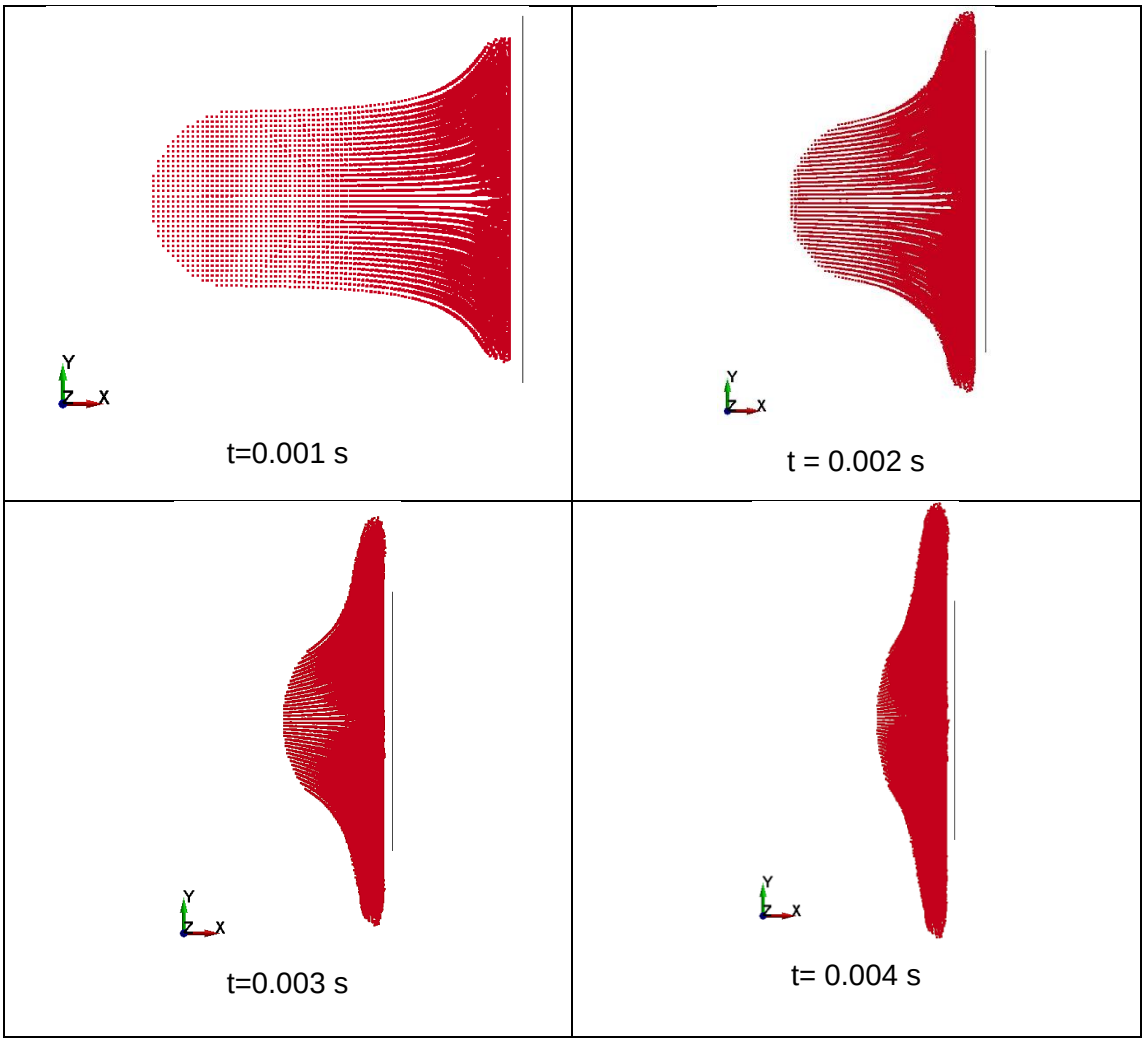

Figure 44 Bird impact on a rigid wall

In order to find out the appropriate time interval between outputs (DT) for ASCII/Binary data, DT was initially set to the model time step of 2.1E-6 s to collect maximum number of data followed by an increment of 1E-6 s (1 µs). Maximum number of data points possible are as follows:

$$\text{Maximum data points} = \frac{\text{Termination Time}}{\text{Model Timestep}} = \frac{4\text{E}{-3}}{2.1\text{E}{-6}} = 1905 \text{ (approx.)}$$

Figure 45 shows the effect of ASCII/Binary database DT value on the pressure profile for a pitch value of 2.7 mm.

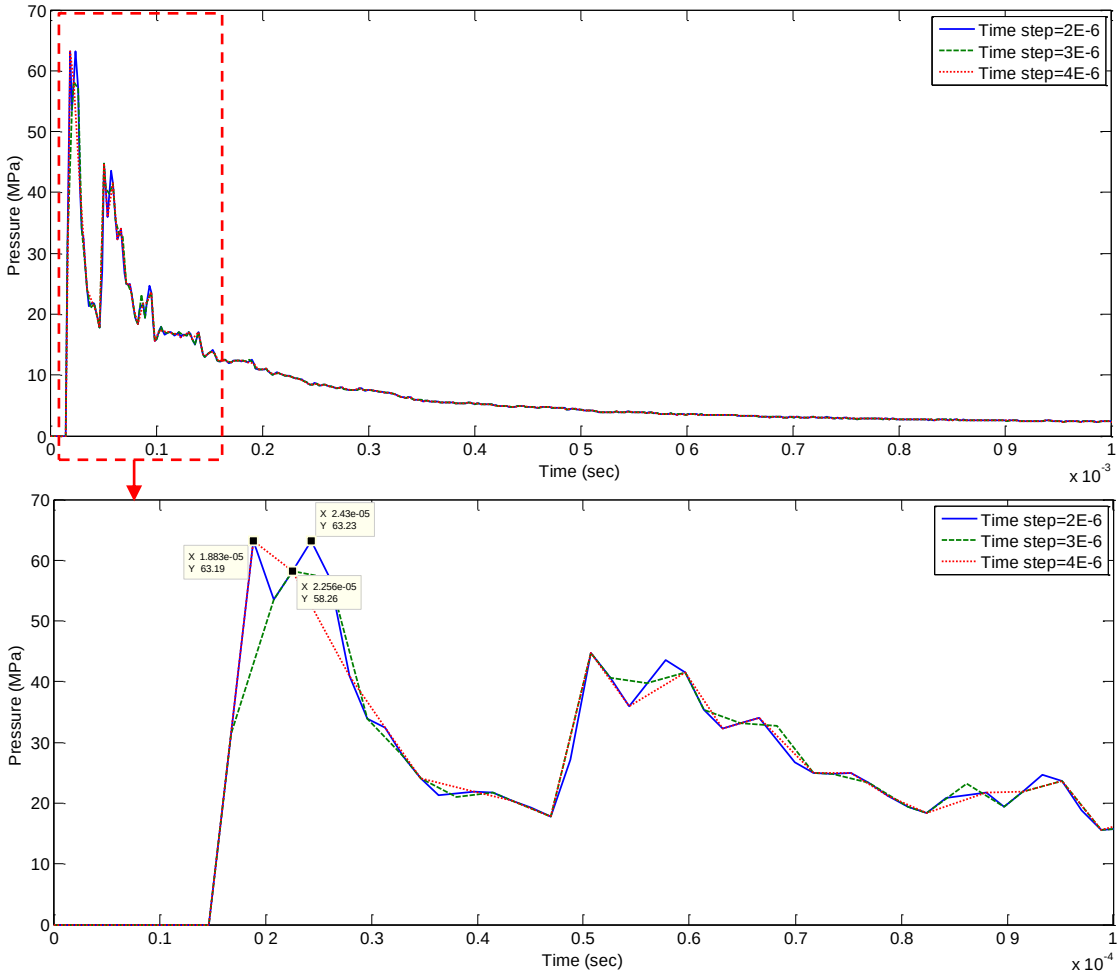

Figure 45 ASCII/Binary database DT value comparison on pressure profile

From the Figure 45, it can be seen that there is no significant difference in the pressure curve due to DT for a low impact velocity of 80 m/s. However, the peak pressure values and the computational time varies for each DT value and is shown in Table 18.

Table 18 Effect of ASCII/ binary DT value on peak pressure

DT value	Peak Pressure (MPa)	Computational Time	Number of data points
2.1E-06	63.23	29 min 52 sec	1905
3E-06	58.26	27 min 55 sec	1334
4E-06	63.19	27 min 4 sec	1001

From the Table 18, the difference in peak pressure value for DT of 2E-6 s and 3E-6 s is 7.86%, but there is a decrease in computation time by 6.53%. On the other hand, difference between DT of 2E-6 s and 4E-6 s is 0.06% for a decrease in computation time by 9.38%. Therefore, DT value of 4E-6 s is selected for the pitch value benchmark tests in the next Sections from 4.1.3.1 to 4.1.3.4, due to reduced computation time but without compromising on the peak and stagnation pressure values. In these tests, the bird model pitch values vary from 2.7 mm to 4 mm, which impact rigid wall with a range of velocities (80 m/s, 116 m/s, 150 m/s and 225 m/s).

4.1.3.1 Bird Impact at 80 m/s velocity

The first benchmark test was performed with bird model velocity of 80 m/s with a range of pitch values (2.7mm, 2.8mm, 3mm, 3.2mm, 3.4mm and 4mm). A plot of pressure against time is presented in Figure 46 to determine the Hugoniot and Stagnation pressure for each pitch value. It can be concluded that the pressure curve for the pitch values (in mm) of 2.7, 2.8 and 3.4 correlates well with Wilbeck (1977) experiment as peak pressure on impact is evident. On the contrast, pitch values (in mm) of 3, 3.2 and 4 have dispersion of pressure just before the peak pressure. The pressure values are further compared with the experimental values obtained from both Wilbeck (1977) and theoretical values, which are calculated using equations (3.3.4, 3.3.6 and 3.3.7) and is shown in Table 19.

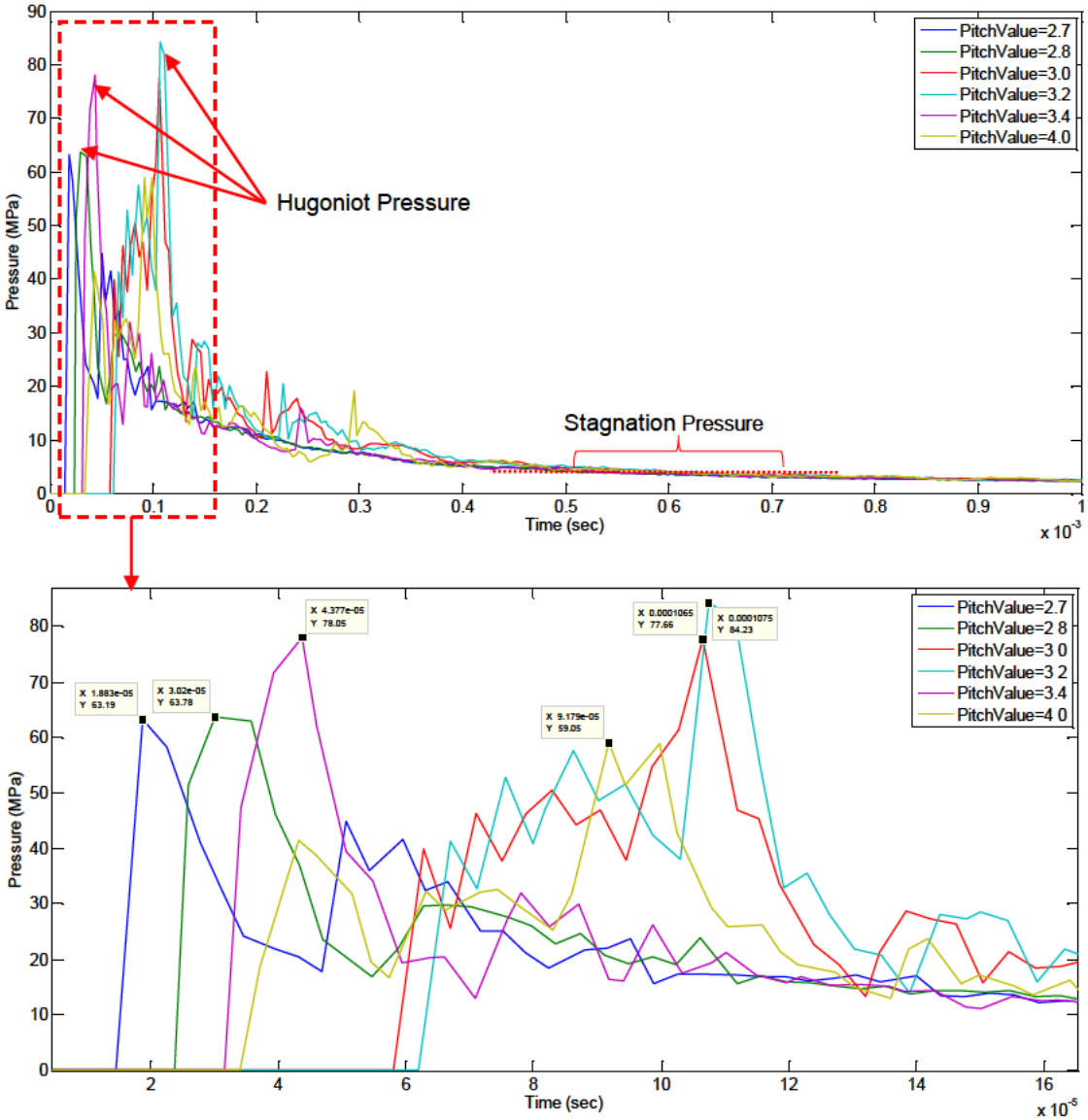

Figure 46 Pitch value comparison for bird impact at 80 m/s

The Hugoniot pressure for 2 kg bird and density of 950 kg/m^3 obtained from Wilbeck experiment (presented in Figure 47) was interpolated in MATLAB to determine the Hugoniot pressure at 80 m/s impact velocity for this study and is presented in Figure 48. Similar graph was plotted for 4 kg bird in order to determine the stagnation pressure at 80 m/s as presented in Figure 50, which was originally obtained from Wilbeck (1977) experiment (as presented in Figure 49).

Thi

Figure 47 Hugoniot pressure for different birds including theoretical value for $\rho = 950\,\frac{\mathrm{kg}}{\mathrm{m3}}$ (adapted from Wilbeck 1977:85)

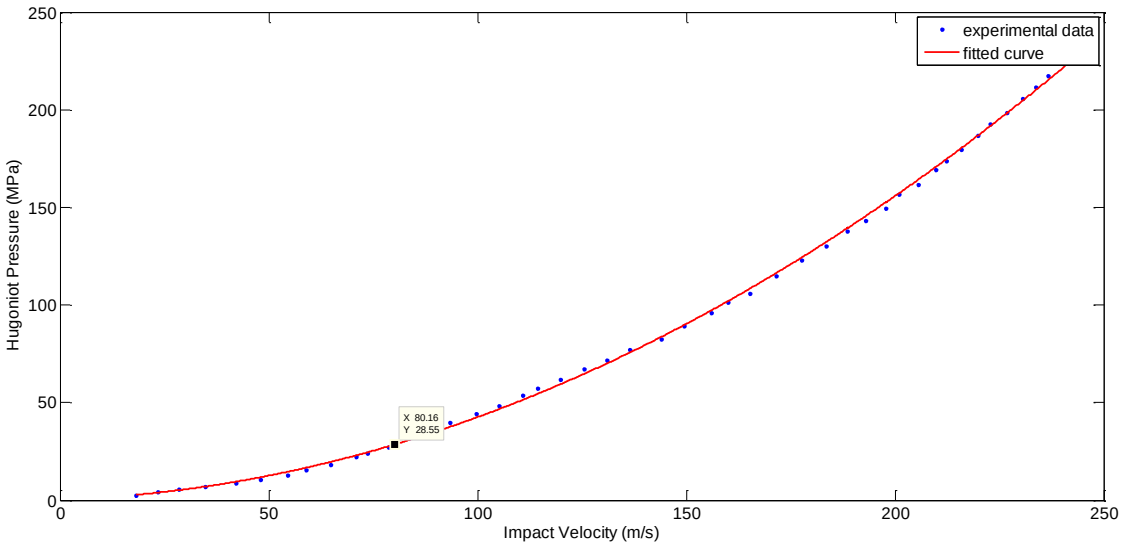

Figure 48 Hugoniot pressure derived from fitted curve for 2 kg birds

Figure 49 Stagnation pressure for 4 kg birds including theoretical value for $\rho = 950\,\frac{\mathrm{kg}}{\mathrm{m3}}$ (adapted from Wilbeck 1977:85)

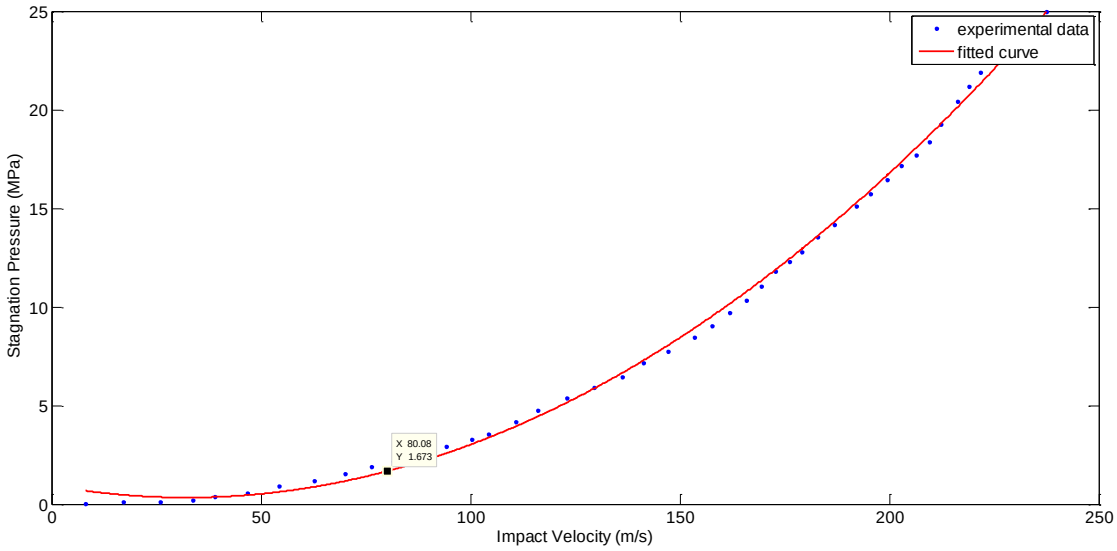

Figure 50: Stagnation pressure derived from fitted curve for 4kg birds

The experimental values from Wilbeck (1977) experiment for birds (chickens) impact at velocity 80m/s measured from centre of impact are:

Hugoniot Pressure for 2 kg bird = 28.55 MPa

Stagnation Pressure for 4 kg bird = 1.67 MPa

The theoretical values at velocity 80 m/s and density 950 kg/m^3 are calculated using equations (3.3.4, 3.3.6 and 3.3.7) mentioned in Section 3.3, which also correlates well with the Hugoniot and stagnation pressure profiles from Wilbeck experiment shown in Figure 47 and Figure 49.

Hugoniot Pressure:

$P_H = \rho_1 u_s u_o = \rho_1 \cdot (c_o + 2\, u_p) \cdot u_o$

=950 x (1482.9 + (2 x 80)) x 80

= 124.86 MPa ≈ 125 MPa

Stagnation Pressure:

$P_s = \frac{1}{2} \rho_1 u_o^2$

=0.5 x 950 x (80)^2

= 3.04 MPa ≈ 3 MPa

Table 19 Hugoniot and Stagnation pressure comparison for different pitch values at impact velocity 80 m/s

Pitch value (mm)	Hugoniot Pressure Value (MPa)	% difference in comparison to Wilbeck experiment (2 kg Birds)	% difference in comparison to theoretical value	Stagnation Pressure (MPa)	% difference in comparison to Wilbeck experiment (4 kg Birds)	% difference in comparison to theoretical value
2.7	63.19	121.33%	-49.45%	2.981	78.50%	-0.63%
2.8	63.78	123.40%	-48.98%	2.986	78.80%	-0.47%
3.0	77.66	172.01%	-37.87%	3.16	89.22%	5.33%
3.2	84.23	195.03%	-32.62%	3.431	105.45%	14.37%
3.4	78.05	173.38%	-37.56%	3.095	85.33%	3.17%
4.0	59.05	106.83%	-52.76%	3.115	86.53%	3.83%

From the Table 19, it can be seen that all the pitch values have Hugoniot pressure comparatively high, and in the range from 106% to 195% compared to Wilbeck (1977) experimental values for 2 kg birds. However, they are relatively low when compared to the calculated Hugoniot pressure, and within the range 32% - 52%. Pitch value of 4 mm is close to the Wilbeck (1977) experimental value with a difference of 106.83% when compared with other pitch values. In contrast, pitch value of 3.2 mm is close to the theoretical value with a difference of 32.62% when compared to other pitch values.

Similarly, pitch value of 2.7 mm is close to Wilbeck (1977) stagnation pressure experimental value (78.50%) when compared with other pitch values. Pitch value of 2.8 mm is closest to the theoretical stagnation value with only a 0.47% difference. The Peak or Hugoniot pressure is the primary reference point for this study, because the main apprehension is on the instantaneous damage after the impact. Although stagnation pressure from 4 kg bird is used for reference, relying only on the stagnation pressure is not appropriate, because the bird mass used for this study is almost half (1.81 kg). Therefore, further numerical simulations were performed with higher velocities such 116 m/s, 150 m/s and 225 m/s in order to evaluate the pressure profile of these pitch values at higher velocities.

4.1.3.2 Bird Impact at 116 m/s velocity

The second benchmark test was performed with bird model velocity of 116 m/s with a range of pitch values (2.7mm, 2.8mm, 3mm, 3.2mm, 3.4mm and 4mm). A plot of pressure against time is presented in Figure 51 to determine the Hugoniot and stagnation pressure for each pitch value followed by theoretical calculation and assessment of these values presented in Table 20.

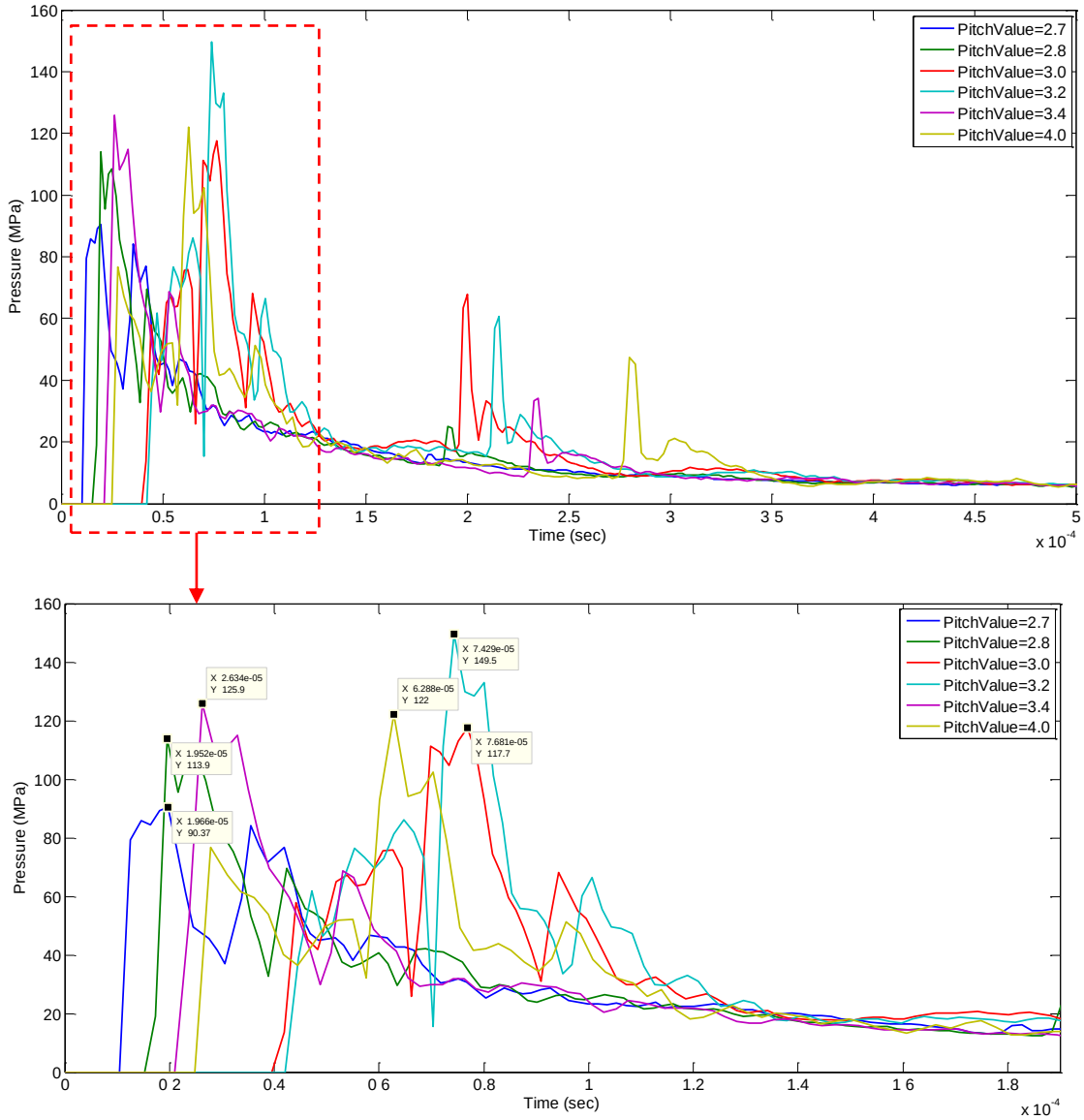

Figure 51 Pitch value comparison for bird impact at 116m/s

The experimental values from Wilbeck (1977) experiment for birds (chickens) impact at velocity 116 m/s measured from centre of impact are:

Hugoniot Pressure for 2 kg bird = 55.87 MPa

Stagnation Pressure for 4 kg bird = 4.48 MPa

The theoretical values at velocity 116 m/s and density 950 kg/m^3 are calculated using equations (3.2.4), (3.2.6) and (3.2.7) and are as follows:

Hugoniot Pressure:

$$P_H = \rho_1 u_s u_o = \rho_1 \cdot (c_o + 2\, u_p) \cdot u_o$$

=950 x (1482.9 + (2 x 116)) x 116

= 188.98 MPa ≈ 189 MPa

Stagnation Pressure:

$$P_s = \frac{1}{2}\rho_1 u_o^2$$

=0.5 x 950 x $(116)^2$

= 6.3916 MPa ≈ 6.4 MPa

Table 20 Hugoniot and Stagnation pressure comparison for different pitch values at impact velocity 116 m/s

Pitch value (mm)	Hugoniot Pressure Value (MPa)	% difference in comparison to Wilbeck experiment	% difference in comparison to theoretical value	Stagnation Pressure (MPa)	% difference in comparison to Wilbeck experiment	% difference in comparison to theoretical value
2.7	90.37	61.75%	-52.19%	5.78	29.02%	-9.69%
2.8	113.9	103.87%	-39.74%	5.535	23.55%	-13.52%
3.0	117.7	110.67%	-37.72%	6.158	37.46%	-3.78%
3.2	149.5	167.59%	-20.90%	6.326	41.21%	-1.16%
3.4	125.9	125.34%	-33.39%	5.707	27.39%	-10.83%
4.0	122	118.36%	-35.45%	6.491	44.89%	1.42%

For bird strike with impact velocity of 116 m/s, pitch value of 2.7 mm is close to the Wilbeck (1977) Hugoniot pressure value i.e. 61.75% difference when compared with pitch values. However, pitch value of 3.2 mm is near to the theoretical value (20.90%), similar to impact velocity of 80 m/s. In terms of stagnation pressure, pitch value of 2.8 mm is close to the Wilbeck (1977) experiment (23.55% difference), whereas pitch value of 3.2 mm is nearest to the theoretical value (1.16%). Therefore, from the above comparison it can be concluded that the pitch value of 3.2 mm

correlates well with the theoretical value for bird strike with impact velocity of 116 m/s.

4.1.3.3 Bird Impact at 150 m/s velocity

The third benchmark test was performed with bird model velocity of 150m/s with a range of pitch values (2.7mm, 2.8mm, 3mm, 3.2mm, 3.4mm and 4mm). A plot of pressure against time is presented in Figure 52 to determine the Hugoniot and stagnation pressure for each pitch value.

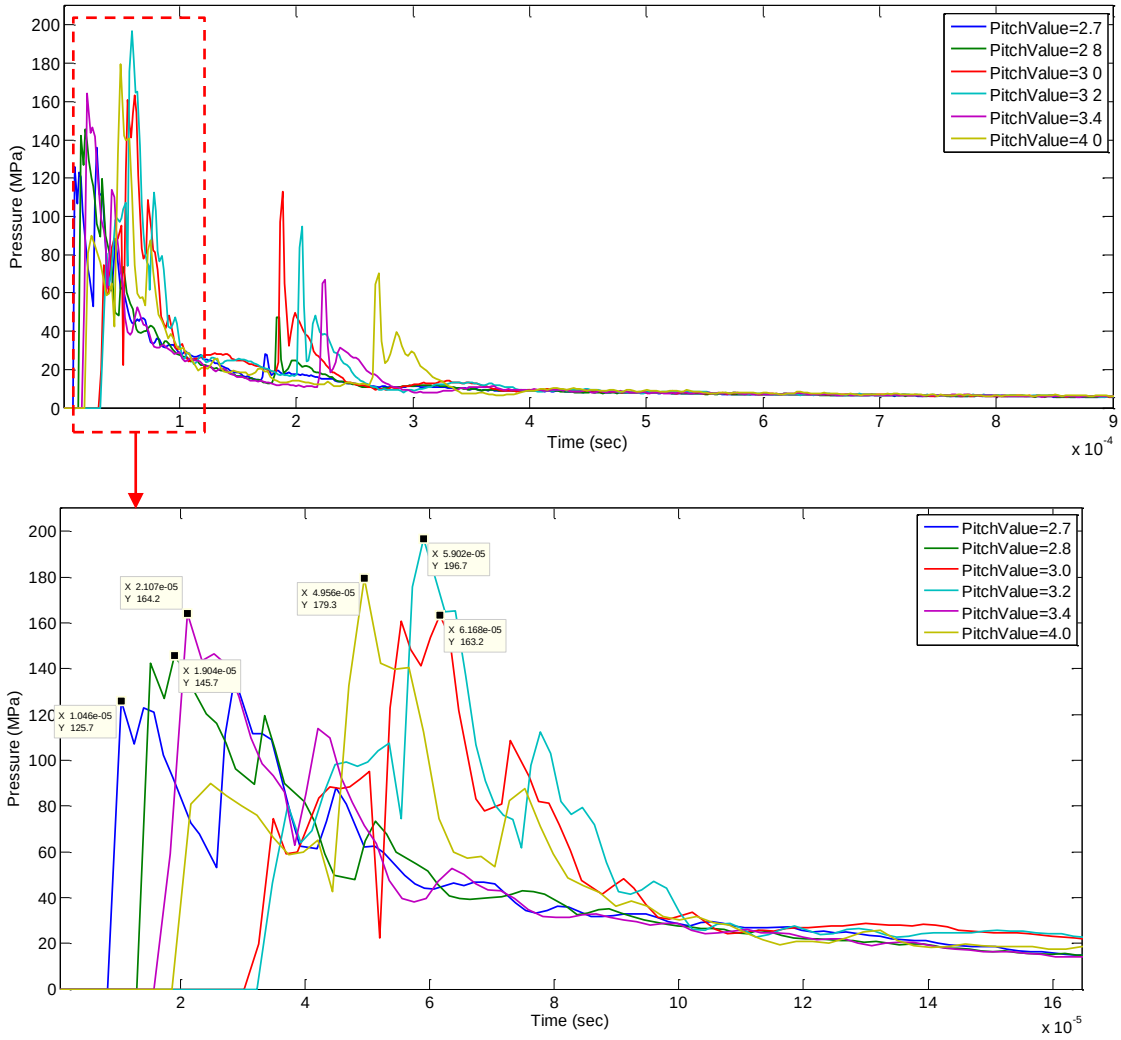

Figure 52 Pitch value comparison for bird impact at 150 m/s

The experimental values from Wilbeck (1977) experiment for birds (chickens) impact at velocity 150 m/s measured from centre of impact are:

Hugoniot Pressure for 2 kg bird = 90.26 MPa

Stagnation Pressure for 4 kg bird = 8.454 MPa

The theoretical values at velocity 150 m/s and density 950 kg/m^3 are calculated using equations (3.2.4, 3.2.6 and 3.2.7) and are as follows:

Hugoniot Pressure:

$P_H = \rho_1 u_s u_o = \rho_1 \cdot (c_o + 2\, u_p) \cdot u_o$

=950 x (1482.9 + (2 x 150)) x 150

= 254.06 MPa ≈ 254 MPa

Stagnation Pressure:

$P_s = \frac{1}{2} \rho_1 u_o^2$

=0.5 x 950 x (150)^2

= 10.6875 MPa ≈ 10.7 MPa

Table 21 Hugoniot and stagnation pressure comparison for different pitch values at impact velocity 150 m/s

Pitch value (mm)	Hugoniot Pressure Value (MPa)	% difference in comparison to Wilbeck experiment	% difference in comparison to theoretical value	Stagnation Pressure (MPa)	% difference in comparison to Wilbeck experiment	% difference in comparison to theoretical value
2.7	125.7	39.26%	-50.51%	8.764	3.67%	-18.09%
2.8	145.7	61.42%	-42.64%	9.197	8.79%	-14.05%
3.0	163.2	80.81%	-35.75%	9.219	9.05%	-13.84%
3.2	196.7	117.93%	-22.56%	9.046	7.00%	-15.46%
3.4	164.2	81.92%	-35.35%	9.413	11.34%	-12.03%
4.0	179.3	98.65%	-29.41%	8.973	6.14%	-16.14%

From the Table 21, it can be concluded that the pitch value of 2.7 mm is near to the experimental Hugoniot pressure (39.26%), whereas pitch value of 3.2 mm is close to the theoretical value (22.56%) when compared with other pitch values. Similarly, for stagnation pressure pitch value of 2.7 mm and 3.4 mm are close to the experimental and theoretical value respectively. Therefore, it can be concluded that the pitch value of 2.7 mm seems appropriate for bird impact at 150 m/s if only experimental values are considered.

4.1.3.4 Bird Impact at 225 m/s velocity

The fourth benchmark test was performed with bird model velocity of 225m/s and a range of pitch values (2.7mm, 2.8mm, 3mm, 3.2mm, 3.4mm and 4mm). A plot of pressure against time is presented in Figure 53.

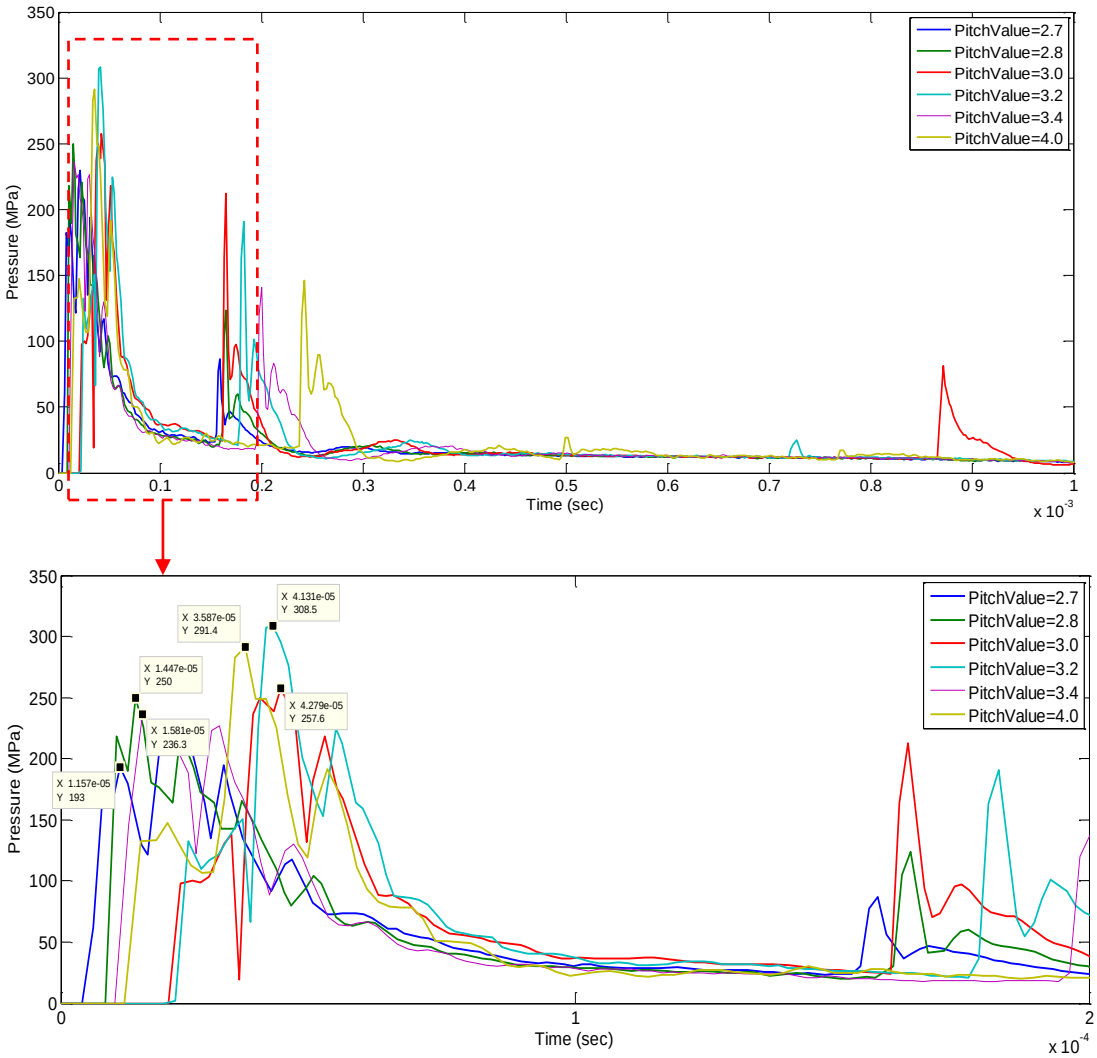

Figure 53 Pitch value comparison for bird impact at 225 m/s

The experimental values from Wilbeck (1977) experiment for birds (chickens) impact at velocity 225 m/s measured from centre of impact:

Hugoniot Pressure for 2 kg bird = 195.5 MPa
Stagnation Pressure for 4 kg bird = 22.09 MPa

The theoretical values at velocity 225 m/s and density 950 kg/m^3 are calculated using equations (3.2.4, 3.2.6 and 3.2.7) are:

Hugoniot Pressure:

$P_H = \rho_1 u_s u_o = \rho_1 \cdot (c_o + 2\, u_p) \cdot u_o$

=950 x (1482.9 + (2 x 225)) x 225

= 413.15 MPa ≈ 413 MPa

Stagnation Pressure:

$P_s = \frac{1}{2}\rho_1 u_o^2$

=0.5 x 950 x (225)^2

= 24.046 MPa ≈ 24 MPa

Table 22 shows the % difference of Hugoniot and Stagnation when compared to both Wilbeck (1977) experimental result and theoretical values. It can be seen that the pitch value of 2.7 mm is close to the experimental Hugoniot pressure i.e. 1.28% difference. Although, pressure value with pitch of 2.7 mm is lower than the experimental value, it contradicts with the numerical results obtained for the impact velocities (80 m/s, 116 m/s and 150 m/s). For all these impact velocities, pitch value of 2.7 mm is found to be greater than the experimental values. Pitch value of 3.2 mm is near to the theoretical Hugoniot value i.e. 25.30% difference. In terms of stagnation pressure, pitch value of 4 mm is comparatively close to both experiment and theoretical values, i.e. 9.33% and 16.54% respectively. Therefore, it can be concluded that the pitch value of 4mm correlates well with the stagnation pressure value for bird strike with impact velocity of 225 m/s.

Table 22 Hugoniot and stagnation pressure comparison for different pitch values at impact velocity 225 m/s

Pitch value (mm)	Hugoniot Pressure Value (MPa)	% difference in comparison to Wilbeck experiment	% difference in comparison to theoretical value	Stagnation Pressure (MPa)	% difference in comparison to Wilbeck experiment	% difference in comparison to theoretical value
2.7	193	-1.28%	-53.27%	17.09	-22.63%	-28.79%
2.8	250	27.88%	-39.47%	17.52	-20.69%	-27.00%
3.0	257.6	31.76%	-37.63%	15.75	-28.70%	-34.38%
3.2	308.5	57.80%	-25.30%	15.92	-27.93%	-33.67%
3.4	236.3	20.87%	-42.78%	19.9	-9.91%	-17.08%
4.0	291.4	49.05%	-29.44%	20.03	-9.33%	-16.54%

4.1.3.5 Pitch Value Conclusion

Comparing all the four benchmark tests, it can be concluded that the Hugoniot pressure and stagnation pressure obtained from pitch value of 2.7 mm is close to the Wilbeck experimental value for the selected velocities (116 m/s, 150 m/s and 225 m/s) when compared with other pitch values. Nonetheless, pitch value of 3.2 mm is close to theoretical Hugoniot value for all the velocities, whereas other pitch values such as 3.4 mm and 4 mm are close to the theoretical stagnation value. Further comparison was made in terms of computation time for all the pitch values and is shown in Figure 54. It can be seen that the computation time for pitch values of 2.7 mm, 2.8 mm, and 4 mm drops between impact velocity 80 m/s and 116 m/s, whereas it remains steady for pitch values of 3 mm and 3.2 mm. Similarity can be seen in the computation time reduction for all pitch values between impact velocity 116 m/s and 150 m/s. Furthermore, there is a steep increase in computation time for pitch values of 2.7mm, 2.8mm, 3mm and 3.2mm between impact velocity 150 m/s and 225 m/s.

Conversely, there is a reduction in computation time for pitch value of 3.4 mm and 4 mm between impact velocity 150 m/s and 225 m/s. Therefore, it can be concluded that the computation behaviour of all the pitch values are same for intermediate velocities i.e. between 116 m/s and 150 m/s. However, higher pitch values such as 3.4 mm and 4 mm needs significantly less computation time at higher velocities compared to lower pitch values, and this can be due to either less number of SPH particles or smoothing kernel function efficiency at higher pitch values.

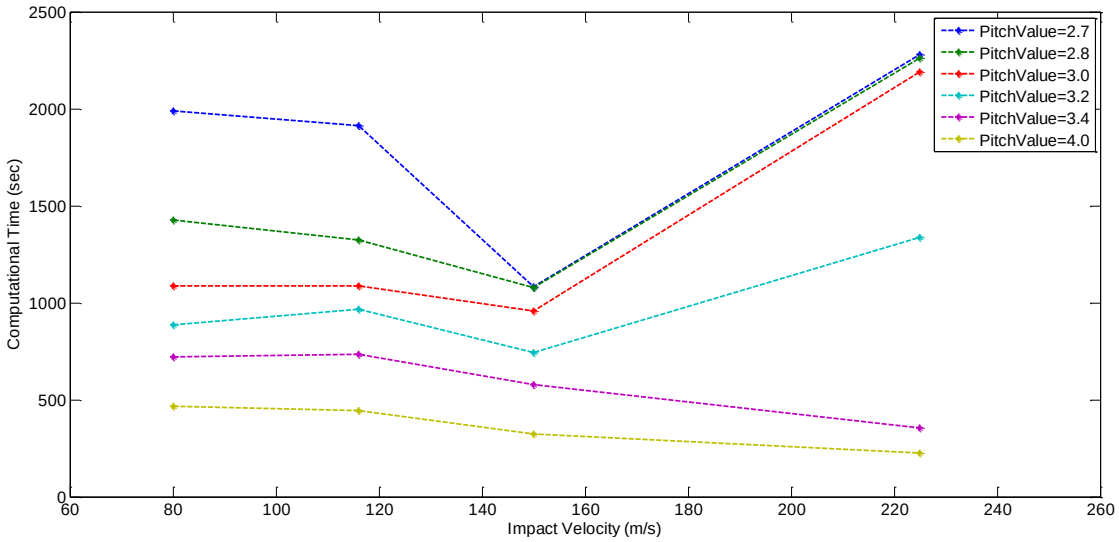

Figure 54 Computational time comparison for all pitch values

In order to further assess the pitch values, average of both experimental and theoretical values are considered for Hugoniot and Stagnation pressure and is shown in Figure 55 and Figure 56 respectively. The average Hugoniot pressure is relatively close to pitch value of 3.2 mm and 4 mm. However, pitch value of 3.4 mm is close to average stagnation pressure. As mentioned earlier in Section 4.1.3 that the stagnation pressure experimental values are from 4 kg bird strike, pitch value of 3.4 mm is disregarded for this study. Prominence is on Hugoniot pressure and out of the above mentioned pitch values (3.2 mm and 4 mm), Hugoniot pressures from 3.2 mm pitch are close to the theoretical values and also low in terms of computational time compared to 4 mm. Therefore, for this study pitch value of 3.2 mm with 16.11% higher number of SPH particle and 67.32% higher mass of each particle than the numerical mallard bird is adopted for the bird strike simulations on the composite leading edge.

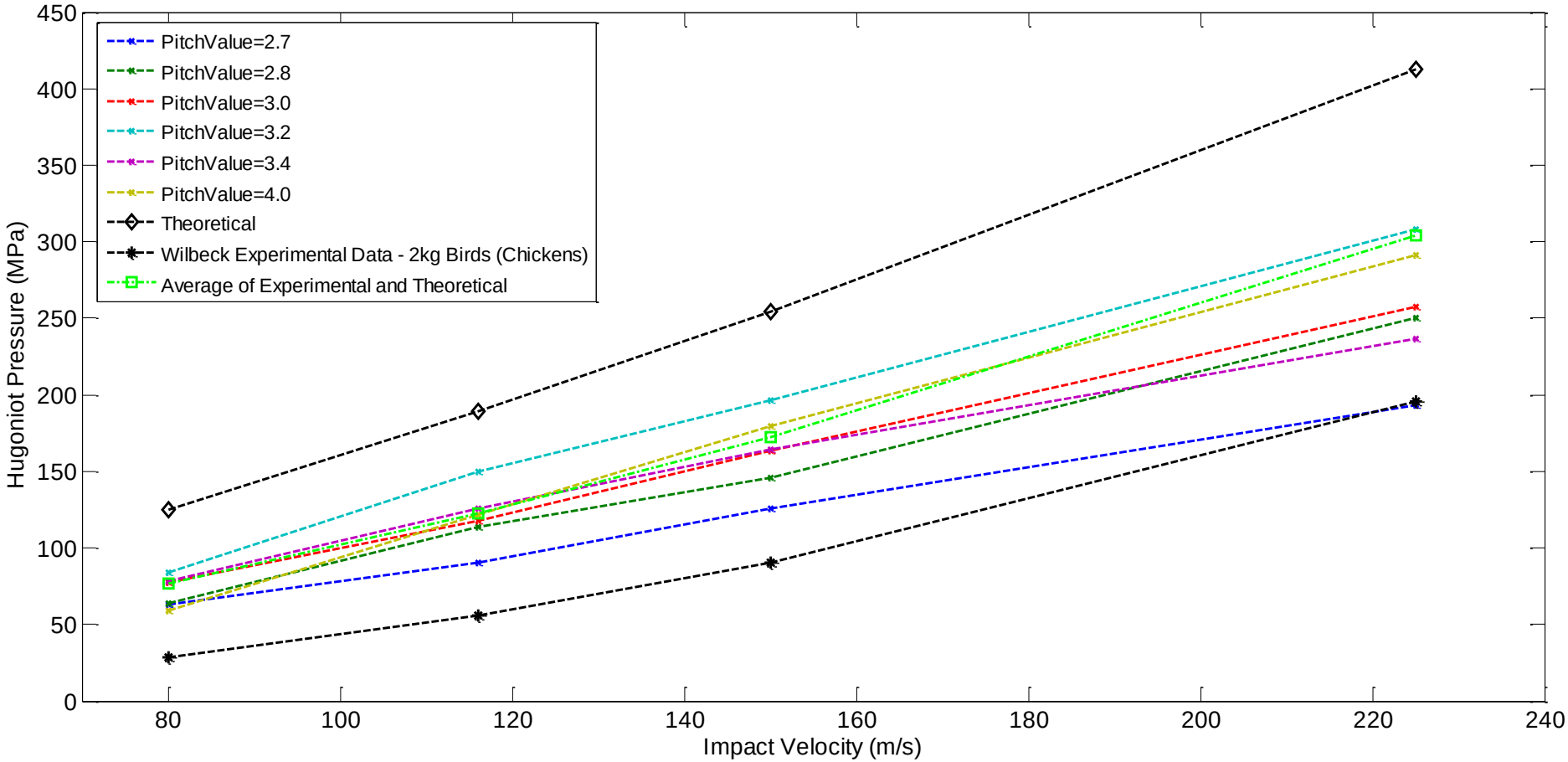

Figure 55 Hugoniot pressure comparison with experimental, theoretical and average values

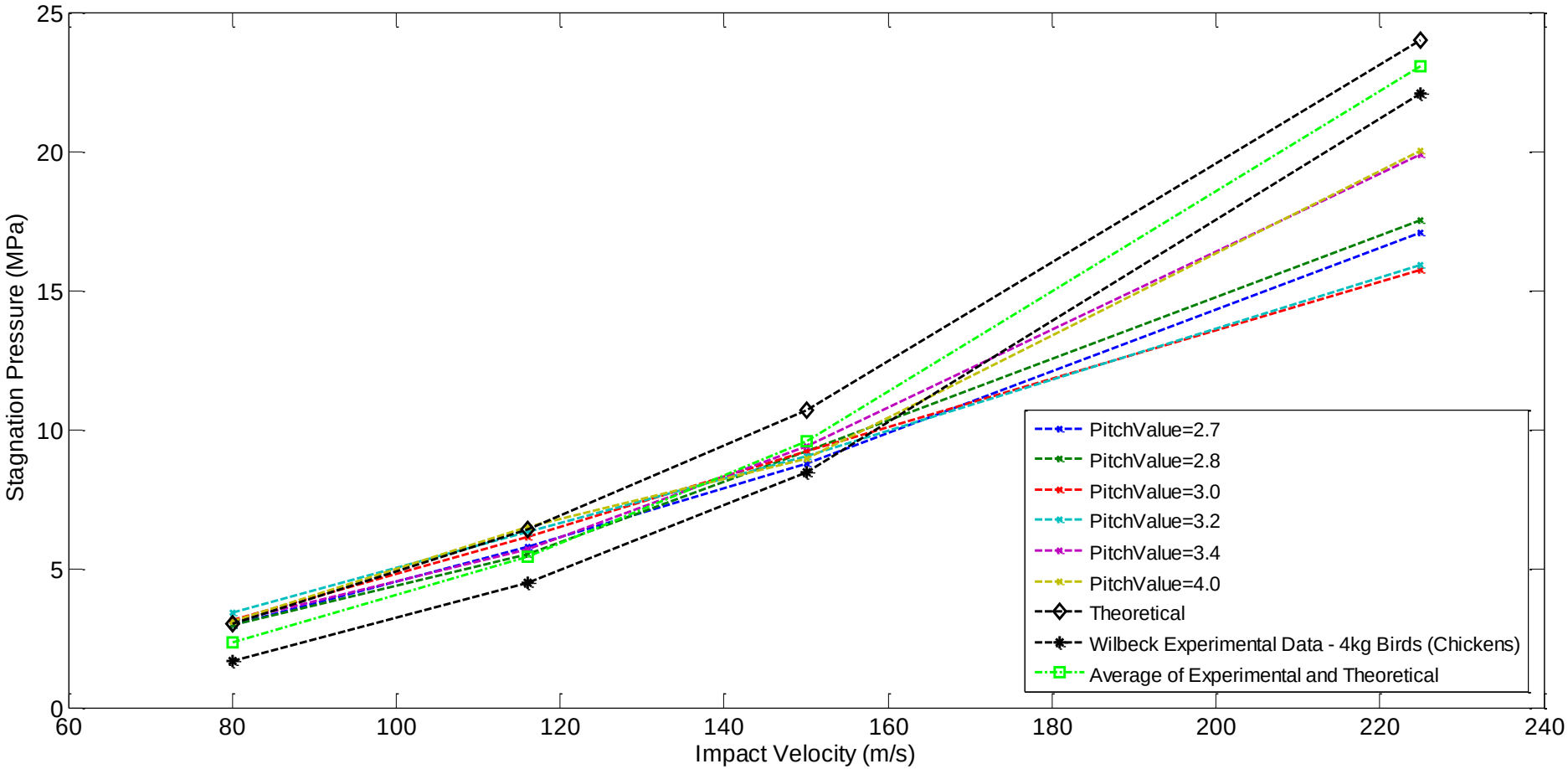

Figure 56 Stagnation pressure comparison with experimental, theoretical and average values

4.2 Wing Numerical Model

As mentioned earlier in Section 2.3, aircraft manufacturer's do not publish the wing's sensitive information in the public domain. Therefore, the author of this study derived the wing dimensions from data point extraction technique using the Image Processing Toolbox in MATLAB to create the CAD model.

Figure 57 Gulfstream G650ER dimension (Gulfstream 2015)

The first data set was extracted from Figure 57 (left) by defining the aircraft nose as a reference point i.e. x=0 and y=0 and the winglet as maximum length x=15.18 m and y=0 followed by multiple data point selection along the wing span including winglet. Likewise, for Figure 57 (right) data was obtained by defining wing nose as a reference point and x=30.41 m and y=0 followed by multiple data point selection along the wing chord length from root to tip. Each data set was stored as a 360-by-2 matrix variable in MATLAB workspace and later imported into CATIA for surface creation. The data set was also used to calculate wing parameters such as chord length (root & tip), span, sweepback angle (assuming 25% chord line), dihedral angle and taper ratio.

The G650ER wing aerofoil shape NACA (National Advisory Committee for Aeronautics) number was not disclosed by the manufacturer. Therefore, a similar predecessor aircraft type Gulfstream III aerofoil data was obtained from Applied Aerodynamics Group website (UIUC 2015) and is shown in Figure 58. Again, Image processing toolbox was used to create the aerofoil surface in CATIA by defining x=0 and y=0 as reference point. Multiple data point was selected along the aerofoil curve and the data was stored as 80-by-2 matrix variable.

Figure 58 Gulfstream III aerofoil (UIUC 2015)

Wing geometric information such as taper ratio, sweepback and dihedral angle were not given much consideration for this study, because the emphasis was only on the wing leading edge surface and its correlation and validation with the C27-J aircraft wing ribless leading edge surface numerical and experimental results by Guida et al. (2013). The CAD model shown in Figure 59 was created in CATIA and imported into HyperMesh software for meshing in 2D shell element. In triangular shell elements, higher order polynomials are used for the interpolation of the displacement field which makes it quite acceptable for numerical modelling of thin sheet metal parts such as an aircraft skin. Quad shell elements are generally preferred over triangular shell elements because they have one additional term included in their displacement function. This term generally provides more accurate results in comparison to triangular elements for certain geometries such as flat and non-sharp edges. For crash or non-linear analysis using a mixed-node element type instead of pure quads helps to achieve better mesh flow lines, and hence both quad and triangular elements have been used to mesh the wing leading edge surface. The element quality check is an important aspect of FE modeling, and therefore 2D element quality parameters such as skewness, aspect ratio, warp angle and Jacobian were considered and Table 23 shows the criteria applied to the mesh used.

Table 23 Wing 2D element quality parameters

Quality parameters	Value
Warp angle (not applicable for triangular elements)	min = 0° (ideal value) and max = 10° (acceptable)
Aspect ratio	min =1 (ideal value) and max = 5 (acceptable)
Skewness	min = 0° (ideal value) and max = 45° (acceptable)
Jacobian	min = 0.6 (acceptable) and max = 1 (ideal value)

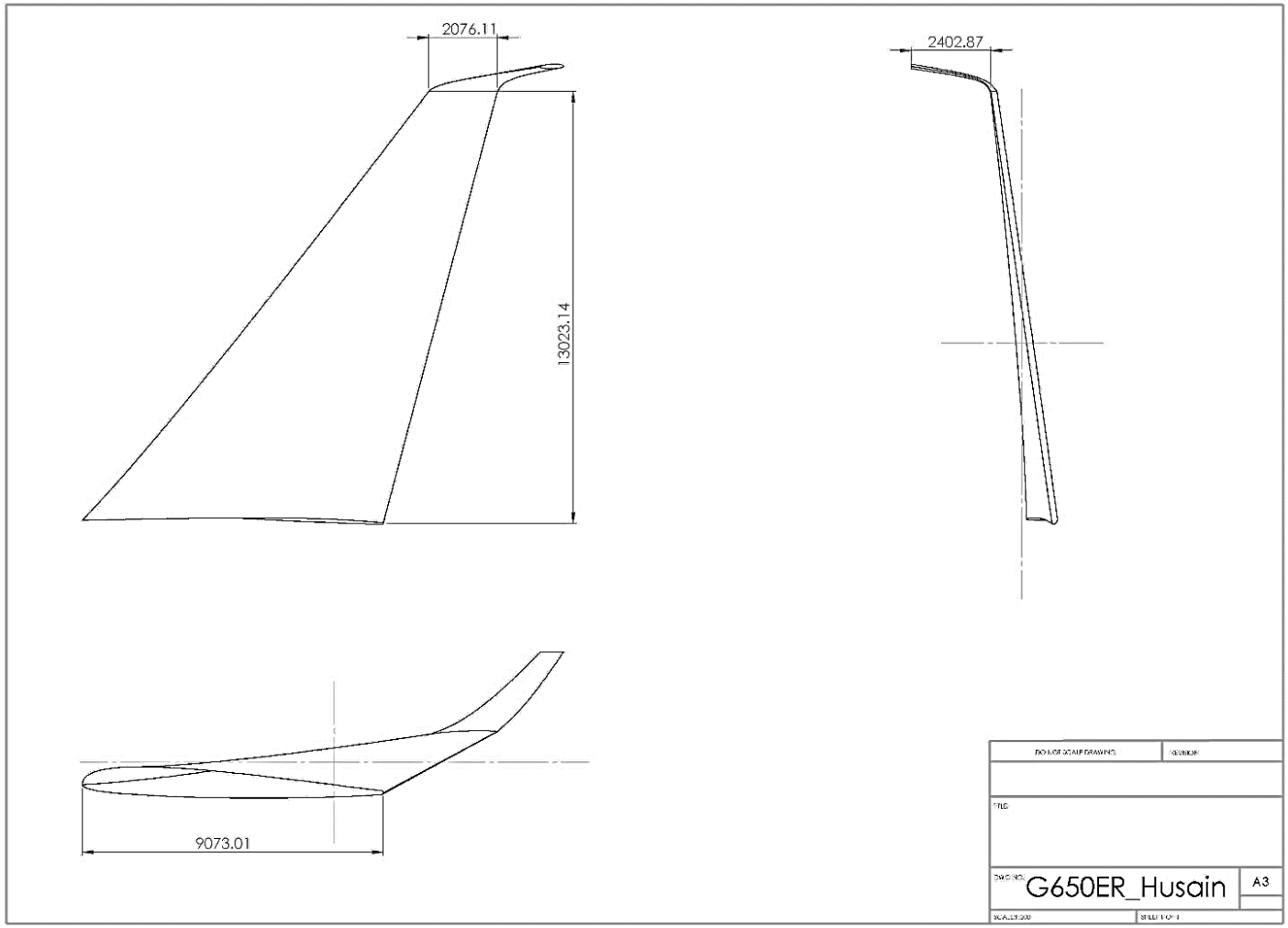

Figure 59 G650ER wing CAD model dimension

The approach for the element length was to obtain the minimum possible element length based on simulation timestep to achieve high accuracy. But for element length lower than 6mm, warning appeared in Hyper Mesh indicating that -element size is adjusted to node tolerance. Therefore, element length of 6 mm was chosen for the analysis purpose and Figure 60 shows the element quality for the whole wing.

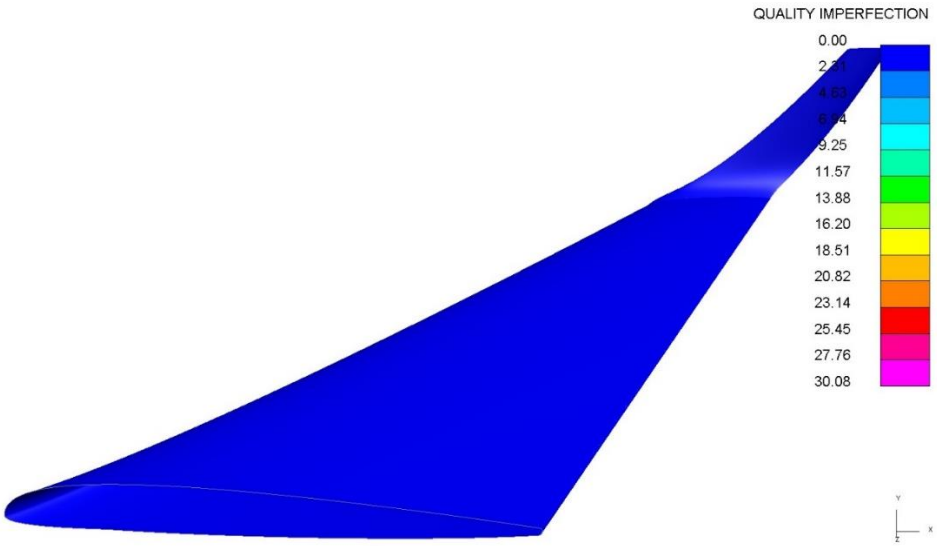

Figure 60 G650ER mesh quality

The total number of shell elements created with 6mm element length was 4,391,758 elements and that could have led to massive computational time. Bird penetration through the leading edge after the impact can be catastrophic if the bird hits the fuel tank. As fuel tank is installed close to the wing root, only a section of the wing leading edge from the root to the middle at a distance of 2000 mm, wing root chord length of 2800 mm and tip chord length of 1000 mm as shown in Figure 61 is considered.

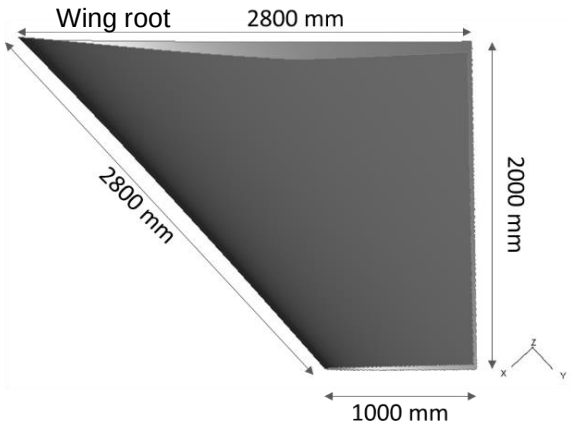

Figure 61 Wing dimension for impact simulations

The wing section (Figure 61) has total number of 270,645 shell element and is used for the two test cases keeping in mind accuracy with reasonable computation time. Further consideration was given to the element normals, and all the top section shell elements normals were aligned in outward or away direction as shown in Figure 62.

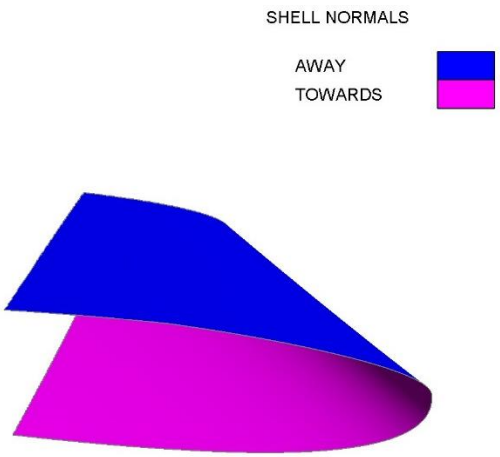

Figure 62 Wing shell element normals

The shell elements coordinates were aligned in such a way that each shell element direction of orientation is same to that of the global coordinate system. All the shell elements x-axis was aligned to the global x-axis using Element Shell > Normal/Align option with vector orientation and is shown in Figure 63.

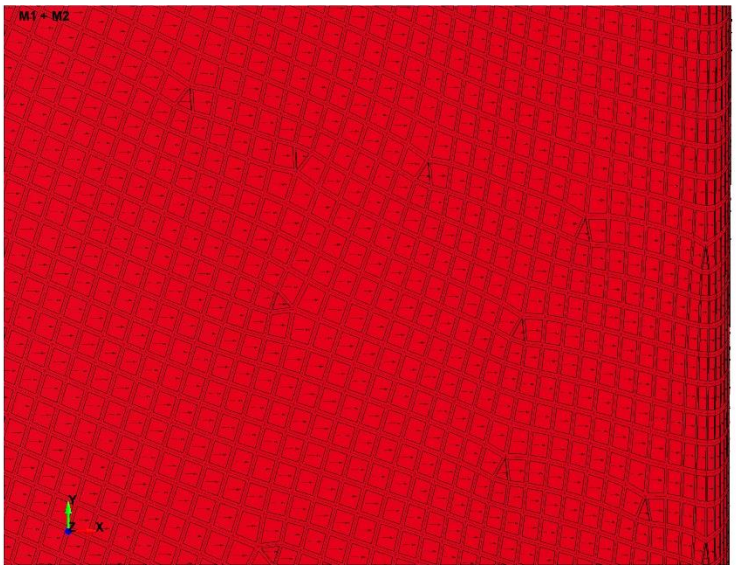

Figure 63 Wing shell elements orientation to x-axis

4.3 Simulation setup

Both bird SPH and wing models were imported into OASYS Primer software for simulation setup. The SPH bird model nodes, section and material ID cards were renumbered to avoid any clash during model merge. After merge, the wing edges were fixed using single point constraints (SPC) with a boundary condition card. The constrained wing and bird model was adjusted such that the bird impact at 90^{o} angle to the wing as shown in Figure 64. The impact force is higher at 90^{o} than at other angles, and hence it was deemed appropriate for this study in order to analyse the damage in worst case scenario. The wing nodes at the edges were defined to be constrained in all 6 degrees of freedom (DOF).

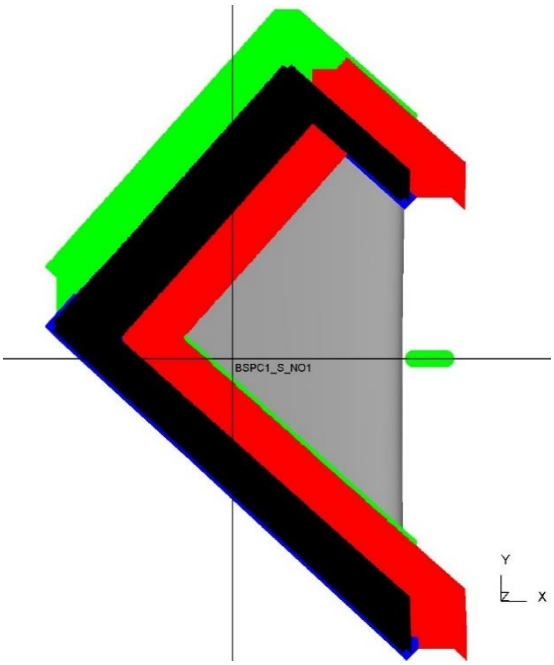

Figure 64 Bird impact at 90 degrees to the constrained wing leading edge

The bird and wing model material, section, contact and control cards were defined in LS-DYNA and is discussed in the Sections 4.3.1-4.5.3.

4.3.1. Material, Section and EOS card

Primarily the bird SPH section, material and equation of state (EOS) cards were defined in LS-DYNA and the parameters are shown in Table 24, Table 25 and Table 26 respectively.

Table 24 Bird SPH Section card parameters

Description	Notation	Value
Constant applied to the smoothing length of the particles	CSLH	1.2
Scale factor for the minimum smoothing length	HMIN	0.2
Scale factor for the maximum smoothing length	HMAX	2

Table 25 MAT_009: NULL card parameters

Description	Notation	Value
Mass Density	RO	9.5E-10
Pressure cut-off (≤0.0)	PC	-9.974E-2
Dynamic Viscosity	MU	1.0E-3

Table 26 EOS: LINEAR_POLYNOMIAL card parameters

Description	Notation	Value
The 0^{th} polynomial equation coefficient	C0	0
The 1^{st} polynomial equation coefficient	C1	2323
The 2^{nd} polynomial equation coefficient	C2	5026
The 3^{rd} polynomial equation coefficient	C3	15180

In a similar manner, the wing model section and material properties were defined using PART_COMPOSITE option. This option provides a simplified method of defining a composite material model for shell elements, which means integration rules and part ID's for each composite layer i.e. SECTION_SHELL and INTEGRATION_SHELL are not required. Table 27 shows the PART_COMPOSITE section parameters defined for the study.

Table 27 PART_COMPOSITE Section parameters

Description	Notation	Value
Element formulation	ELFORM	2
Shear Correction Factor	SHRF	1.0
Location of reference surface	NLOC	-1.0

In Table 27, ELFORM= 2 represents EQ.2: Belytschko – Tsay element formulation. It is based on Reissner - Mindlin kinematic assumption and a fully integrated membrane in which bending stiffness is negligible. As both triangular and quadrilateral element shapes are employed for the wing leading edge, this formulation allows mixing of the shells provided that the element sorting flag ITRIST on CONTROL SHELL card is set to 1 (discussed in Section 4.3.3). SHRF is the shear correction factor and set to the default value of 1.0 because LAMSHT=1 (Laminated Shell Theory) card is active due to use of dissimilar material layers (discussed in Section 4.3.3). NLOC defines the offset distance from the plane of the nodal points to the reference surface of the shell in the direction of the shell normal vector. In order to evaluate the effect of the NLOC values on the plies layup, author performed a simple test by modelling 7 plies with increasing thickness as populated in Table 28 and the results for the plies layup are shown in Figure 65, Figure 66 and Figure 67.

Table 28 NLOC effect on plies layup

Ply no.	Thickness (mm)
Ply#1	0.125
Ply#2	0.25
Ply#3	0.5
Ply#4	0.75
Ply#5	1
Ply#6	1.25
Ply#7	1.5

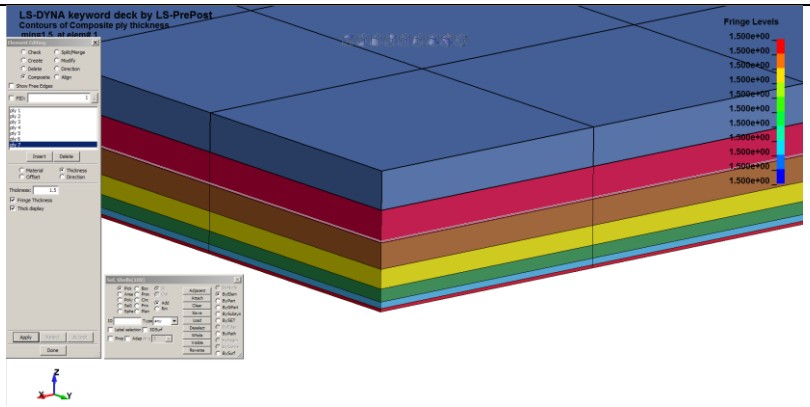

Figure 65 Composite Layup for NLOC=0

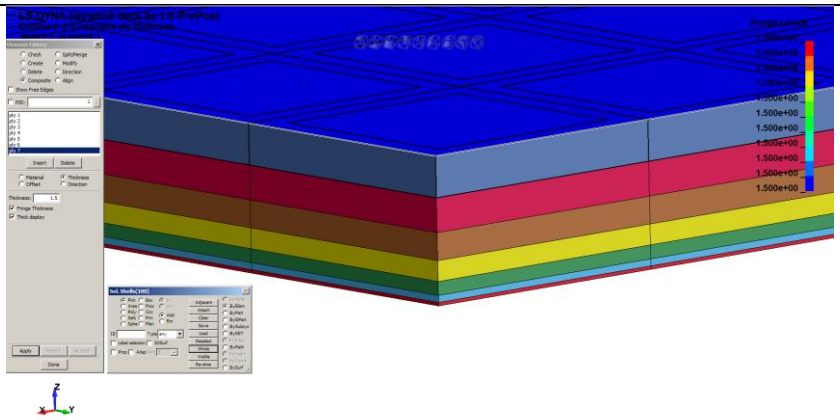

Figure 66 Composite layup for NLOC=1

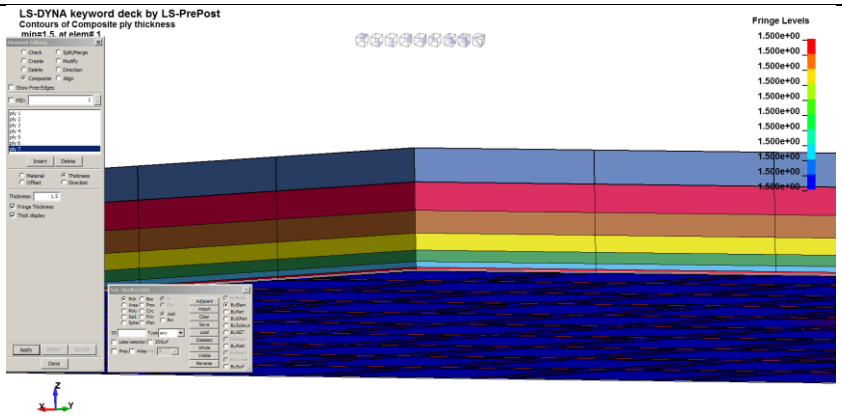

Figure 67 Composite layup for NLOC=-1

From the Figure 65, Figure 66 and Figure 67, it can be seen that the value of NLOC does not change the plies layup, and hence, useful only if a non-symmetrical layup has to be modelled. The choice of reference surface for the composite may vary from case to case, but here, it was assumed that the tooling surface was used as the reference surface when meshing the model i.e. the reference nodes should be located at the bottom of the first ply. Therefore, for this study symmetrical layup,

NLOC value was defined as EQ.-1: bottom surface. Furthermore, PART COMPOSITE layup option was used to define the orientation of each Al-2024 and fiberglass ply and is shown in Figure 68. B is the beta angle defined for each through-thickness layer. MID 2 is for Aluminium alloy 2024-T3 and MID 3 is for fiberglass and Table 29 and Table 30 defined these material cards respectively.

LAYER	MID	THICK	B	TMID
1	2	0.3	0.0	0
2	3	0.125	0.0	0
3	3	0.125	90.0	0
4	2	0.3	0.0	0
5	3	0.125	90.0	0
6	3	0.125	0.0	0
7	2	0.3	0.0	0
8	0	0.0	0.0	0

Figure 68 PART_COMPOSITE card parameters

Table 29 MAT_015: JOHNSON_COOK card parameters for Al-2024

Description	Notation	Value
Mass density	RO	2.7E-9
Shear modulus	G	28000
Young's Modulus	E	73000
Poisson's ratio	PR	0.33
Yield Strength	A	369
Strain hardening modulus	B	684
Strain rate dependent coefficient	C	8.3E-3
Strain hardening exponent	N	0.73
Temperature dependent exponent	M	1.7
Melt temperature	TM	775
Room temperature	TR	294
Quasi-static threshold strain rate	EPS0	1.0E-2

Table 30 MAT_022: COMPOSITE_DAMAGE CARD parameters for Fiberglass

Description	Notation	Value
Mass density	RO	2.7E-9
Young's modulus – longitudinal direction, E_a	EA	53200
Young's Modulus – transverse direction, E_b	EB	9300
Young's Modulus – normal direction, E_c	EC	9300
Shear modulus ab	GAB	5495
Shear modulus, bc	GBC	5495
Shear modulus, ca	GCA	5495
Effective failure strain	EFS	0.064
Longitudinal compressive strength	XC	725
Longitudinal tensile strength	XT	725
Transverse compressive strength	YC	75
Transverse tensile strength	YT	75
Shear strength	SC	75

AOPT for MAT_022 which is the material axes option was defined as 0. In this option the main fiber direction was determined by the element's main axis (n1 > n2).

4.3.2 Contact Card

In the bird strike simulation, the bird model comes in contact with the wing leading edge and therefore it is necessary to define a contact algorithm between the SPH nodes and the wing shell elements. AUTOMATIC NODES TO SURFACE contact card was defined, which is a one-way contact treatment and computationally efficient as it cost half the two-way contact treatment. Moreover, it is well suited to nodes impacting rigid bodies or surface. For the contact card, SPH nodes were selected as

a set of nodes on slave side and wing shell elements were selected as master side. All the automatic contacts include thickness offsets, and are recommended for impact and crash analysis. The geometry penetration between bird and wing was checked to eliminate any initial penetrations between them. Sometimes the modification of the geometry can change the result whereby penetrating nodes are not moved, but rather the initial penetration become the baseline from which additional penetration is measured. Therefore, LSTC (2012) recommends the tracking of initial penetrations by setting the parameter IGNORE=1 (ignore initial penetrations).

4.3.3 Control Cards

The control cards for all the impact simulations were defined according to the recommendation by LSTC (2012) for modelling of composites, and the values along with discussion are presented in Table 31.

Table 31 Control card parameters for the bird strike simulations

Notation	Value/EQ	Description
CONTROL_CONTACT		
SLTHK	EQ.1	Shell thickness considered in node to surface type contact options. EQ.1: thickness is considered but rigid bodies are excluded.
PENOPT	EQ.1	Penalty stiffness value option. EQ.1: minimum of master segment and slave node.
THKCHG	EQ.1	Shell thickness changes considered in single surface contact. EQ.1: shell thickness changes are considered.
CONTROL_ENERGY		
HGEN	EQ.2	Hourglass energy: Energy computed and included in the energy balance.
RWEN	EQ.1	Rigid wall energy: Energy dissipation not computed.
SLNTEN	EQ.2	Sliding interface energy: Energy dissipation is computed and included in the energy balance.
RYLEN	EQ.1	Rayleigh energy: Energy dissipation is computed and included in the energy balance.

CONTROL_HOURGLASS		
IHQ	EQ.4	Flanagan-Belytschko stiffness form. For explicit analysis, shell elements can be used with either viscous hourglass control (IHQ=1=2=3) or stiffness hourglass control (IHQ=4=5). Stiffness based HG is generally more effective than viscous HG control for structural parts and hence EQ.4 is used.
QH	0.05	Default Hourglass coefficient. With IHQ= 1-5, values of QH that exceed 0.15 may cause instabilities. Usually, when stiffness based HG control is invoked then HG coefficient should be in the range of .03 to .05.
CONTROL_TERMINATION		
ENDTIM	1.4 E-2	Termination Time.
CONTROL_TIMESTEP		
TSSFAC	0.67	Scale factor for computed time step. For high explosive or bird impact default is lowered to 0.67.
CONTROL_SHELL		
WRPANG	20.0	Shell element warpage angel in degrees. Default is 20 degrees.
ESORT	EQ.1	Sorting of triangular shell elements to automatically switch to C0 triangular shell formulation 4.
IRNXX	EQ.-2	Shell normal update option. Unique nodal fibers which are incrementally updated based on the nodal rotation at the location of the fiber.
THEORY	EQ.2	Default shell formulation. EQ.2: Belytschko–Tsay (default). LSDYNA recommend shell formulation with type 2 in terms of speed and robustness in comparison to type 16 which requires approximately 2.5 times more CPU than type 2 shells.
BWC	EQ.2	Warping stiffness for Belytschko-Tsay shells (default).
PROJ	EQ.1	Projection method for the warping stiffness in the Belytschko-Tsay shell. EQ.1: full projection.
INTGRD	EQ.0	Default through thickness numerical integration rule for shells. Less than 10 integration points (in this project 7 integration points) were defined and hence the default Gauss integration was adopted for the simulation. More than 10 integration points would have led to trapezoidal rule.EQ.1 Lobatto integration includes integration points on the outside surfaces and hence not recommended for composites.

LAMSHT	EQ.1	Laminated shell theory for all thin and thick shell materials. EQ.1: activate laminated shell theory. The stress discontinuities can be minimised between layers and at the bottom and top surfaces by imposing a parabolic transverse shear stress and hence laminated shell theory is activated for composites that have a transverse shear stiffness that varies by layer.
CONTROL_SPH		
IDIM	EQ.3	Space dimension for SPH particles. Bird Crash Impact is a 3D problem hence EQ.3 is used.

4.3.3.1. Effect of hourglass

Hourglass (HG) modes are non-physical modes of deformation that occur in under integrated elements, which in this study are shell elements, with a single in-plane integration point and produce no stress. One-point integration is much faster in comparison to fully integrated shells and is usually tolerable by using one of the several HG control algorithms. The hourglass control card was defined as type 4 (IHQ=4) with coefficient QH=0.05 which is the maximum default value to avoid instabilities. Type 4 Flanagan-Belytschko hourglass control evaluates hourglass stiffness rather than viscosity. Stiffness generates hourglass forces proportional to components of nodal displacements contributing to hourglass modes, and hence, preferred for crash simulation. The hourglass rates of equation are multiplied by the solution time step to produce increments of hourglass deformation. The hourglass stiffness is scaled by the element's maximum frequency so that the stability can be maintained as long as the hourglass scale factor is sufficiently small (LSTC 2014). Author of this study also looked into the effect of hourglass energy on the overall energy values. A benchmark test was performed with and without hourglass control card for bird strike with impact velocity of 116 m/s and the hourglass results are shown in Figure 69 and Figure 71 respectively.

Figure 69 shows the hourglass energy of the whole model, wing and SPH bird, and Figure 70 shows the K.E, I.E and T.E of the whole model when the hourglass control card is not defined. It can be observed that the hourglass energy of the whole model and the wing composite part increases linearly, which is not good for the solution. Therefore, it can be concluded that without hourglass control non-physical zero energy deformation modes are formed.

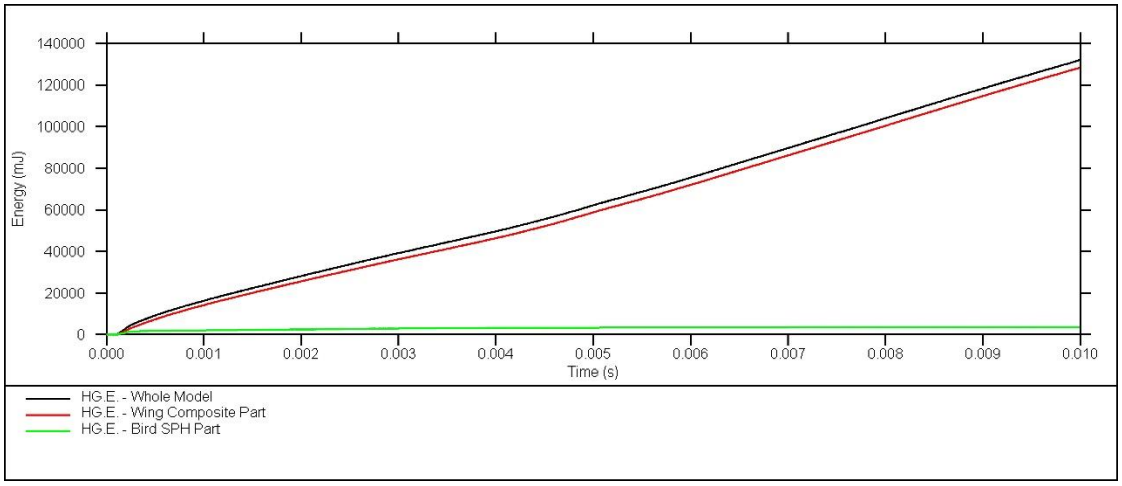

Figure 69 Hourglass energy without CONTROL_HOURGLASS card defined

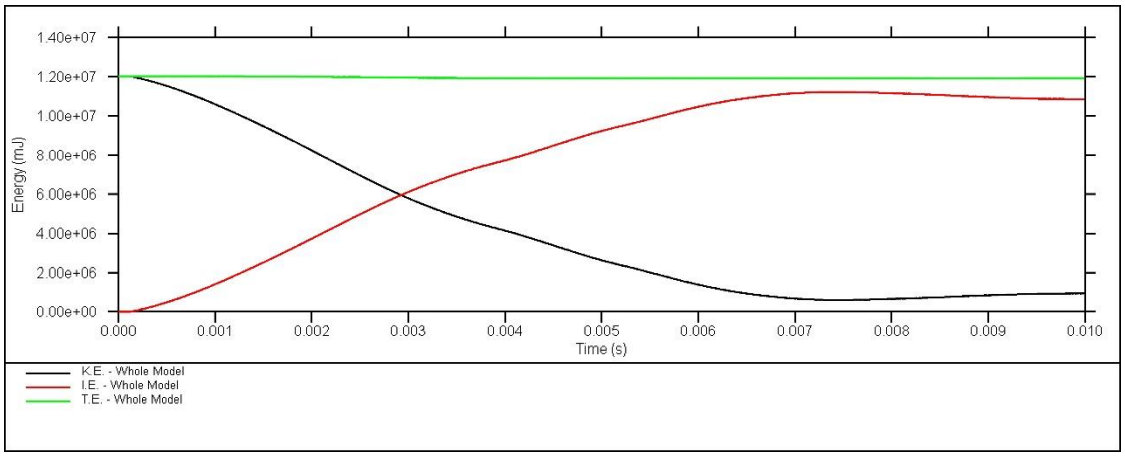

Figure 70 Energies of the whole model without CONTROL_HOURGLASS card

Figure 71 below shows the hourglass energy of the whole model, wing and bird, whereas Figure 72 shows K.E, I.E and T.E of the whole model when the CONTROL_HOURGLASS card is defined with IHQ=4 and QH=0.05. It can be seen that the maximum hourglass energy of the whole model is 20,856 mJ (20.86 J), which is 0.17% of the total energy (1.20E7 mJ or 12,000 J) and 0.18% of the internal energy (1.13 mJ or 11,300J) of the whole model.

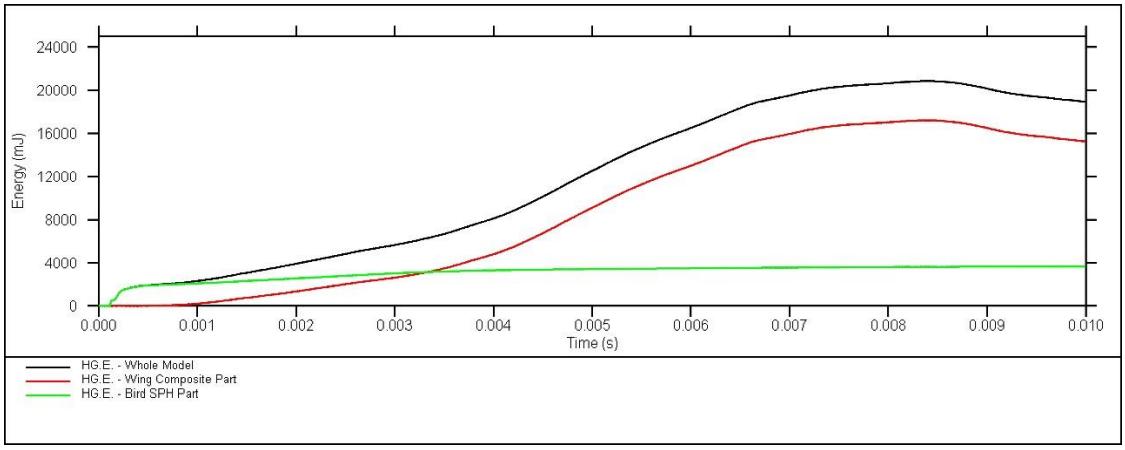

Figure 71 Hourglass energy with CONTROL_HOURGLASS card defined

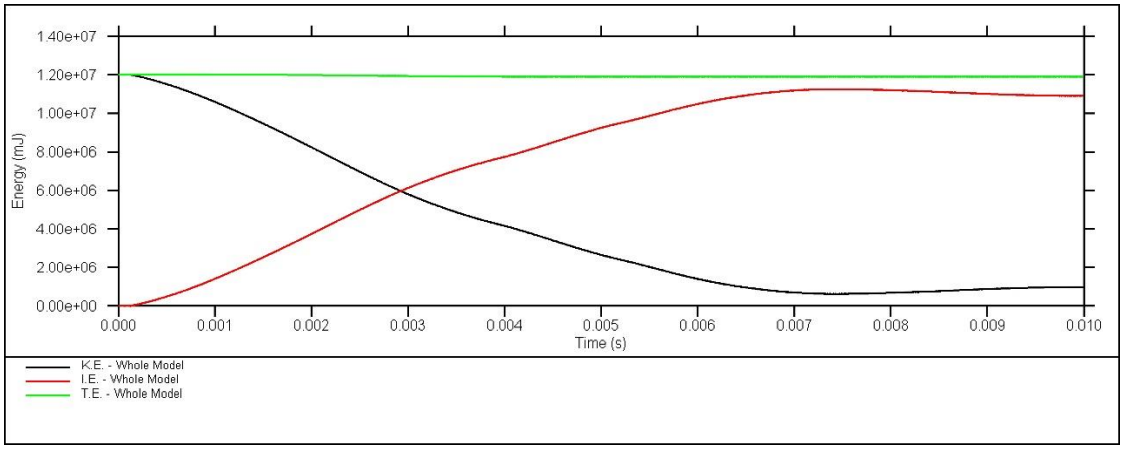

Figure 72 Energies of the whole model with CONTROL_HOURGLASS defined

According to the LSTC (2014) guidelines, HG should be <10% of internal energy and should also hold true for the total energy of the system. The defined hourglass control card meets the recommended criteria, and therefore, IHQ value of 4 and QH value of 0.05 is used for all the impact simulations in this study.

4.3.4 Composite Post-Processing Database Card

The shells history variable database card is defined to assess the failure mode of both aluminium alloy and fiberglass. The history variables are initiated through the DATABASE_EXTENT_BINARY card as variable NEIPS. By default, NEIPS=0 gives output of 6 history variables for each element integration points. The parameters of both Al-2024 and fiberglass material card history variables for inner, mid and outer surface layers are given in Table 32 and Table 33 respectively (LSTC 2014).

Table 32 MAT_015 Johnson Cook card history variables for Al-2024

History variable #	Description
1	Failure value
3	Current pressure cut-off
4	JC Damage Parameter
5	Temperature Change
6	JC failure strain

Table 33 MAT_022 Composite Damage card history variables for Fiberglass

History variable #	Description	Value
1	Longitudinal tensile failure mode along the fibres	1-elastic
2	Transverse tensile failure mode along the matrix	0-failed
3	Transverse compressive failure mode along the matrix	

The total number of integration points is determined by the number of entries on the PART COMPOSITE card as represented in Figure 68. There are 7 entries in the card for A/0/90/A/90/A configuration, and hence 7 integration points are required, which was initiated using the MAXINT option. MAXINT is the number of shell integration points written to the binary database. Default value of MAXINT=3, output results for the outermost (top) and innermost (bottom) integration points together with results from the neutral axis. For this study output from all the 7 layers are required, and therefore, the default value of MAXINT was changed from 3 to 7. The listing of integration points in the composite layers is shown in the Figure 73.

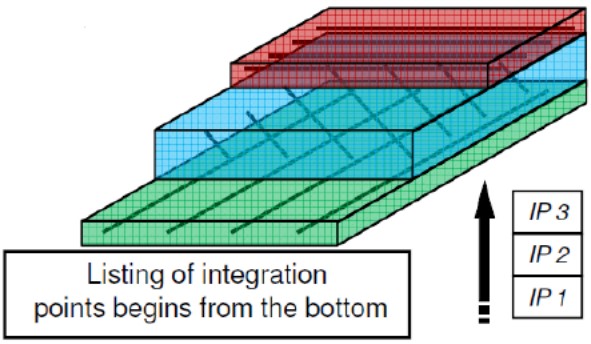

Figure 73: Location of integration points

The total thickness of the composite shell is the sum of the integration point thickness in which the shell thickness is assumed to be uniform. Thus, for 7 layers of plies and MAXINT=7, the corresponding layer of material is shown in Figure 74 which is also reflected in Section 5 results and analyses.

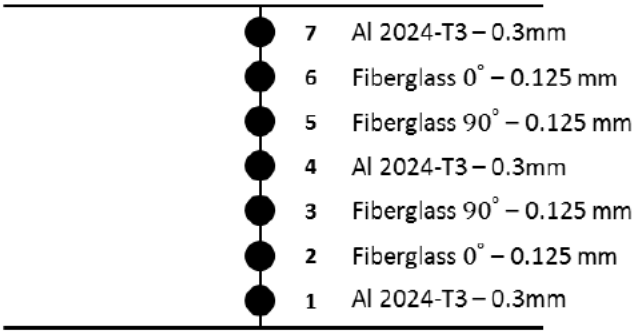

Figure 74: Location of material for integration points MAXINT=7

For composite material modeling, LSTC (2012) recommend stresses and strains to be written in the material coordinate system rather than the global coordinate system, because it is useful for post-processing of fiber and matrix stresses. CMPFLG is the flag to indicate the coordinate system for out of stress and strain in shells of orthotropic materials. It was set to 1 in order to obtain shell stress and strain values in material's local coordinate system. STRFLG is strain tensors for shell and was set to 11 to output both plastic and total strain tensors.

4.3.5 Test Cases

Two test cases were performed as part of this study, to assess the bird strike damage on the ribless composite wing leading edge. The two test cases are as follows:

Table 34 Test cases for bird strike simulation

Test Case	Bird Impact Velocity (m/s)	Description
#1	116 m/s	Take-off, climb and landing speed of G650ER.
#2	129 m/s	Compare the result with Guida et al. (2013) experiment for C-27J certification.

In the first test case, bird model impacts the leading edge at a velocity of 116 m/s (225 kts). This is the initial climb speed of the G650ER aircraft with weight 60,500 lb (27,442 kg) including 138900 lb (6,300 kg) of fuel. It was performed to assess the damage during take-off, climb or landing, which is half of the maximum speed for this aircraft type (Flightglobal 2015).

The second test was performed at a velocity of 129 m/s (250 kts) to compare the damage with a bird strike test performed by Guida et al. (2013). In this test, 8 lb (3.6 kg) bird impacted the leading edge of a FML material, used as an outboard sheet with aluminium flex core as shown in Figure 35 for the certification of C-27J aircraft ribless composite leading edge at a speed of 250 kts. The comparison is not completely germane, because not only the mass of the bird but also the wing leading edge material layup used for the numerical simulation by Guida et al. (2013) are different. However, there are no other experimental and numerical data available for 4 lb (1.81 kg) bird impact on FML wing leading edge for a high velocity business jet. Therefore, the results from Guida et al. (2013) is used for reference purpose to evaluate the numerical value offsets obtained from this study.

5. Simulation Results and Analyses

5.1 Test Case I – Bird Impact at 116 m/s (225 knots)

As mentioned in Section 4.3.5, the first test was performed with bird model velocity of 116 m/s impacting the ribless composite leading edge. Figure 75 shows the kinetic and internal energy of the both bird and wing.

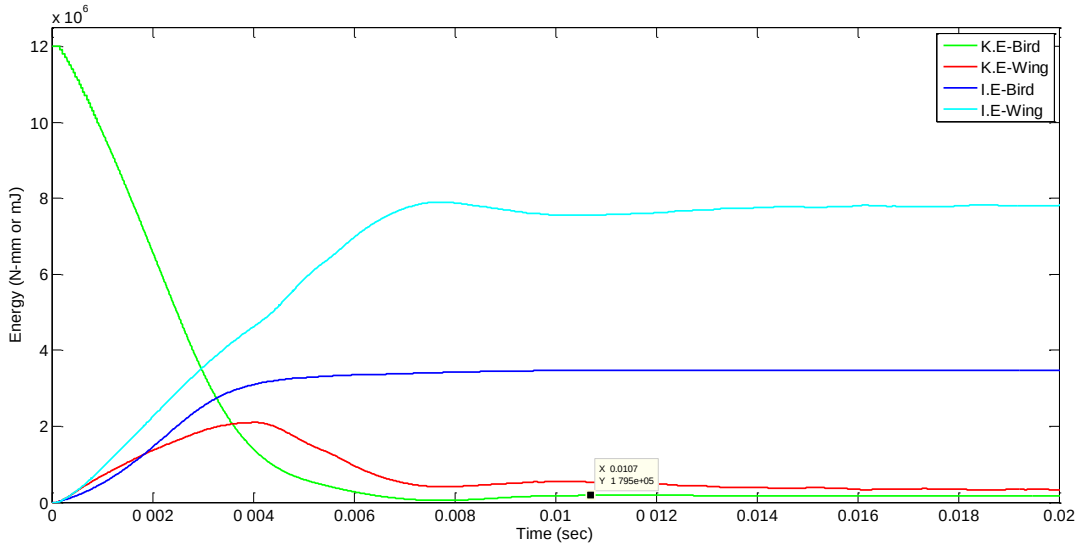

Figure 75 Kinetic and internal energy for bird impact at 116 m/s

From the Figure 75, it can be seen that the bird K.E energy of about 12E6 mJ (12,000 J) is impacted on the wing leading edge (LE). The impact energy is basically bird K.E, which can be calculated using equation (2.4.1).

$$\mathrm{K.E} = \frac{1}{2}\mathrm{mv}^2 = 0.5 \times 1.81 \times 116^2 = 12,177.68 \text{ Joules}$$

The bird K.E energy fell to a constant value of about 0.177E6 mJ (177 J) by time = 0.0107 s (10.7 ms), when the bird leaves the wing leading edge with a reduced velocity. An increase in the K.E energy of the wing is observed, which is due to the transfer of energy from the bird to the leading edge during impact. Shortly, there is a decrease in the wing K.E until a constant K.E value is reached after time=0.01707 s (10.7 ms) as no more energy is transferred. In contrast to this, internal energy of both bird and wing increases from zero and finally stabilises after reaching a maximum value. The internal energy is computed in LS-DYNA based on the six components of stress and strain (tensorial values) and is done incrementally for each element. The contact force for the impact is shown in Figure 76 and it can be seen that the

maximum contact force experienced by the leading edge during the initial bird impact is 43,860 N at time 0.00012 s (0.12 ms). There is also a comparatively higher contact force of 44,370 N experienced at time 0.00264 s (2.64 ms). This type of secondary peak force can be due to the mass of the bird being lumped at the nodes and non-homogeneous shape of the bird, which largely depends on the mesh topology used such as simple cubic and is also observed by Meguid et al. (2008:493). The contact force in LS-DYNA for automatic nodes to surface contact type is computed by summation of each slave node mass and acceleration in contact with each master side surface element during the impact.

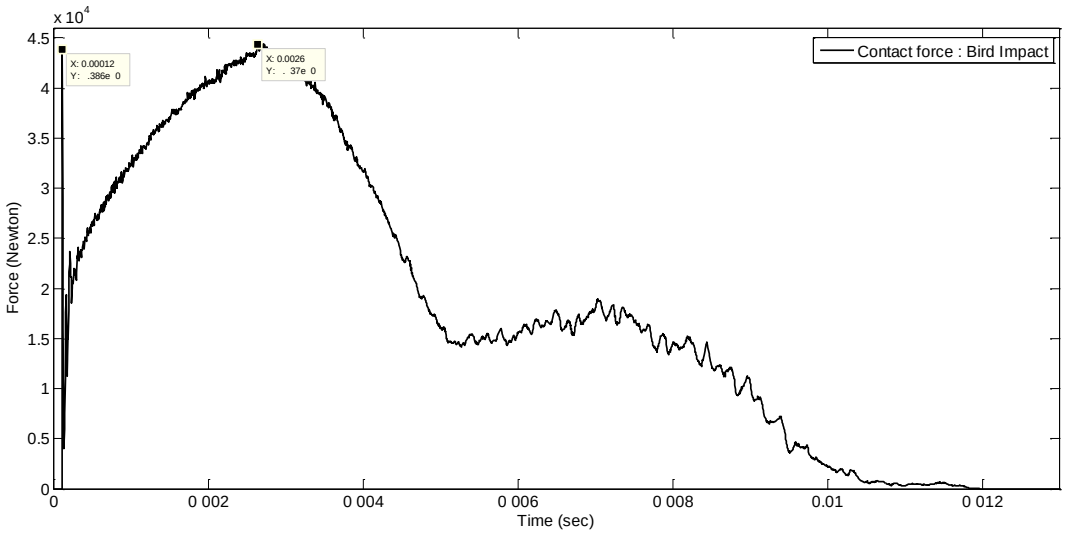

Figure 76 Force vs time history for bird impact at 116 m/s

For maximum stress theory failure criterion to apply, the maximum stress on the shell element at the centre of impact was converged to the principal stresses for all the 7 integration points and compared with their corresponding strength values as discussed in Section 3.9.3.1. Figure 77 shows stress in X direction or σ_{11} for each ply in the material local coordinate system. It can be seen that the simulation result correlates well with the expected physical phenomena. When the topmost ply (ip#7) is under tension at the start of the simulation then the bottommost ply (ip#1) is under compression and vice-a-versa is noted through the rest of the simulation. It can also be determined that the converged principal stress i.e. in this case is X direction when compared with the corresponding strength both X_t = 725 MPa (tension strength along the fibers) and X_c =725 MPa (compression strength along the fibres), then the fiberglass composite plies 3, 5 and 6 failed in tension at stress value of 674 MPa, 664.1 MPa and 719.6 MPa respectively. Fiberglass ply 2, which is the bottom ply did not fail and endured the stress produced during impact.

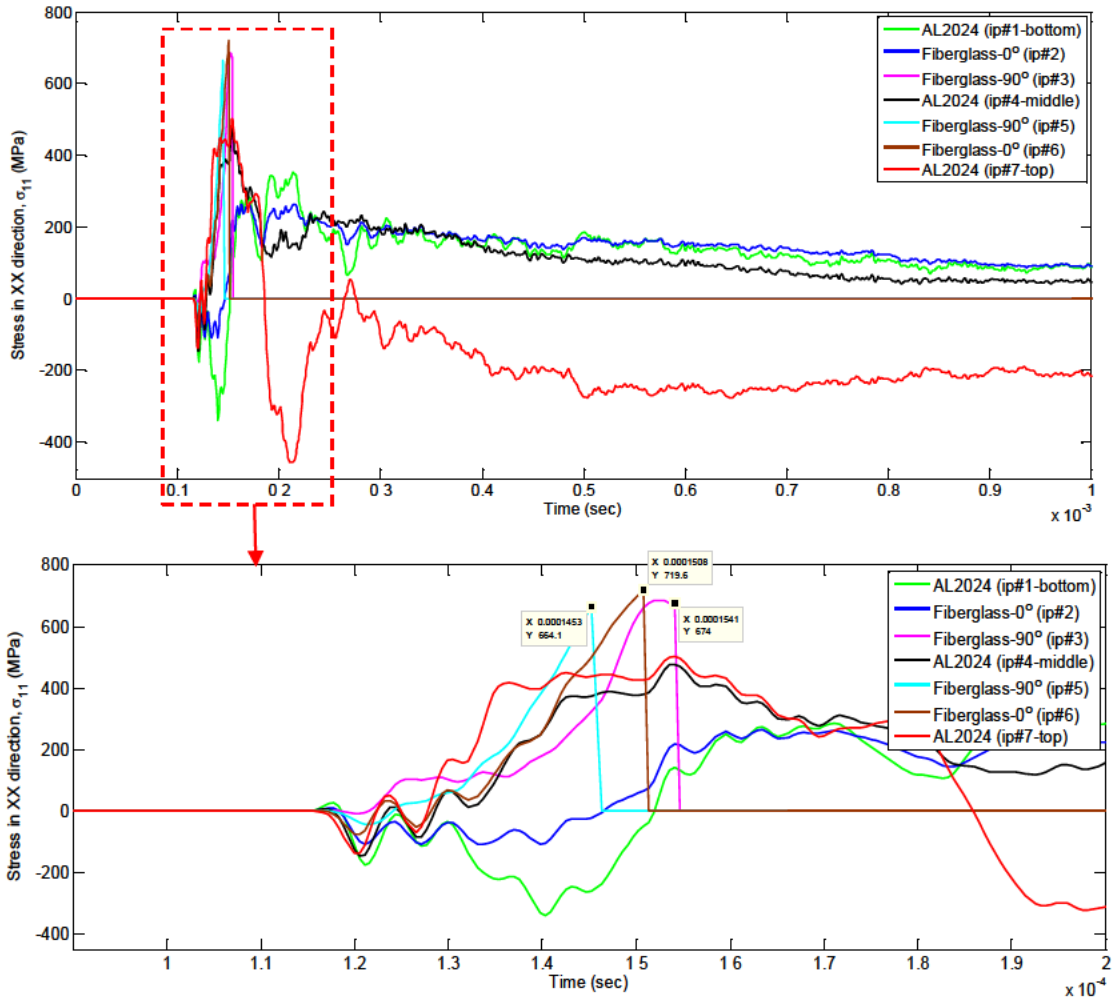

Figure 77 Stress in X direction for bird impact at 116 m/s

It can also be noted that the stress values obtained in Figure 77 are slightly less than the material strength along the fibers X_t and X_c values. But still the plies failed, and it can be due to the database timestep. However, the difference is not high with respect to X_t and the comparison is presented in the Table 35.

Table 35 Ply stress in X direction comparison with X_t for bird impact at 116 m/s

Ply #	Tension strength along the fibres, X_t (MPa)	Stress in XX direction, σ_{11} (MPa)	% difference in comparison to X_t
3	725	674	-7.03%
5	725	664.1	-8.4%
6	725	719.6	-0.74%

Figure 78 shows the stress in Y direction or σ_{22} for each ply in the material local coordinate system.

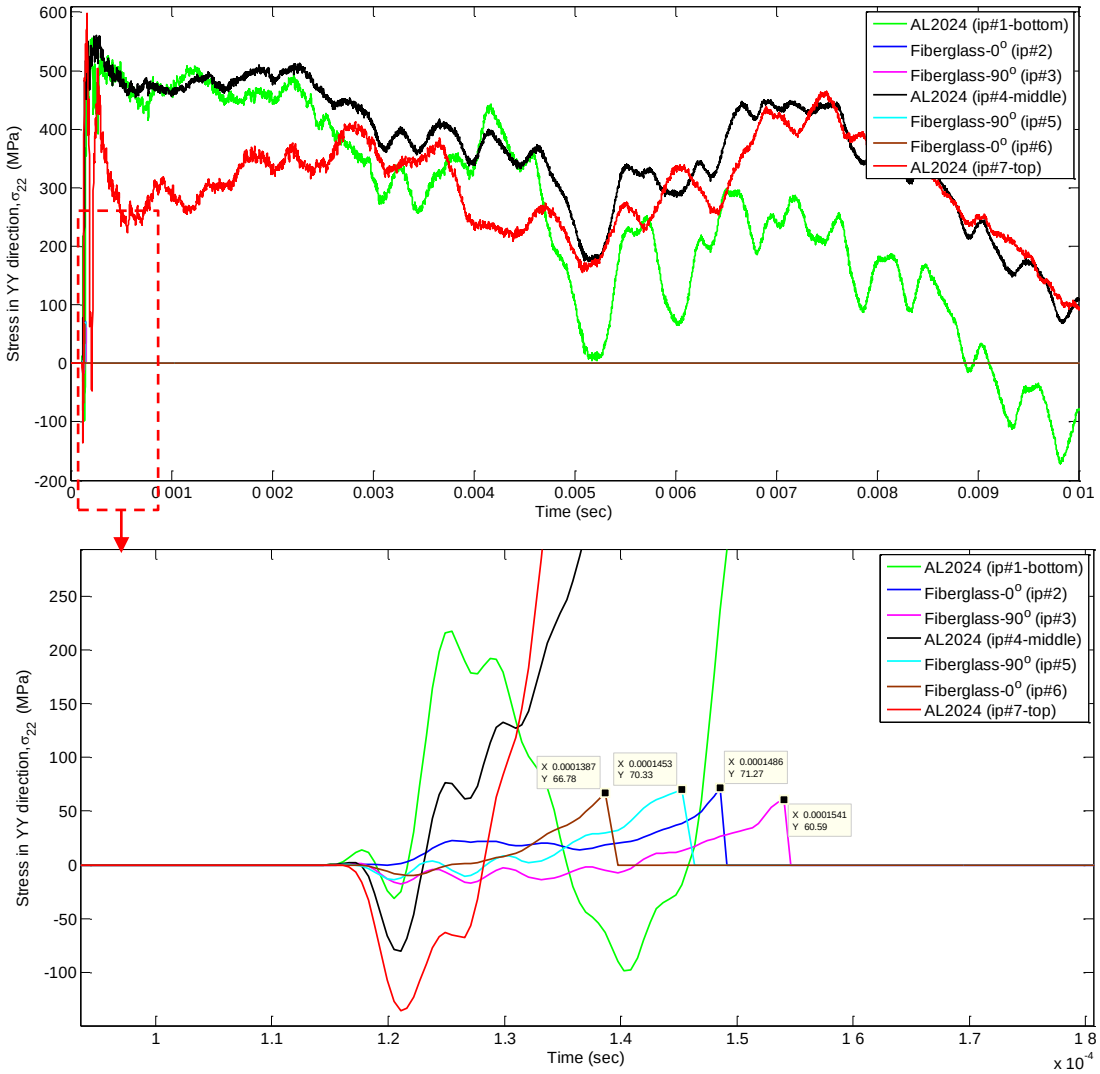

Figure 78 Stress in Y direction for bird impact at 116 m/s

From the Figure 78, it can be seen that the converged principal stress i.e. in this case is Y direction, when compared with the corresponding strength both Y_t = 75 MPa (tension strength transverse to the fibers) and Y_c =75 MPa (compression strength transverse to the fibres), then all the fiberglass composite plies failed in tension. The % difference with respect to Y_t is presented in Table 36. It can be concluded that the fiberglass plies 2, 5 and 6 have Y stress values near to the fiberglass material Y_t value and are between 4.97% and 10.96%.

Table 36 Ply stress in Y direction comparison with Y_t for bird impact at 116m/s

Ply #	Tension strength transverse to the fibers, Y_t	Stress in YY direction, σ_{22} (MPa)	% difference in comparison to Y_t
2	75	71.27	-4.97%
3	75	60.59	-19.21%
5	75	70.33	-6.23%
6	75	66.78	-10.96%

Figure 79 shows shear stress in XY direction or τ_{12} for each ply in the material local coordinate system.

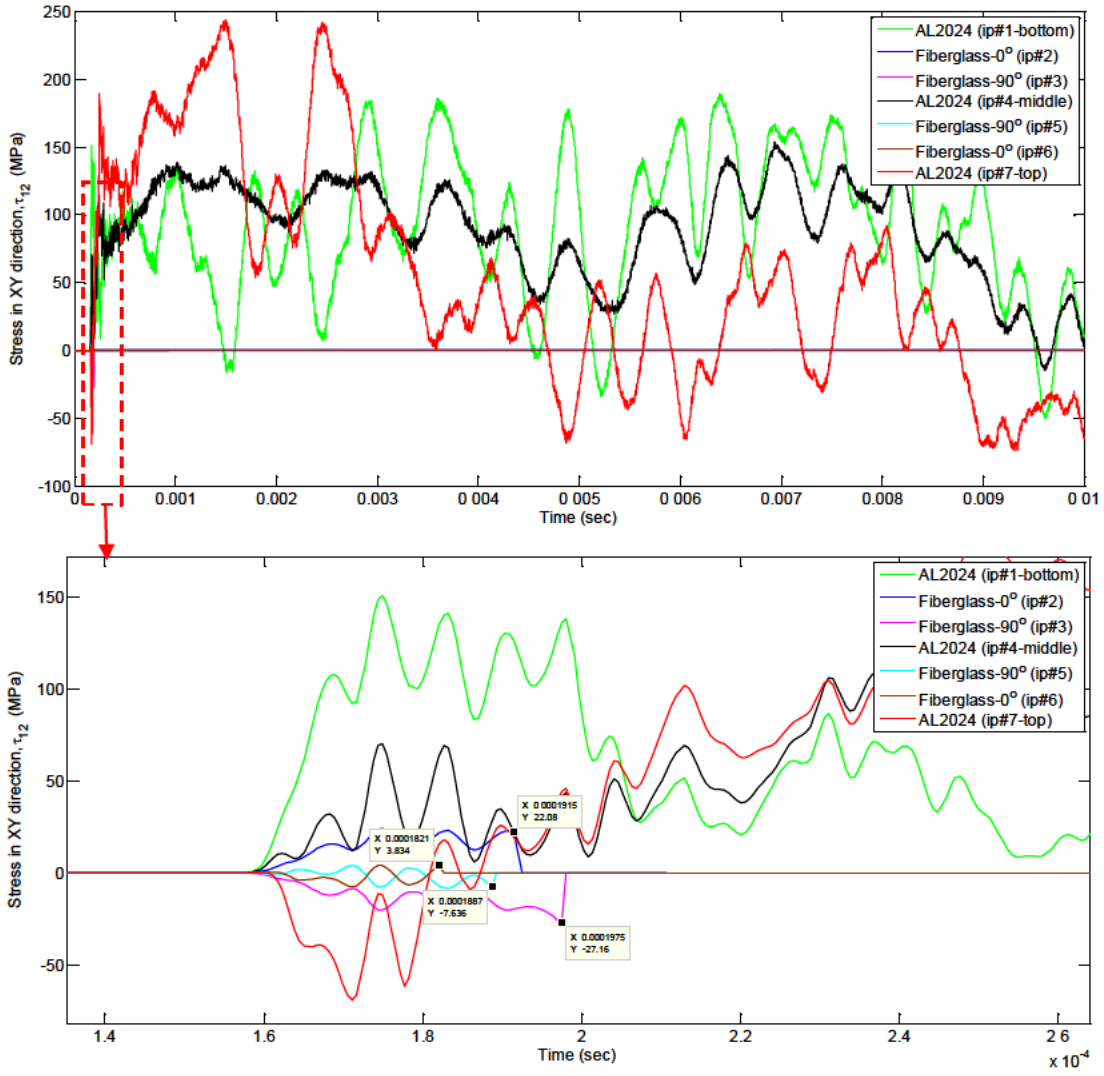

Figure 79 Shear stress in XY direction for bird impact at 116 m/s

From the Figure 79, it can be observed that the shear stress i.e. $|\tau_{12}|$ when compared with the corresponding pure shear strength of the material (S=75 MPa), then all the composite plies failed. The % difference with respect to S is represented in Table 37.

Table 37 Ply shear stress in XY direction comparison with S for bird impact at 116m/s

Ply #	Pure shear strength S (MPa)	Stress in XY direction, $\|\tau_{12}\|$ (MPa)	% difference in comparison to S
2	75	22.08	-70.56%
3	75	27.16	-63.79%
5	75	7.636	-89.82%
6	75	3.834	-94.89%

From the Table 36, it can be concluded that the % difference for shear stress, τ_{12} on each ply is between 70.56% and 94.89%, which is higher than the % difference obtained for the stresses in σ_{11} and σ_{22} directions. It is unclear why the % difference for shear stress is higher, and therefore, further investigation was undertaken considering the maximum principal stress on each composite ply and is shown in Figure 80. It can be seen that the highest principal stress is at the uppermost fiberglass composite ply 6 with 0° fiber orientation. Similar to the stress result in X direction (Figure 77), fiberglass plies 3, 5 and 6 failed at stress 682.5 MPa, 689.2 MPa and 718.3 MPa respectively. The result also shows a sensible relationship of stress flow with respect to time. The stress experienced by fiberglass ply #5 with 90° fiber orientation is 689.2 MPa, which fluttered to the bottom ply #3 (same 90° orientation) and similar stress of 682.5 MPa after 6.6E-6 s (6.6 µs) is observed.

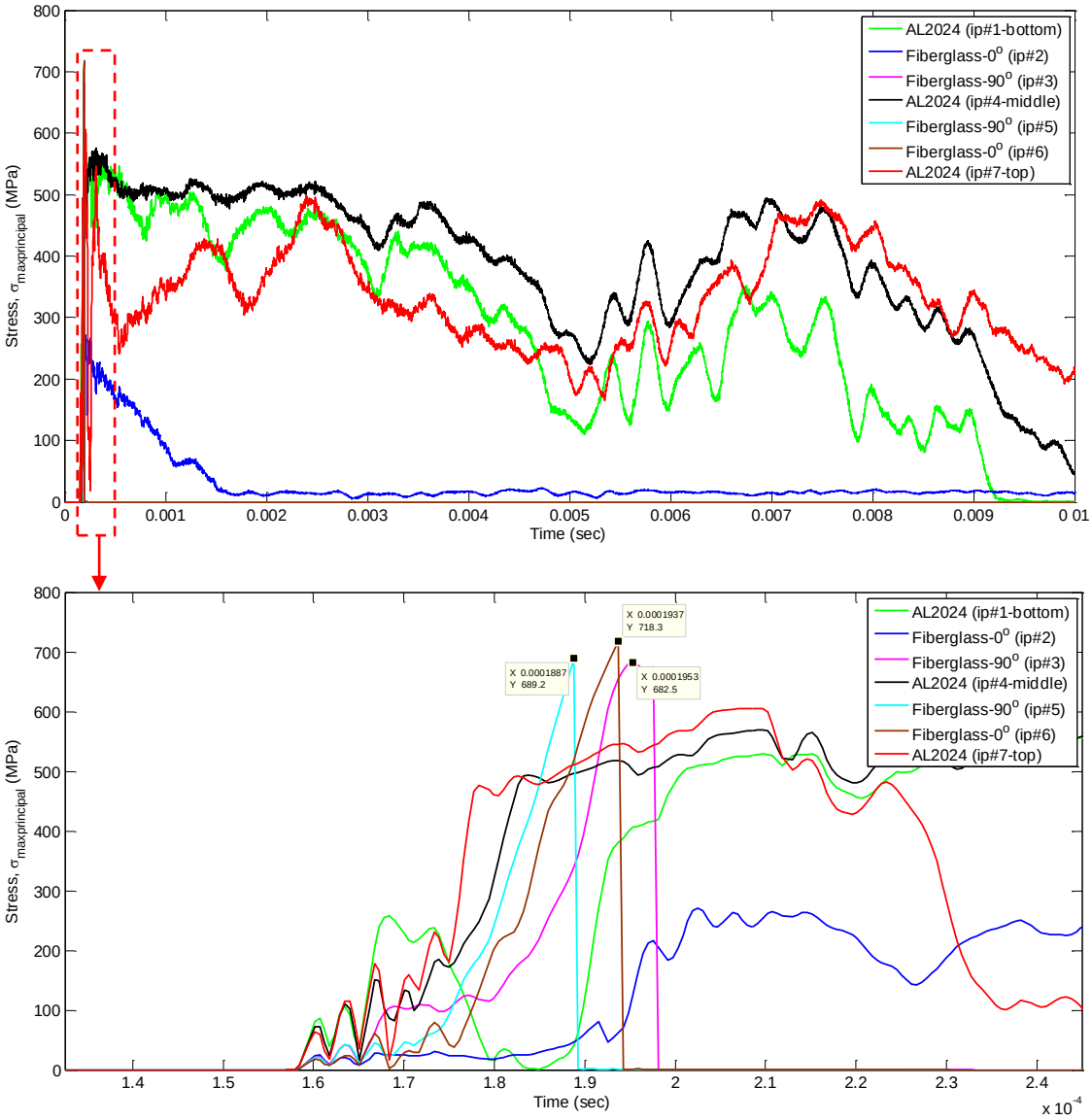

Figure 80 Composite plies maximum principal stress for bird impact at 116 m/s

In all of the stress results (presented in Figure 77,Figure 78,Figure 79 and Figure 80), aluminium alloy plies did not fail, even though the maximum principal stress exceeded the Al material yield strength of 369 MPa. Therefore, further investigation was performed on the ductile Al-2024 plies by considering von-Mises yield criterion. Von-Misses stress for isotropic materials is based on distortion energy theory, and Figure 81 shows the plot of Al-2024 stress vs plastic strain curve.

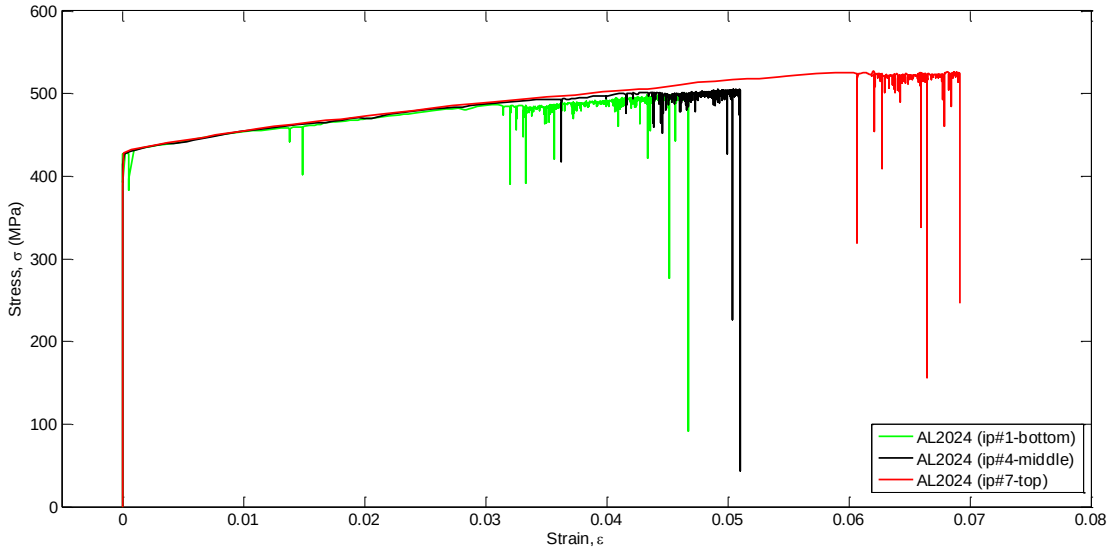

Figure 81 Al-2024 stress-strain curve for bird impact at 116 m/s

In the Figure 81, it is noted that the yield point of the aluminium alloy plies reached approximately 428 MPa, which is 16% higher than its yield strength of 369 MP. The 16% higher yield strength can be due to either Al-2024 hardening modulus value of 684 MPa or glass layers contributions to the strain rate effects that has been evident by McCarthy et al. (2005). The stress-strain curve began to deviate from the initial linear path and the plies continued to elongate with increased stress level due to the continuous reinforcement of laminate by the fiberglass plies (Guida 2008:50). As there are no experimental data available to validate the Al-2024 stress-strain curve profile (Figure 81) used in FML for a bird impact, experimental stress-strain curve was obtained from the tensile test performed on a FML at TU Delft by Vries and Vermeeren (1995) with similar material properties (Yield Strength=380 MPa, Young Modulus=72.4 GPa, Poisson ratio=0.33 and Shear modulus=27.2 GPa). This experimental stress-strain curve is presented in Figure 82. The aluminium stress-strain curve in longitudinal (L) or aluminium rolling direction is different from the transverse (LT) direction. It is due to the rolling process of the aluminium sheet, which gives a distinct difference in the yield value in the two directions (Hagenbeek 2005:42). Figure 82 is only used to compare the Al-2024 stress-strain curve profile obtained experimentally with this study numerical simulation curve, and not accentuate the difference in yield stress value of L and LT direction. Therefore, from the Figure 81 and Figure 82, it can be concluded that the numerical simulation aluminium alloy stress-strain curve profile correlates well with the experimental data. It is also noted that due to the presence of numerical noise, spikes of low stress values for increasing strain is evident, which should be ignored.

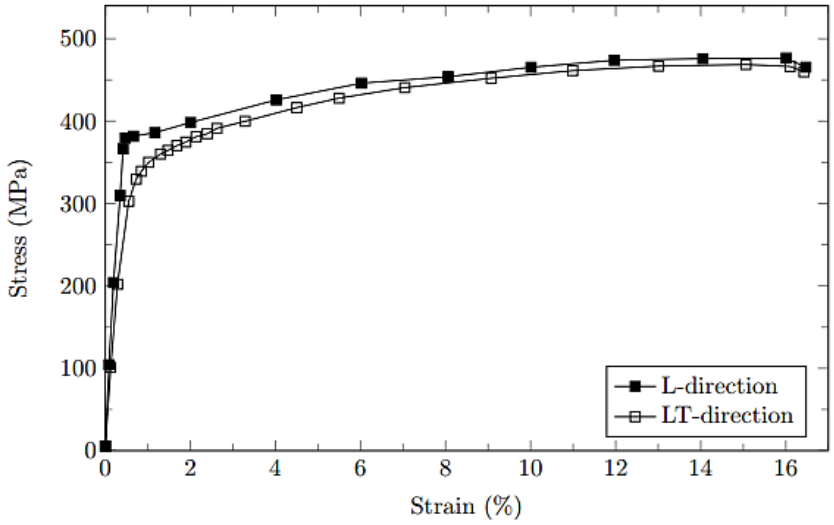

Figure 82 Experimental data given for the characterisation of the deformation of Al-2024-T3 material (Vries and Vermeeren 1995)

Further evaluation was made on the fiberglass composite plies MAT_022 material card using Chang-Chang failure criteria mentioned in the Section 3.9.3.5. Figure 83 shows the longitudinal tensile failure mode along the fibers, where 1 is for elastic and 0 is for failure.

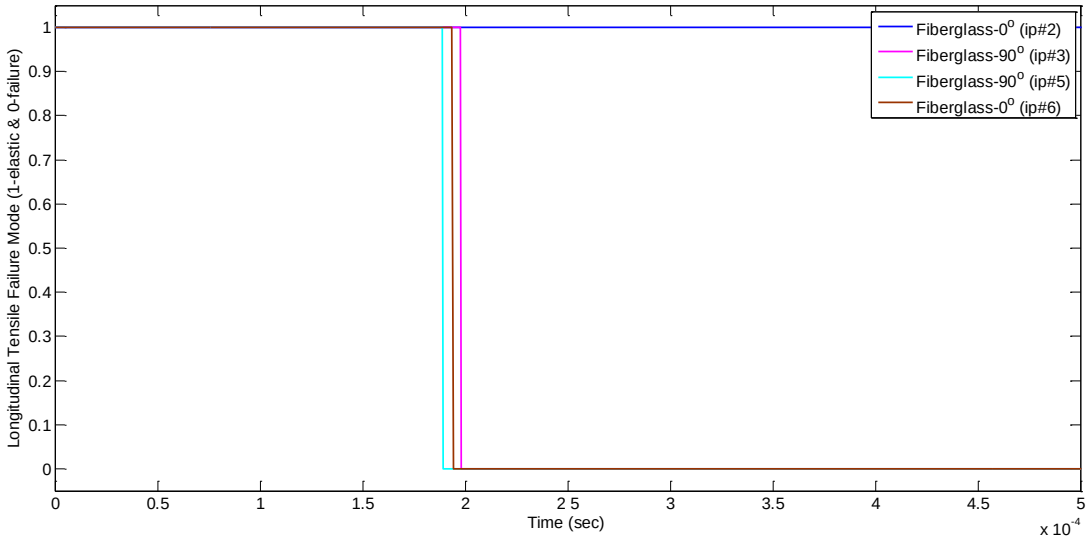

Figure 83 Fiberglass plies longitudinal tensile failure mode for bird impact at 116 m/s

From the Figure 83, it can be seen that the fibers in the ply 3, 5 and 6, which are the front plies of the wing failed under longitudinal tensile at time 2E-4 s (0.2 ms). Fiberglass ply 2 (the bottommost ply) with 0° fiber orientation retained its elastic property. The result (Figure 83) correlates well with stress result both in the X direction (Figure 77) and maximum principal (Figure 80), where all the fiberglass

composite plies failed, except ply 2. However, it is noted that the above analyses are performed on a single shell element at the centre of the impact, and therefore, the longitudinal tensile failure mode (green-elastic and red-failure) for the whole wing in d3plot at time t= 0.0006 s is presented in Figure 84. The time step is selected on the basis that the failure mode occurs at time=0.0002 s and the minimum time step used for d3plot database.

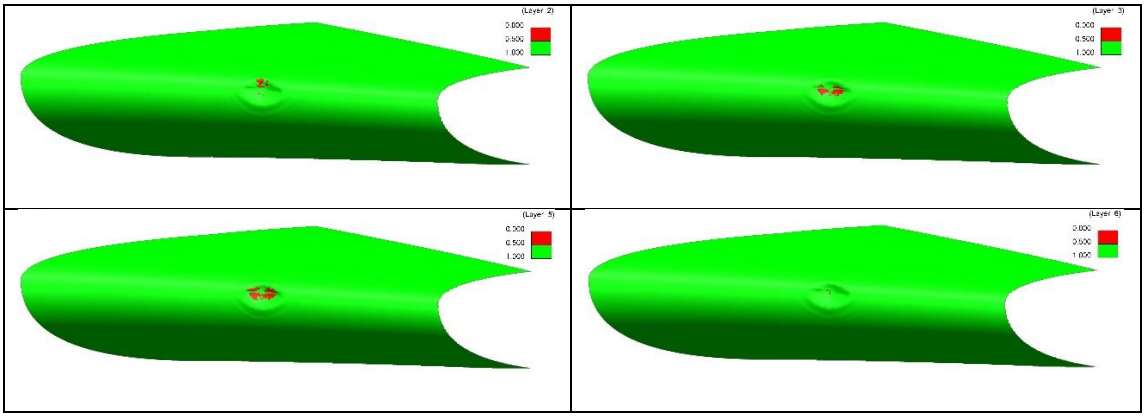

Figure 84 Longitudinal tensile failure mode d3plot for fiberglass plies (top left-ply2, top right-ply3, bottom left-ply5 and bottom right-ply6)

As presented in Figure 84, it can be concluded that the failure mode at the centre of impact (Figure 83) reflects well with the numerical result obtained for the whole wing. However, the chosen time t=0.0006 s, is appropriate only for this element (centre of impact) failure. Therefore, failure result for the whole wing at time t=0.0054 s, which is the time required by the bird total length to impact on the wing leading edge is presented in the Appendix 2.

Figure 85 shows the transverse tensile failure mode along the matrix for bird impact at 116 m/s. Compared to the longitudinal tensile failure mode, where fiberglass ply 2 only retained its elastic property, here in transverse tensile failure mode, plies 2, 5, and 6 failed; but ply 3 retained its elastic property. If this transverse tensile result is compared with the fiberglass plies failure under stress in Y direction (Figure 78), it can be seen that the ply 3 retained elastic property in Chang-Chang failure criteria but failed under stress in Y direction. It can be due to the stress in Y direction close to Y_t (material transverse tensile strength), whereas Chang-Chang failure criteria considers the transverse strength along the matrix, and not the fiber alone. It is also noted that the ply 3 stress in Y direction is 19.21% lower compared to Y_t, whereas

stress for other plies are in between 4.97% and 10.96%. Thus, the ply 3 should not have failed under stress in Y direction.

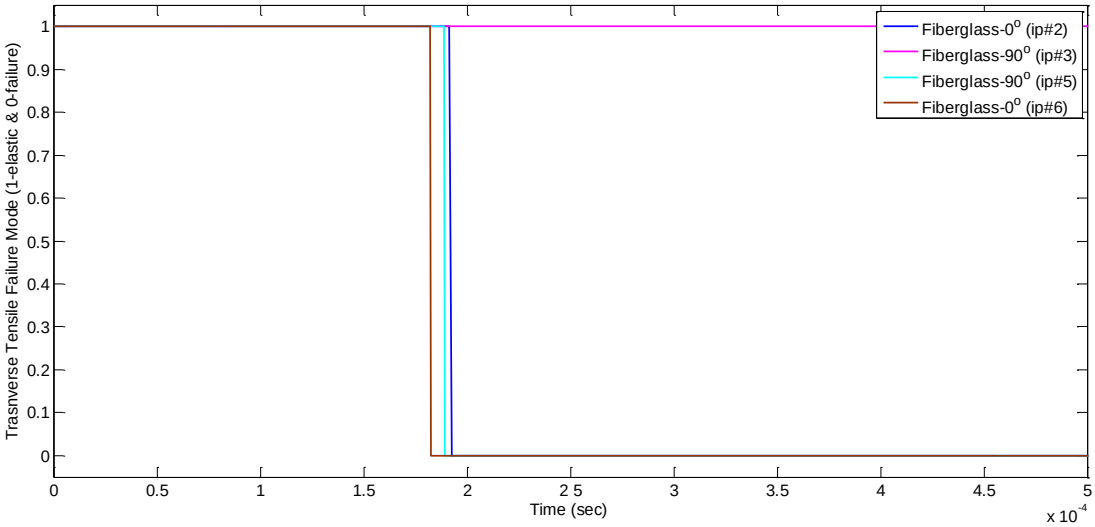

Figure 85 Fiberglass plies transverse tensile failure mode for bird impact at 116 m/s

Figure 86 below shows transverse compressive failure mode along the matrix. All the fiberglass plies retained their elastic property under transverse compression load along the matrix. It indicates that during the impact, the compression load on the matrix is not enormous, which can also be observed in Figure 78; where the fiberglass plies maximum stress in Y direction are in tension but minimal in compression.

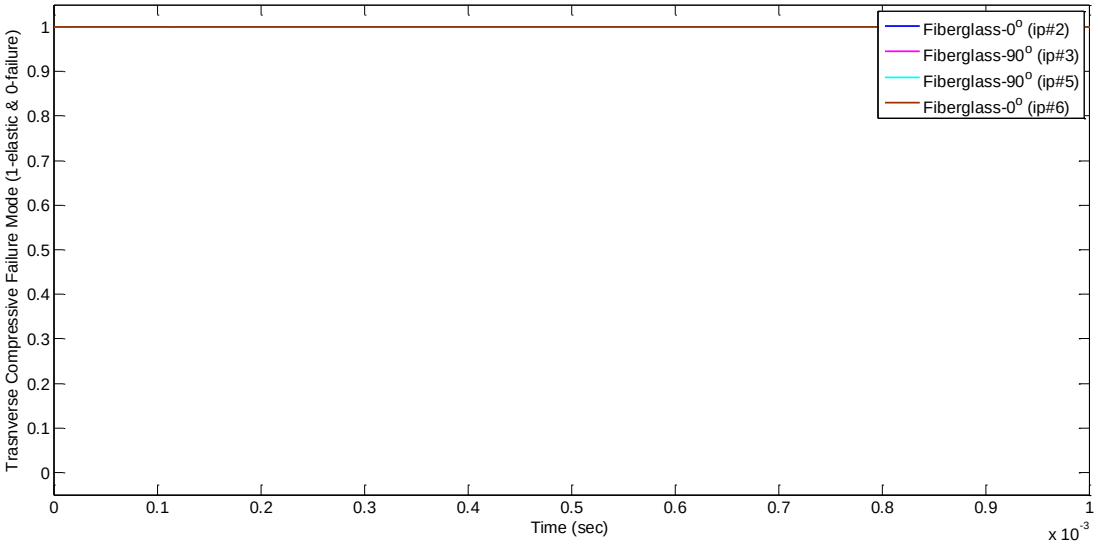

Figure 86 Fiberglass plies transverse compressive failure for bird impact at 116 m/s

The analyses (represented in Figure 85 and Figure 86) are performed on the shell element at centre of impact. The whole wing leading edge results for all the three orthotropic failure modes are provided in the Appendices (2, 3 and 4).

Displacement of the leading edge gives an indication of the structural deformation during an impact. The displacement at different time intervals with an increment of t=0.005 s till termination time of t=0.02 s is presented in Figure 87.

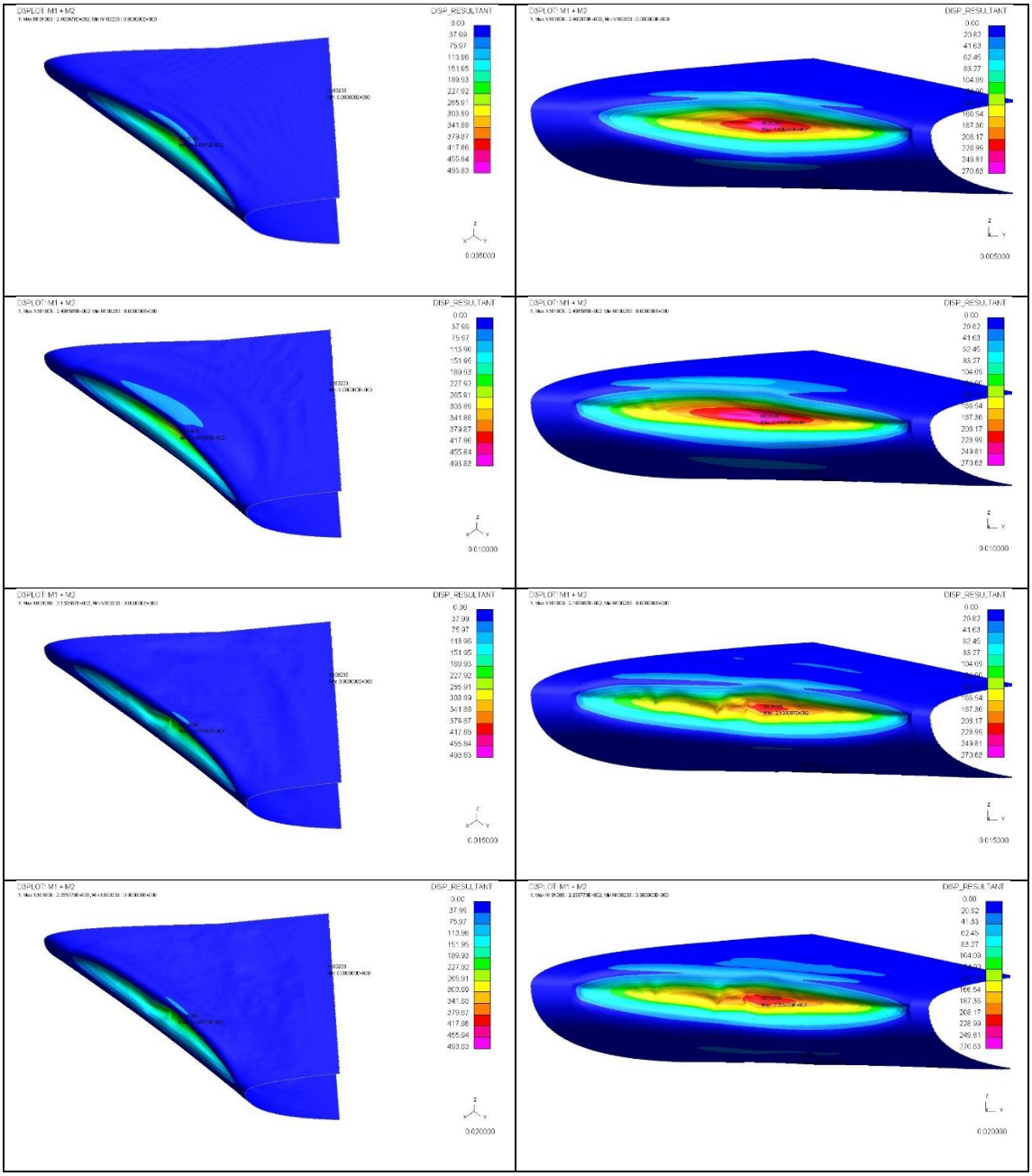

Figure 87 Displacement at different time steps for bird impact at 116 m/s

From the Figure 87, it can be seen that the composite leading edge did not suffer any perforation, and hence, there is no bird penetration through the wing leading edge. It can be concluded that the structure is able to absorb the bird impact energy without any failure. The maximum displacement noted is 270 mm at 0.0075 seconds (7.5 ms) and is shown in Figure 88.

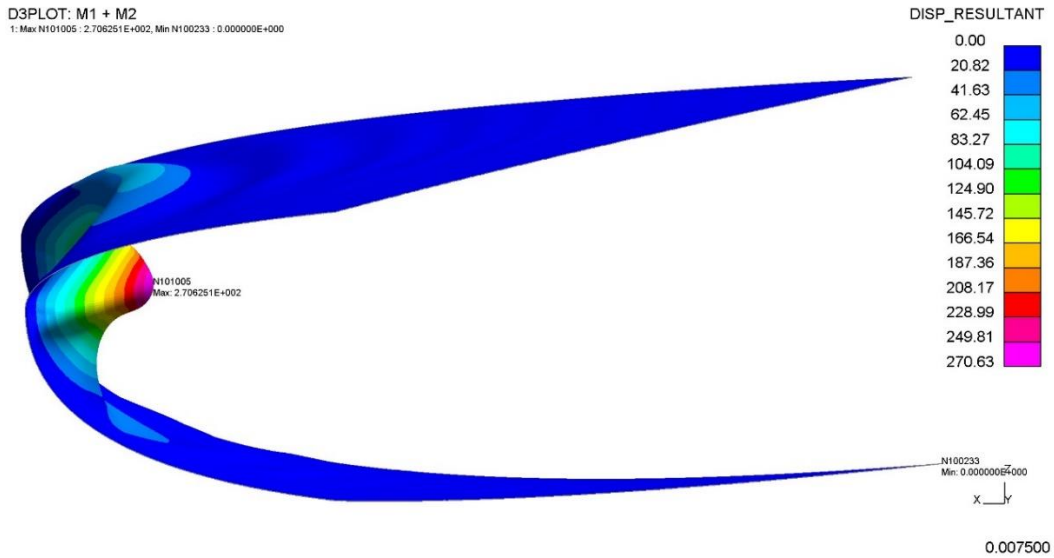

Figure 88 Maximum deformation of leading edge for bird impact at 116 m/s

The residual displacement for the node at centre of impact is found to be approx. 222.6 mm during the post-processing and is shown in Figure 89.

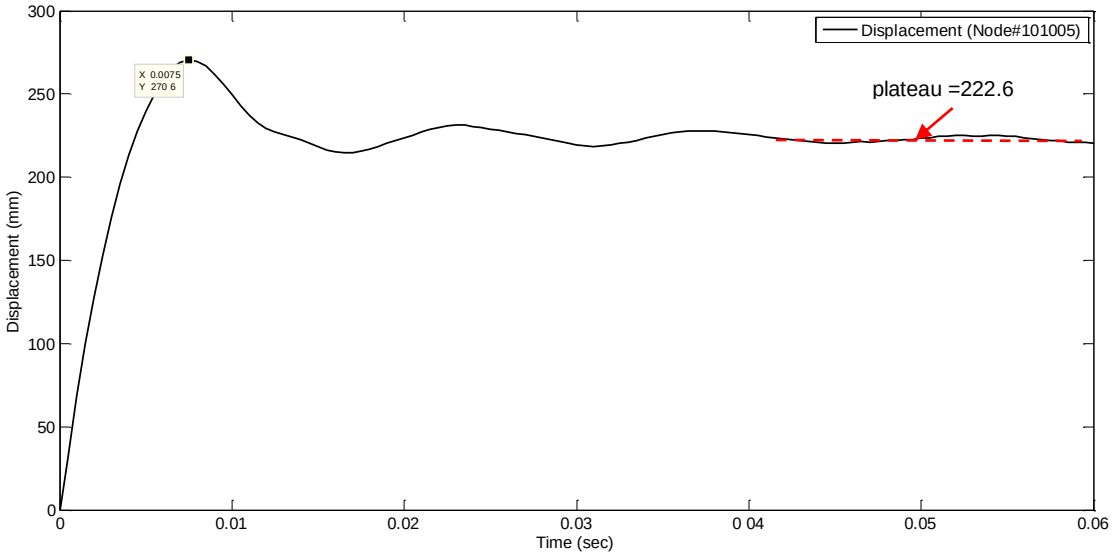

Figure 89 Residual displacement of wing leading edge for bird impact at 116 m/s

5.2 Test Case II– Bird Impact at 129 m/s (250 knots)

The second tests comprised of bird impact on the ribless leading edge at 129 m/s and Figure 90 shows the kinetic and internal of both bird and wing.

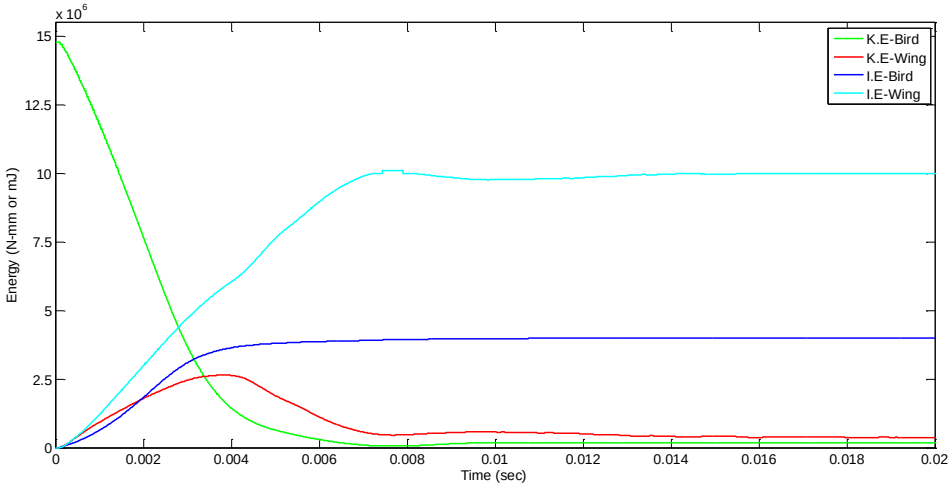

Figure 90 Kinetic and internal energy for bird impact at 129 m/s

From the Figure 90, it can be concluded that the initial K.E of the bird is 14.8E6 mJ (14,800 J) and reduced to a constant value of 0.18E6 mJ (180 J) at 0.0095 s (9.5 ms). The K.E numerical result from Guida et al. (2013) for an 8 lb (3.6 kg) bird impacting at 250 kts on FML was processed using image processing toolbox in MATLAB to keep the units consistent for comparison and is presented in Figure 91.

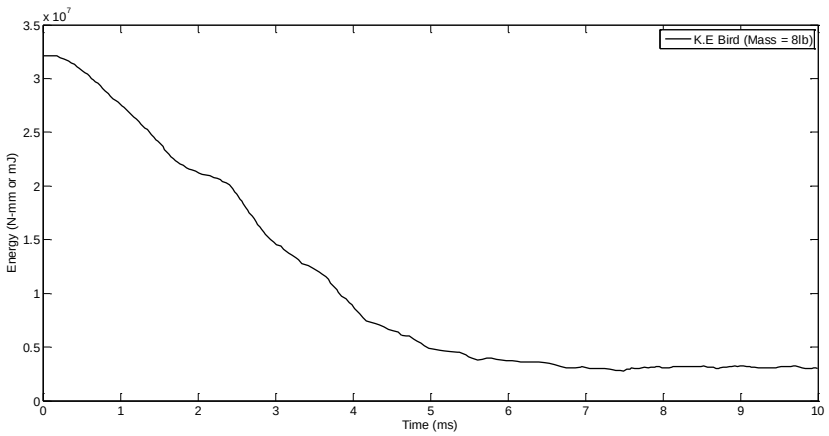

Figure 91 Kinetic energy for 8lb Bird impact at 250 kts on ribless wing leading edge (derived from Guida et al. 2013:112)

As seen in Figure 91, the initial bird kinetic energy is about 32E6 mJ (32,000 J), which is absorbed by the structural deformation in the LE. The KE dropped to a constant value at the end of impact, 3E6 mJ (3,000 J) at time 5E-3 s (5 ms). Table 38

shows comparison of the K.E change after impact obtained by Guida et al. (2013) for 3.6 kg (8 lb) bird with this research numerical result obtained for 1.81 kg (4lb) bird. It can be concluded that the change in K.E after the impact obtained from this study is proximate with a difference of 8% compared to the numerical result obtained by Guida et al. (2013). It is also noted that K.E reduction after the impact in numerical result obtained by Guida et al. (2013) was more because both Fiber Metal Laminate (FML) and Honeycomb core was used for the C-27J certification.

Table 38 Change in Bird KE after impact

Bird Mass	Initial K.E (N-mm)	K.E after impact (N-mm)	Change in K.E after the impact (N-mm)	% difference in bird KE after impact
8 lb (3.6 kg)	32E6	3E6	29	90%
4 lb (1.81 kg)	14E6	0.18E6	13.82	98%

Further analysis is performed in terms of the leading edge maximum deformation. The leading edge deformation experimental and numerical results obtained by Guida et al. (2013) are presented in Figure 92 and Figure 93 respectively. The maximum deformation recorded from the experimental test is approx. 150 mm (Figure 92). From Figure 93, it can be observed that the maximum numerical displacement of 150 mm correlates very well with the experimental result. The residual displacement obtained by the numerical simulation is 117 mm (Guida et al. 2013:111).

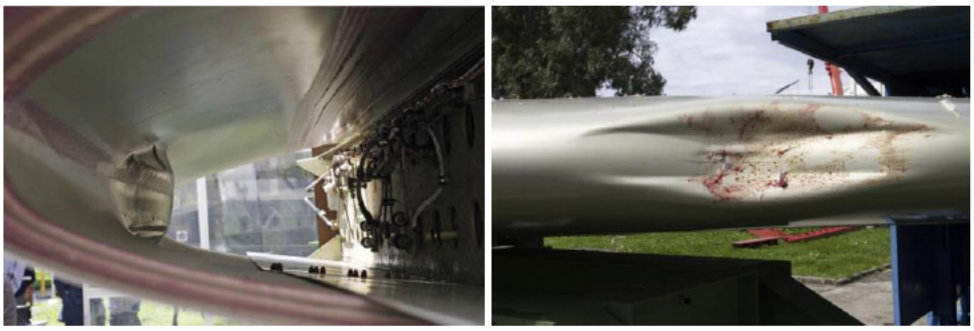

Figure 92 Leading edge deformation: experimental result (Guida et al. 2011:1066)

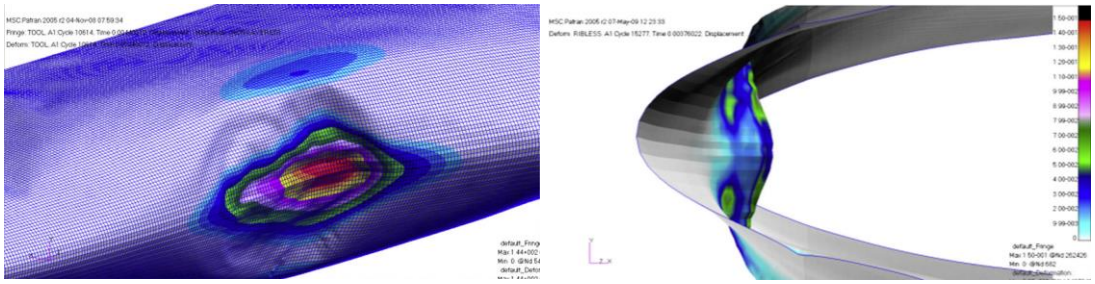

Figure 93 Leading edge deformation: numerical result (Guida et al. 2013:110)

The maximum deflection obtained from this research numerical simulation is 297 mm and is presented in Figure 94. The maximum displacement obtained is 98% higher in comparison to the Guida et al. (2013) numerical result.

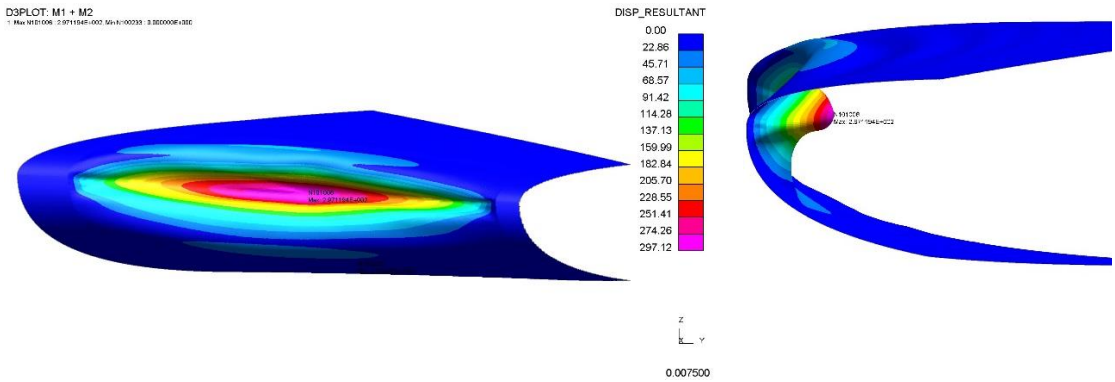

Figure 94 Maximum displacement of the leading edge for bird impact at 129 m/s

The residual displacement obtained is approx. 259.65 mm and is shown in Figure 95. It is 121% higher compared to the residual displacement obtained by Guida et al. (2013) for his numerical simulation. Such a high difference in the result is due to increase in the wing structure stiffness because of the additional layer of honeycomb core and inboard Al-2024 sheet used (Figure 35) for the C-27J certification.

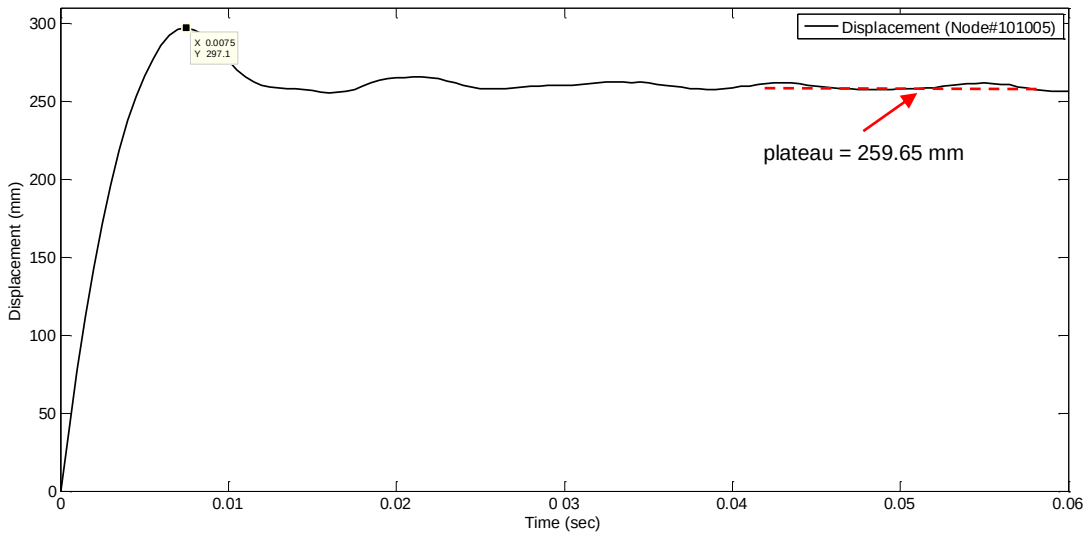

Figure 95 Residual displacement of wing leading edge for bird impact at 129 m/s

Furthermore, increase in the impact force is seen due to the high velocity and is presented in Figure 96. The peak contact force observed for bird impact at 116 m/s is 43,860 N, whereas the peak contact force observed for impact at 129 m/s is 55,070 N, which is an increase of 25.56% force for 11.21% increase in velocity. It is also noted that increase in velocity still leads to secondary peak contact force of 51,820 N but lower than the primary contact force of 55,070 N compared to impact at 116m/s.

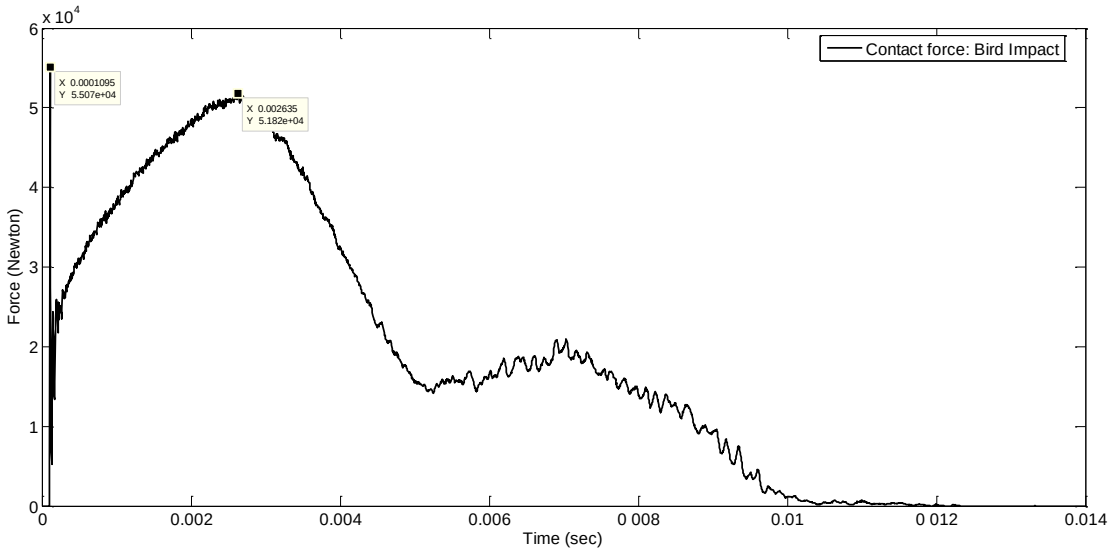

Figure 96 Force vs time history for bird impact at 129 m/s

The secondary contact force at 116 m/s velocity impact is 44,370N, higher than the primary force of 43,860 N. It is anticipated that the difference in the secondary contact force for impact at 116 m/s and 129 m/s can be due to the length of the bird

and the pressure of SPH particles effected by the shock wave and release waves mentioned in the Section 3.2 (Figure 8). At higher velocity, the shockwaves travelling in the opposite direction slows down the acceleration of the forward moving particles leading to lower secondary contact force. At lower velocity the shockwave travelling in the opposite direction still slows down the acceleration of the forward moving particles, but the shockwave pressure is less, and therefore, the number of SPH particles impacting on the wing surface area is higher leading to greater secondary contact force. Based on this assumption, it can be prophesied that the secondary contact force should be lower if the velocity is increased for the same bird length with same shape and properties.

Further analyses are made on the stresses observed in the X, Y direction and shear stress and is shown in Figure 97, Figure 98, and Figure 99 respectively. It can be seen that the fiberglass plies 3, 5 and 6 failed under tension in X direction, whereas all the fiberglass plies 2, 3, 5 and 6 failed under tension in Y direction. In shear stress all the fiberglass composite plies failed. The results obtained from these analyses are similar to the bird impact at 116 m/s.

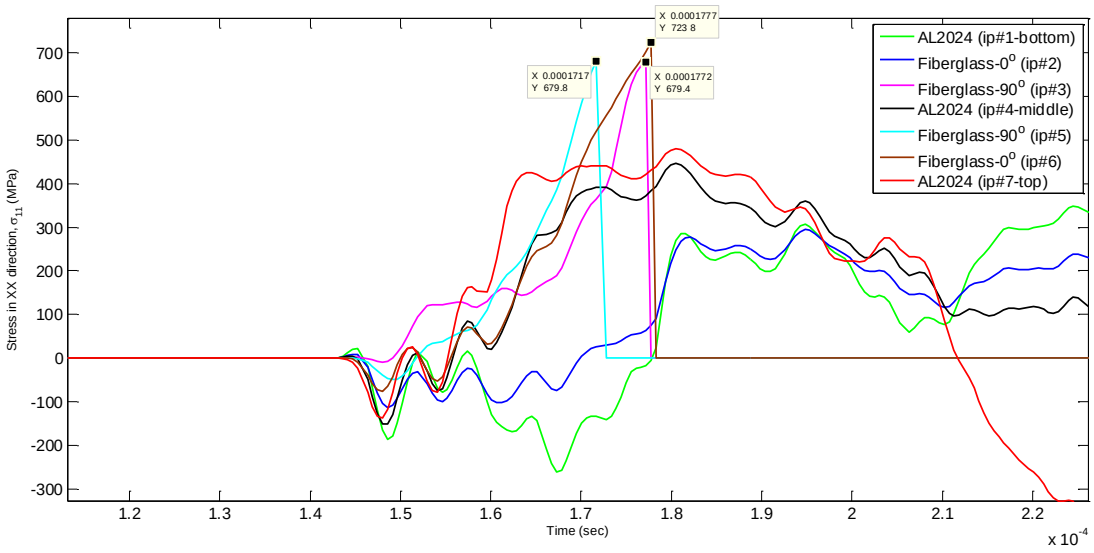

Figure 97 Stress in X direction for bird impact at 129 m/s

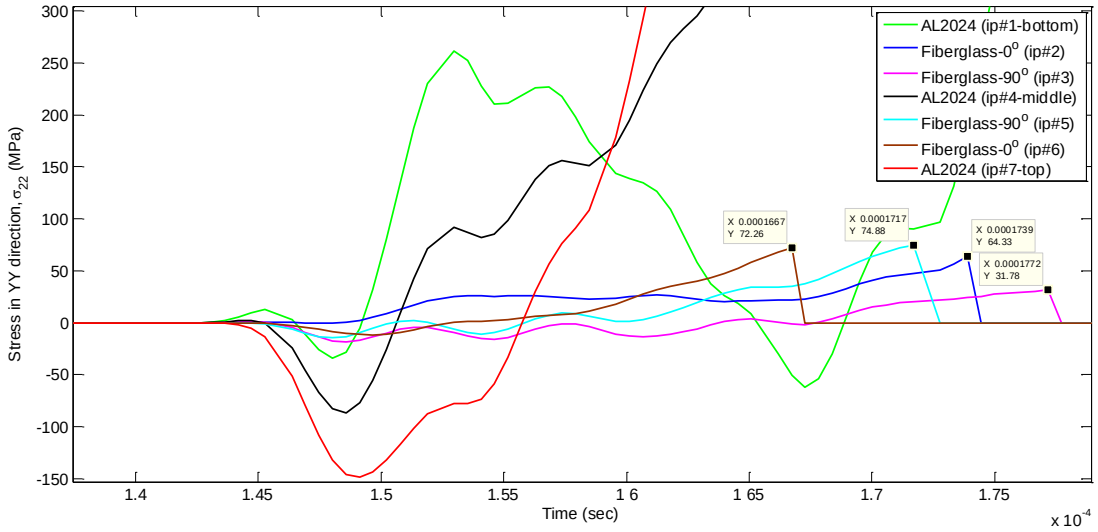

Figure 98 Stress in Y direction for bird impact at 129 m/s

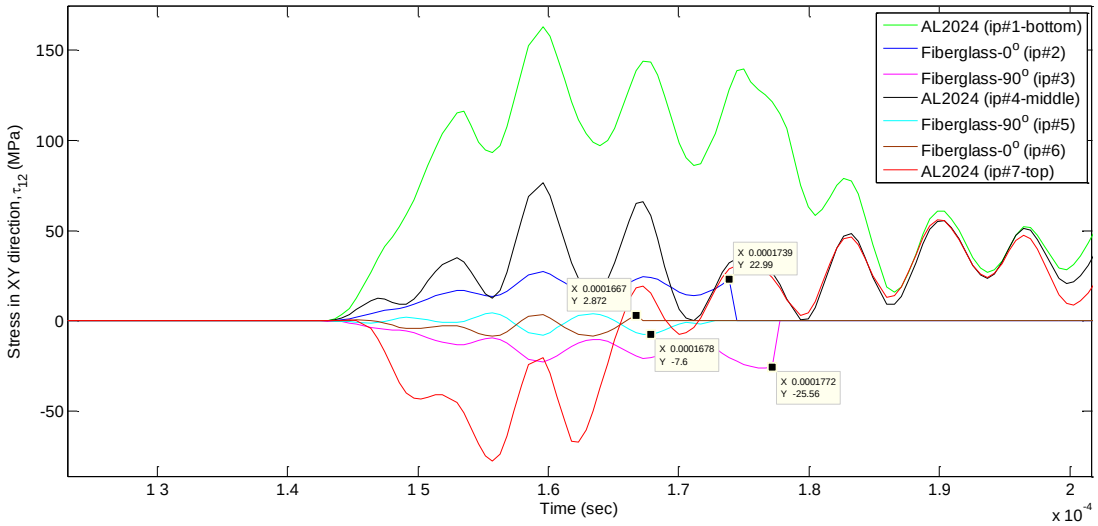

Figure 99 Shear stress in XY direction for bird impact at 129 m/s

The % difference in the stress for composite plies failure considering the maximum stress failure theory is presented in Table 39. It can be seen that the % difference for the fiberglass plies 3, 5, and 6 failures due to stress in X direction is close compared to longitudinal tensile strength (X_t). Fiberglass plies 2, 3, 5 and 6 failures due to stress in Y direction varies from 0.16% - 57.63% when compared to the material transverse tensile strength (Y_t). The % difference for stress in XY direction is higher in the range of 69.35% - 96.17% when compared to shear strength (S).

Table 39 Fiberglass plies failure % difference comparison with material strength for bird impact at 129 m/s

Ply #	Stress in X direction, σ_{11} (MPa)	% diff in comparison to X_t=725 MPa	Stress in Y direction, σ_{22} (MPa)	% diff in comparison to Y_t=75 MPa	Stress in XY direction, $\lvert\tau_{12}\rvert$ (MPa)	% diff in comparison to S=75 MPa
2	--	--	64.33	-14.23%	22.99	-69.35%
3	679.4	-6.29%	31.78	-57.63%	25.56	-65.92%
5	679.8	-6.23%	74.88	-0.16%	7.6	-89.87%
6	723.8	-0.17%	72.26	-3.65%	2.87	-96.17%

The highest principal stress of 723.8 MPa is observed by the fiberglass composite ply 6 and this can be seen from maximum principal stress vs time plot shown in Figure 100. The stress experienced by ply 6 is similar to the bird impact at 116 m/s, but 0.76% higher. It is also noted that the fiberglass plies 3, 5, and 6 failed at 680.5 MPa, 679.8 MPa and 723.8 MPa respectively.

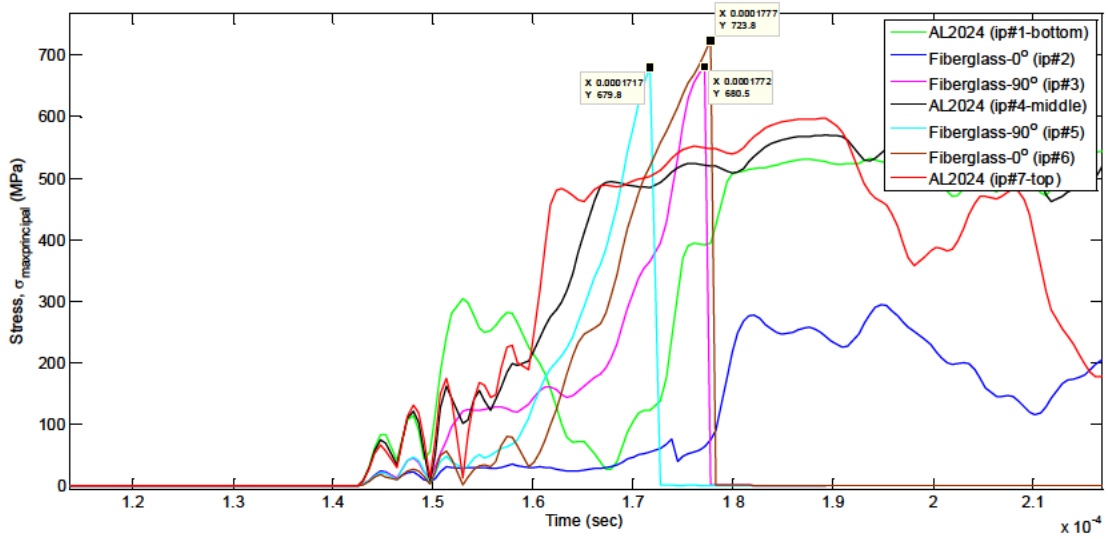

Figure 100 Maximum principal stress on each ply for bird impact at 129 m/s

The maximum principal stress of the aluminium plies again exceeded the applied material yield strength but still the plies did not fail. Therefore, further investigation was carried out by plotting Al-2024 stress-strain curve and is shown in Figure 101.

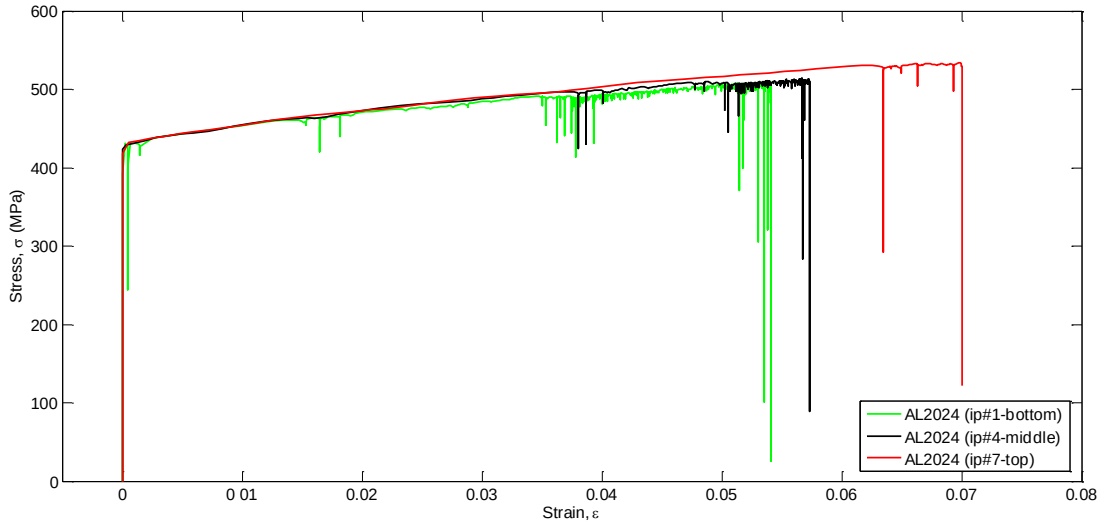

Figure 101 Al-2024 stress-strain curve for bird impact at 129 m/s

The stress-strain curve for bird impact at 129 m/s showed similar profile to that of impact at 116 m/s. The yield point of the aluminium alloy plies reached approximately 428 MPa, and the stress-strain curve shows plastic deformation. It is difficult to predict materials behaviour after it has plastically deformed, and hence aluminium plies are anticipated to fail. However, the failure of aluminium plies is not observed in the simulation as the bird SPH particles did not penetrate through the wing leading edge.

Furthermore, assessment was carried on the fiberglass composite plies considering Chang-Chang failure criteria. Figure 102, Figure 103 and Figure 104 shows longitudinal tensile failure mode along the fibers, transverse tensile and compressive failure mode along the matrix respectively. It can be seen that fiberglass composite plies 3, 5, and 6 failed under longitudinal tensile load along the fiber, and only ply 2 with 0^o fiber orientation retained its elastic property. The result of the longitudinal tensile load along the fiber correlates well with the fiberglass composite plies failure under stress in X direction (Figure 97), in which all the fiberglass plies failed, except ply 2. Under transverse tensile load along the matrix, fiberglass composite plies 2, 5 and 6 failed, whereas ply 3 with 90^o fiber orientation retained its elastic property. The transverse tensile load along the matrix correlates somewhat with the fiberglass composite plies failure under stress in Y direction (Figure 98), except the ply 3 failure. However, ply 3 have % difference of 57.63% compared to Y_t (material transverse tensile strength), and therefore, it should not fail under stress in Y direction. All the fiberglass composite plies 2, 3, 5 and 6 retained their elastic property under

transverse compressive load, which is also observed in Figure 98; where the plies failed only in tension and compression load is minimal. All the above three failure modes result for bird impact at 129 m/s on the wing leading edge at time t=0.0054 s are provided in the Appendices (5, 6 and 7). The failure behaviour of the fiberglass composite plies is similar to that of bird impact at 116 m/s and no penetration of the bird through the leading edge is evident.

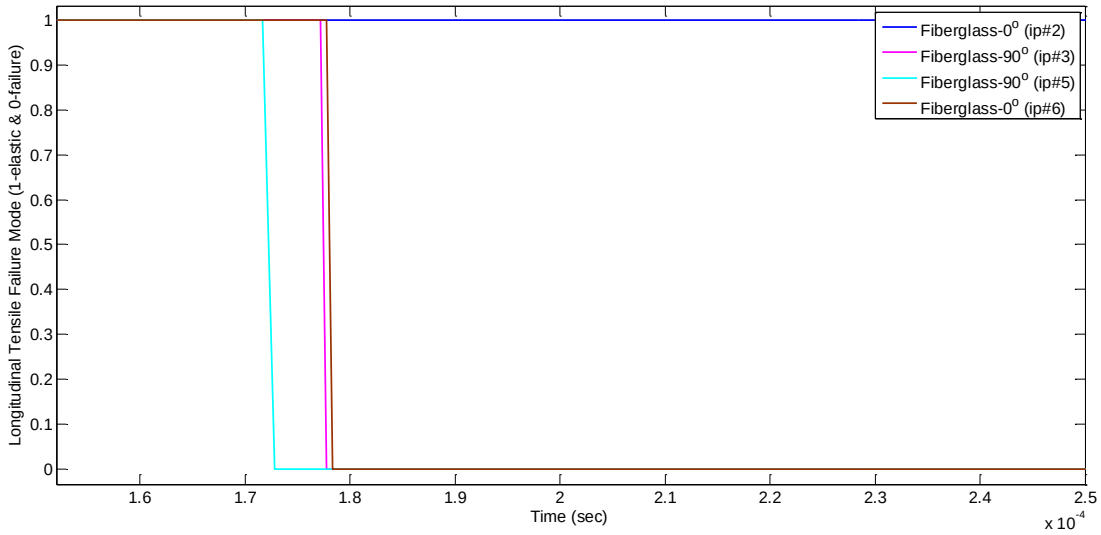

Figure 102 Fiberglass longitudinal tensile failure mode for bird impact at 129 m/s

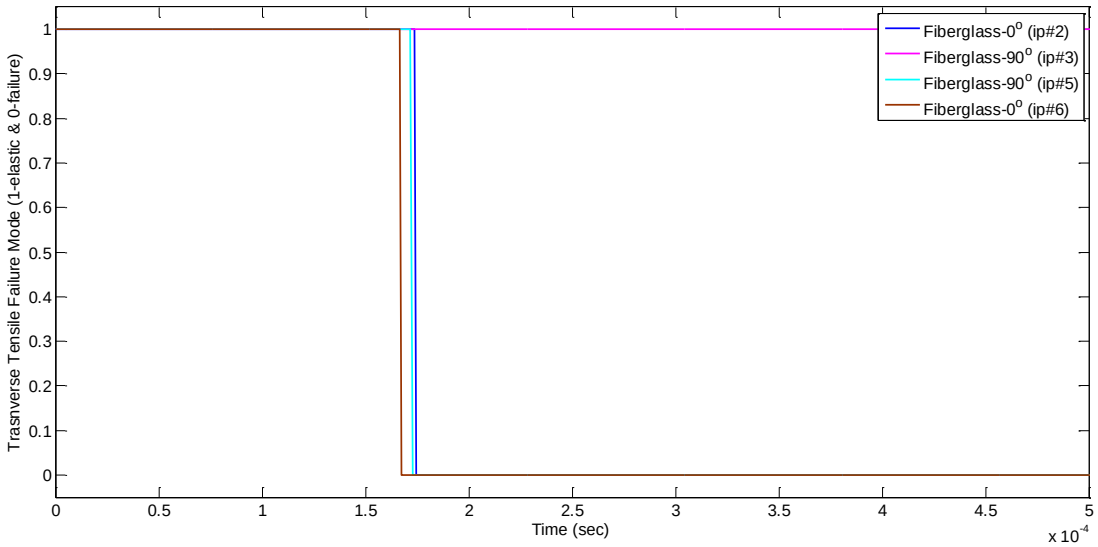

Figure 103 Fiberglass transverse failure mode for bird impact at 129 m/s

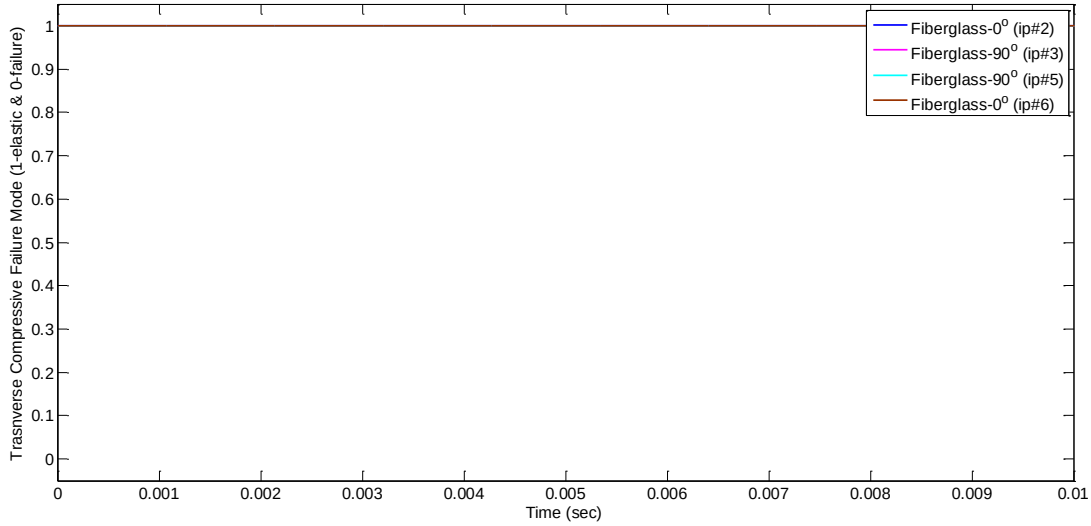

Figure 104 Fiberglass transverse compressive failure mode for bird impact at 129m/s

6. Conclusion and Recommendation

6.1 Summary and Conclusion

One of the main objectives of the study was to define and conduct a series of case studies to determine and analyse the failure criteria on the composite wing structure. To achieve this objective, the numerical bird has been modelled using Smooth Particle Hydrodynamics and Polynomial equation of state with different pitch values of 2.7mm, 2.8mm, 3mm, 3.2mm, 3.4mm and 4mm. The decision on the number of SPH particles and mass of each particle were dependent on the Mallard bird numerical model. The Hugoniot and Stagnation pressure obtained from all the above mentioned pitch values were validated with theoretical and Wilbeck (1977) experimental values at velocities 80 m/s, 116 m/s, 150 m/s and 225 m/s. Although no stagnation pressure experimental data was available for 1.81 kg (4lb) bird impact, stagnation pressure from 4 kg bird was used for reference purpose. The pitch value of 3.2 mm correlated well with the theoretical Hugoniot pressure as well as average of Hugoniot and Wilbeck (1977) experimental data and therefore was chosen for this study even though the number of SPH particles was 16.11% higher and mass of each particle was 67.32% higher than the Mallard bird numerical model.

Gulfstream G650ER aircraft wing simplified geometric model with aerofoil shape derived from Gulfstream III aircraft was used for this study. The ribless leading edge was numerically modelled using 2D shell elements and GLARE as material with A/0/90/A/90/0/A layup. The metal used was Aluminium alloy 2024 and composite was Glass Fabric (FM-94-27%-S2 Glass 187-460) with 0/90/90/0 fiber orientation and the total thickness of the leading edge was 1.4 mm. Effect of hourglass energy on both wing and bird model was also analysed and it was observed that the Type 4 Flanagan-Belytschko hourglass control card with coefficient value of 0.05 must be included to maintain the stability when deformation occurred in under integrated shell elements. Integration point database was also defined to collect stress and strain values for all the 7 plies and also to capture the Chang-Chang failure mode of the 4 glass fibreglass composite plies. Two test cases were considered for this study in which bird impacted the leading edge with velocities 116 m/s and 129 m/s. Bird impact at 116 m/s was performed to analyse the damage during the take-off or landing phase, whereas bird impact at 129 m/s was performed to compare the

damage with Guida et al. (2013) experimental and numerical results obtained from C-27J certification.

In the first test case, the bird SPH model was impacted normal to the ribless wing leading edge at velocity 116 m/s. The kinetic and internal energy of both bird and wing seems appropriate after the impact and stabilised after reaching a certain value. The contact force experienced by the wing leading edge during the bird strike seems reasonable and fluctuation was observed due to the mass of the bird being lumped at the nodes and non-homogenous shape of the bird. Maximum stress theory was considered to compare the result of each ply failure in X, Y and XY direction. The composite glass fiber plies 3, 5, and 6 failed in X direction whereas all the glass fiber plies 2, 3, 5 and 6 failed in Y and XY direction. Further analyses on the glass fiber composite plies were performed considering the Chang-Chang failure criteria and similar kind of observation was noted. Under longitudinal tensile load along the fiber, plies 3, 5 and 6 failed whereas ply 2 retained its elastic property similar to the results obtained for stress in X direction. However, plies 2, 5 and 6 failed under transverse tensile failure mode along the matrix whereas ply 3 retained its elastic property which somewhat correlates with the plies failure under stress in Y direction. Under transverse compressive load all the glass fiber plies retained their elastic property which was also observed for compression load result for stress in Y direction. The maximum deformation of the leading edge was 270.5 mm whereas the residual displacement was 222.6 mm.

In the second test case, bird SPH model was impacted normal to the ribless wing leading edge at velocity 129 m/s and the result was compared with the theoretical and experimental result available from Guida et al. (2013) performed for the certification of C-27J aircraft. The change in bird KE after impact correlates well with the Guida et al. (2013) numerical result with difference of 8%. The maximum and residual deformation of the leading edge were 297.1 mm and 259.65 mm respectively which were 98% and 121% more than the experimental result. However, this massive difference was predominantly due to total thickness of the C-27J leading edge which was 6.35 mm with addition of aluminium flex core and inboard aluminium alloy compared to total thickness of GLARE of 1.4 mm used for this study. Further analyses were performed considering the maximum stress theory and Chang-Chang failure criteria and similar results were obtained as the first test case.

In both the test cases, there was no penetration of the bird SPH particles observed through the wing leading edge which indicates that the structure was able to absorb the impact energy. However, there were no aluminium plies failure in any of the results even though the stress exceeded material's yield strength and this can be due to the strain hardening effect of the Johnson-Cook material card. This is an area where future work is recommended by the author.

6.2 Future Work

As part of the future work, the bird model can be improved by studying the effect of the length with the recommended pitch value of 3.2 mm to give SPH particles mass equal to that of the Mallard bird CT scan. Several studies have been carried out on the shape of the impact but no study has been performed with the pitch value of 3.2 mm which has been found to correlate well with the Wilbeck experimental and theoretical result in this study at four different velocities. It would also be interesting to study the effect of different shapes of the bird for example cylindrical bird model with single spherical end rather than both end as spherical. Another complex aspect of bird numerical modelling is introduction of void methodology which could be adopted for future study. This is basically a variation in meshing pattern which permits bird numerical model with cavities similar to mallard bird numerical model.

Aluminium alloy 2024 plies failure were not observed on any of the tests even at higher principal stress values. Therefore, it would be worth to analyse and compare the aluminium alloy ply failure study with other material cards such as MAT_013 (ISOTROPIC ELASTIC PLASTIC) or MAT_024 (PIECEWISE LINEAR PLASTICITY) and validate the results. MAT_022 (COMPOSITE DAMAGE) card used for fiberglass modelling is a simple card with three failure criteria. In order to analyse the composite ply failure extensively, MAT_054 (MAT ENHANCED COMPOSITE DAMAGE), which is an enhanced version of MAT_022 and indicates tensile and compressive failure both along the fiber and matrix can be used. One of the important aspects in laminate modelling is the adhesives used between the plies. In this study, inter-laminar failure was not embarked on, but can be considered as an important feature for future work.

7. Bibliography

Aerospace-Technology (2015) *GKN Aerospace to Supply Wing Skins for Gulfstream G500 Ad G600 Business Jets* [online] available from <http://www.aerospace-technology.com/news/newsgkn-aerospace-supply-wing-skins-gulfstream-g500-g600-business-jets-4560601> [06 June 2015]

Airoldi, A. and Cacchione, B. (2005) 'Numerical Analysis of Bird Impact on Aircraft Structures Undergoing Large Deformations and Localised Failure'. *Impact Loading on Lightweight Structures* 49

Airoldi, A. and Cacchione, B. (2006) 'Modelling of Impact Forces and Pressures in Lagrangian Bird Strike Analyses'. *International Journal of Impact Engineering* 32 (10), 1651-1677

Allan, R., and Orosz, A. (2001) *The Costs of Birdstrikes to Commercial Aviation* [online] available from <http://digitalcommons.unl.edu/birdstrike2001/2/> [20 February 2014]

Altair (2012) *CAE Driven Design Process* [online] available from < http://www.altairhyperworks.com/HWTemp1.aspx?top_nav_name=Concept%20Design&item_name=CAE%20Driven%20Design& > [22 January 2014]

Altair (2014) *Hyperworks 13.0* [online] available from < http://www.altairhyperworks.co.uk/HW/13/ > [14 June 2014]

Atkins Limited (2003) *Bird Strike Damage and Windshield Bird Strike* [online] available from <http://www.easa.europa.eu/rulemaking/docs/research/Final%20report%20Bird%20Strike%20Study.pdf> [12 January 2014]

Audic, S., Berthillier, M., Bonini, J., Bung, H., and Combesure, A. (eds.) (2000) *36th AIAA Joint Propulsion Conference and Exhibit*. 'A Prediction of Bird Impact in Hollow Fan Blades'. held 16-19 July at Huntsville. Alabama: AIAA

Australian Transport Safety Bureau. (2002) *The Hazard Posed to Aircraft by Birds* [online] available from < https://www.atsb.gov.au/media/43383/Hazard_aircraft_by_birds.pdf > [18 November 2014]

Barber, J., Taylor, J., and Wilbeck, J. (1978) *Bird Impact Forces and Pressures on Rigid and Compliant Targets*. Ohio: Air Force Flight Dynamics Laboratory

Bastien, C. (2015) *Application of Finite Element Analysis to Crashworthiness.* Unpublished booklet. Coventry: Coventry University

Boeing (2011) *Strategies for Prevention of Bird-Strike Events* [online] available from <http://www.boeing.com/commercial/aeromagazine/articles/2011_q3/4/> [13 February 2014]

Brockman, R. (1984) *Finite Element Analysis of Soft-Body Impact*. Ohio: Wright-Patterson Air Force Base

Buyuk. M., Kan, S. and Loikkanen, M. (2009) 'Explicit Finite Element Analysis of 2024-T3 Aluminium Material Under Impact Loading for Airplane Engine Containment and Fragment Shielding'. *Journal of Aerospace Engineering* 22 (3), 287-295

Campbell, F. C. (2010) *Structural Composite Materials*. Ohio: ASM International

CBS (2009) *US Airplane Crashes into Hudson River* [online] available from <http://wcbstv.com/breakingnewsalerts/us.airways.crash.2.909535.html> [21 June 2013]

Christensen, J (2014) *Introduction to Finite Element Analysis.* Unpublished booklet. Coventry: Coventry University

Citarella, R., Armentani, E., Sepe, R. and Caputo, F. (2014) *FEM Simulation of a FML Full Scale Aeronautic Panel Undergoing Static Load* [online] available from <http://www.omicsgroup.org/journals/fem-simulation-of-a-fml-full-scale-aeronautic-panel-undergoing-static-load-2169-0316.1000122.pdf> [09 June 2015]

Composites World (2015) *Flying High on Composite Wings* [online] available from <http://www.compositesworld.com/articles/flying-high-on-composite-wings> [20 June 2015]

Cornell, R. (1976) 'Elementary Three-Dimensional Interactive Rotor Blade Impact Analysis'. *Journal of Engineering Power* 98 (4), 480-6

Cossins, P. (2010) [online] available from <http://arxiv.org/abs/1007.1245v2> [11 October 2014]

Dar, U., Zhang, W. and Xu, Y. (2013) 'FE Analysis of Dynamic Response of Aircraft Windshield against Bird Strike Impact'. *International Journal of Aerospace Engineering*, 1-12

Early Aviators (n.d.) *Calbraith Perry Rodgers* [online] available from <http://www.earlyaviators.com/erodgers.htm> [16 June 2013]

EASA Certification Memorandum (2012) *Compliance with CS-25 Bird Strike Requirements* [online] available from <http://www.easa.europa.eu/certification/docs/certification-memorandum/'final'%20EASA%20CM-S-001%20Issue%2001_Compliance%20with%20CS-25%20bird%20strike%20requirements_PUBL.pdf> [28 January 2014]

Ensan, M., Zimcik, D., Lahoubi, M., Andrieu,D. (2007) 'Soft Body Impact Simulation on Composite Structures'. *Transactions of the Canadian Society for Mechanical Engineering* 07 (66), 283-296

Flightglobal (2015) *Flight Test: Gulfstream goes farther and faster with G650ER* [online] available from < http://www.flightglobal.com/news/articles/flight-test-gulfstream-goes-farther-and-faster-with-409557/ > [20 June 2015]

Georgiadis, S., Gunnion, A. J., Thomson, R. S., and Cartwright, B. K. (2008) 'Bird-Strike Simulation for Certification of the Boeing 787 Composite Moveable Trailing Edge'. *Composite Structures* 86 (1–3), 258-268

Goswami, P. and. Pajarola, R. (2011) *Time Adaptive Approximate SPH* [online] available from <http://maverick.inria.fr/~Prashant.Goswami/Research/Papers/VRIPHYS11_TAASPH.pdf> [20 June 2014]

Guida, M. (2008) *Study Design and Testing of Structural Configurations for the Bird Strike Compliance of Aeronautical Components* [online] available from <http://www.fedoa.unina.it/3190/1/Guida_doctoral_thesis_Study_Design_and_Testing_of_Structural_Configurations_for_the_bird-strike_compliance_of_aeronautical_components.pdf> [23 September 2014]

Guida, M., Marulo, F., Meo, M., Grimaldi, A., and Olivares, G. (2011) 'SPH – Lagrangian Study of Bird Impact on Leading Edge Wing'. *Composite Structures* 93 (3), 1060-1071

Guida, M., Marulo, F., Meo, M., and Russo, S. (2013) 'Certification by Birdstrike Analysis on C27J Fullscale Ribless Composite Leading Edge'. *International Journal of Impact Engineering* 54 (0), 105-113

Gulfstream (2015) *The Gulfstream G650ER* [online] available from <http://www.gulfstream.com/aircraft/gulfstream-g650er> [22 June 2015]

Guo, Y., Jia, P., and Hong, G. (2012) 'Research on Bird Strike Simulation of Composite Leading Edge'. *AASRI Procedia* 3 (0), 674-679

Hachenberg, D., Graf, O., Leopold, T. (ed.) (2003) *2nd EADS Workshop on Crash and Impact Simulation*. 'Comparison of Different Approaches for Bird Strike Simulation'. held December 11 at Germany

Hagenbeek, M. (2005) *Characterisation of Fiber Metal Laminates Under Thermo-Mechanical Loadings*. Netherlands: TU Delft

Hanssen, A. G., Girard, Y., Olovsson, L., Berstad, T., and Langseth, M. (2006) 'A Numerical Model for Bird Strike of Aluminium Foam-Based Sandwich Panels'. *International Journal of Impact Engineering* 32 (7), 1127-1144

Hedayati, R. and Ziaei-Rad, S. (2013) 'A New Bird Model and the Effect of Bird Geometry in Impacts from various Orientations'. *Aerospace Science and Technology* 28 (1), 9-20

Hedayati, R., Sadighi, M., and Mohammadi-Aghdam, M. (2014) 'On the Difference of Pressure Readings from the Numerical, Experimental and Theoretical Results in Different Bird Strike Studies'. *Aerospace Science and Technology* 32 (1), 260-266

Heimbs, S. (2011) 'Computational Methods for Bird Strike Simulations: A Review'. *Computers & Structures* 89 (23–24), 2093-2112

Homebuilt Airplanes (2003) *Bird Strikes and what Building Material are Best?* [online] available from <http://www.homebuiltairplanes.com/forums/aircraft-design-aerodynamics-new-technology/15203-bird-strikes-what-building-material-best.html> [11 February 2014]

Huertas, C. (2010) *Robust Bird-Strike Modelling using LS-Dyna*. Germany: VDM Verlag

Maragakis, I. (2009) *Bird Population Trends and their Impact on Aviation Safety 1999-2008* [online] available from <http://easa.europa.eu/essi/documents/EASAReportBirdpopulationandimpact.pdf> [16 January 2014]

Ivancevic, D. and Smojver, I. (2011) 'Hybrid Approach in Bird Strike Damage Prediction on Aeronautical Composite Structures'. *Composite Structures* 94 (1), 15-23

Johnson, A. F. and Holzapfel, M. (2003) 'Modelling Soft Body Impact on Composite Structures'. *Composite Structures* 61 (1–2), 103-113

Kassapoglou, C. (2010) *Design and Analysis of Composite Structures*. Chichester: Wiley

Kermanidis, T., Labeas, G., Sunaric, M., and Ubels, L. (2005) 'Development and Validation of a Novel Bird Strike Resistant Composite Leading Edge Structure'. *Applied Composite Materials* 12 (6), 327-353

Kumar, N., Kumar, M., Krishna, V. and Rao, D. (2013) 'Experimental Investigation on Mechanical Properties of Coal Ash Reinforced Glass Fiber Polymer Matrix Composites'. *International Journal of Emerging Technology and Advanced Engineering* 3 (8), 250-258

Lacome, J. (ed.) (2001) *FEA Information International News for the World-Wide Engineering Community*. 'Smooth Particle Hydrodynamics - Part II'. held November 2001

Lawson, M., and Tuley, R. (1987) *Supercomputer Simulation of a Birdstrike on a Turbofan Aero Engine*. Derby: Rolls Royce

Liu, J., Li, Y. L., and Xu, F. (2008) 'The Numerical Simulation of a Bird-Impact on an Aircraft Windshield by using the SPH Method'. *Advanced Materials Research* 33, 851-856

Liu, J. and Li, Y. (2013) 'Numerical Simulation of a Rotary Engine Primary Compressor Impacted by Bird'. *Chinese Journal of Aeronautics* 26 (4), 926-934

Liu, J., Li, Y., and Gao, X. (2014) 'Bird Strike on a Flat Plate: Experiments and Numerical Simulations'. *International Journal of Impact Engineering* 70, 21-37

Liu, J., Li, Y., Gao, X., and Yu, X. (2014) 'A Numerical Model for Bird Strike on Sidewall Structure of an Aircraft Nose'. *Chinese Journal of Aeronautics* 27 (3), 542-549

LSTC. (2012) *Modeling of Composites in LS-DYNA* [online] available from < ftp://ftp.lstc.com/outgoing/jday/composites/mat_comp.pdf > [18 June 2015]

LSTC (2014) *LS-DYNA Support: Theory Manual* [online] available from < http://www.dynasupport.com/manuals > [07 January 2015]

Lucy, L. (1977) 'A Numerical Approach to the Testing of the Fission Hypothesis'. *Astronomical Journal* 82, 1013

Mao, R., Meguid, S., and Ng, T. (2008) 'Transient Three Dimensional Finite Element Analysis of a Bird Striking a Fan Blade'. *International Journal of Mechanics and Materials in Design* 4 (1), 79-96

Martinez, F., Rico, G., Franganillo, A., and Climent, H. (eds.) (1995) *ABAQUS Users' Conference*. 'Bird Impact on an Aircraft Leading Edge'. held 31 May - 2 June at Paris. France: Dassault Systems

Martinez, J., Rusinek, A., and Arias, A. (2011) 'Thermo-Viscoplastic Behaviour of 2024-T3 Aluminium Sheets Subjected to Low Velocity Perforation at Different Temperature'. *Thin-Walled Structures* 49 (7), 819-832

McCallum, S.C., and Constantinou, C. (ed.) (2005) *5th European LS-DYNA Users Conference*. 'The Influence of Bird-Shape in Bird-Strike Analysis' at Birmingham UK

McCarthy, M., Xiao, J., McCarthy, C., Kamoulakos, A., Ramos, J., and Gallard, J. (2005) 'Modelling Bird Impacts on an Aircraft Wing Part 2: Modelling the Impact with an SPH Bird Model'. *Applied Composite Materials* 11 (5), 317-340

McCarty, R. (ed.) (1979) *International Proceedings of the 17th Annual SAFE Symposium*. 'Computer Analysis of Bird-Resistant Aircraft Transparencies'. held 2 December at Las Vegas. Nevada: SAFE Association

McCarty, R. (ed.) (1980) *International Proceedings of the 21st AIAA Structures, Structural Dynamics and Material Conference*. 'Finite Element Analysis of F-16 Aircraft Canopy Dynamic Response to Bird Impact Loading'. held May 12-14 at Seattle. Washington: AIAA

Megson, T. H. G. (2007) *Aircraft Structures for Engineering Students*. 4th ed. Burlington; Oxford: Burlington: Elsevier Science

Meguid, S. A., Mao, R. H., and Ng, T. Y. (2008) 'FE Analysis of Geometry Effects of an Artificial Bird Striking an Aeroengine Fan Blade'*. International Journal of Impact Engineering* 35 (6), 487-498

Mithun, N. and Mahesh, G. (2012) 'Finite Element Modelling for Bird Strike Analysis and Review of Existing Numerical Methods'*. International Journal of Engineering Research & Technology (IJERT)* 1 (8), 1-8

Nayak, N. (2014) 'Composite Materials in Aerospace Applications'*. International Journal of Scientific and Research Publications* 4 (9), 1-10

Nizampatnam, L. (2007) *Models and Methods for Bird Strike Load Predictions* [online] M.S dissertation. Wichita State University. available from < http://soar.wichita.edu:8080/bitstream/handle/10057/1494/d07030.pdf?sequence=1 > [19 November 2014]

Nomenclaturo (2007) *Airplane Wing* [online] available from <http://www.nomenclaturo.com/tag/airplane-wing> [18 February 2014]

Olovsson, L. and Souli, M. (eds.) (2000) *6th International LS-DYNA Users Conference*. 'ALE and Fluid-Structure Interaction Capabilities in LS-Dyna' at Detroit. California: Livermore Software Technology Corporation

Reuters (2014) *Rolls Royce seeks long-term uplift with new aero engines* [online] available from < http://uk.reuters.com/article/uk-rollsroyce-engines-idUKBREA1P1TN20140226 > [04 April 2014]

RGN (2014) *Bird Strikes have Big Safety and Financial Impact* [online] available from <http://www.runwaygirlnetwork.com/2014/02/19/bird-strikes-have-big-safety-and-financial-impact/> [22 February 2014]

Schuette, W. (ed.) (1990) *Proceedings of the 5th International Conference of Science and Engineering on Supercomputers*. 'Blade Behaviour during Bird Strike'. England: WIT Press

Shmotin, Y. and Chupin, P. and Ryabov, A. (eds.) (2009) *7th Europan LS-DYNA Conference*. 'Bird Strike Analysis of Aircraft Engine Fan' at Germany

Simulia (2011) *Bird Strike Simulations on Composite Aircraft Structures* [online] available from <http://www.simulia.com/download/scc-papers/Aerospace/bird-strike-simulations-on-composite-aircraft-2011-F.pdf> [01 March 2014]

Smith, O. (2012) *Nepal Plane Crash: The Ongoing Threat of Bird Strikes* [online] available from <http://www.telegraph.co.uk/travel/travelnews/9573381/Nepal-plane-crash-the-ongoing-threat-of-bird-strikes.html> [25 January 2014]

Smojver, I. and Ivancevic, D. (2011) 'Bird Strike Damage Analysis in Aircraft Structures using Abaqus/Explicit and Coupled Eulerian Lagrangian Approach'. *Composites Science and Technology* 71 (4), 489-498

Strand7 (2012) *ST7-1.10.10 Linear / Statics Webnotes* [online] available from < http://www.strand7.com/webnotes/ST7-1.10.htm#ST7-1.10.10 > [04 February 2014]

Thorpe, J. (2003) *Fatalities and Destroyed Civil Aircraft due to Bird Strike, 1912-2002* [online] available from <http://tinyurl.com/qzsm2oo> [20 June 2014]

Triumph Group Inc (2015) *Wings: Triumph Aerostructures -Red Oak* [online] available from <http://www.triumphgroup.com/companies/triumph-aerostructures-vought-red-oak/capabilities/wings> [04 June 2015]

Tudor, A. J. (ed.) (1968) *Symposium on the Mechanical Reliability of Turbo-Machinary Blading*. 'Bird Ingestion Research at Rolls Royce'. held April at Derby and District College of Technology

UIUC (2015) *Airfoil Coordinates Database* [online] available from <http://m-selig.ae.illinois.edu/ads/coord_database.html#G> [17 June 2015]

Vlot, A. and Gunnink, W. (2001) *Fiber Metal Laminates: An Introduction*. Netherlands: Springer Netherlands

Vries, T.J. and Vermeeren, C.A.J.R. (1995) *R-Curve Test Data: 2024-T3, 7075-T6, GLARE 2 & GLARE 3.* Netherlands: TU Delft

Walvekar, V. (2007) *Birdstrike analysis on leading edge of an aircraft wing using a smooth particle hydrodynamics bird* model [online] MSc dissertation. Wichita State University. available from < http://soar.wichita.edu:8080/bitstream/handle/10057/3339/t10048_Walvekar.pdf?sequence=3 > [29 October 2014]

Wilbeck, J. (1977) *Impact Behaviour of Low Strength Projectiles*. US: Wright-Patterson Air Force Base

Zarei, H. (2008) *Experimental and Numerical Investigation of Crash Structures using Aluminium Alloys*. Germany: Cuvillier Verlag

Zhu, S., Tong, M., Wang, Y. (ed.) (2009) *50th AIAA/ASME/ASCE/AHS/ASC Structures, Structural Dynamics, and Materials Conference*. 'Experiment and Numerical Simulation of a Full-Scale Aircraft Windshield Subjected to Bird Impact'. held May 4-7 at California: AIAA

Appendix 1

Paper	Year	Software					Bird modeling				Bird								Load case					
		LS-DYNA	PAM-CRASH	ABAQUS	DYTRAN	other	Pressure load	Lagrange	Eulerian/ALE	SPH	Mass	Velocity [m/s]	Geometry				Dimensions [mm x mm]	Density [kg/m³]	Plate	Leading edge	Fan blade	Windshield	other
													cyl	hem	elp	spr							
[100]	2011			x				x			2 lb/4 lb	55-125	x	x					x			x	
[15]	2011			x				x			4 lb	175		x									upper cap
[140]	2011			x					x		32 g/4 lb	100-200		x					x				stiffened panel
[125]	2011	x			x			x		x	8 lb	129	x	x			268 x 134	924		x			
[143]	2011			x					x		32 g/4 lb	100-225		x			208 x 118	950	x	x			preloaded plate
[40]	2011			x					x		4 lb	100/150		x				938	x	x			
[83]	2010	x						x	x	x	1.92 kg	75-116		x			300 x 100	941	x	x			
[99]	2010			x				x			2 lb/4 lb	83-125	x	x								x	pitot probe
[183]	2010		x							x	4 lb	162		x			200 x 120	944		x			belly pod
[42]	2010				ANSYS					x	4 lb	78-182		x			208 x 120	930-970	x				
[145]	2010	x						x	x	x	4 lb	116	x					938				x	
[186]	2010	x								x	1.5 lb	75		x			138x92/164x82	950			x		
[124]	2010			x				x			4 lb/2.7 kg	100-146		x			228 x 114	938		x			
[147]	2010			x					x		0.45 kg/4 lb	100/150		x				938	x	x			
[97]	2010	x						x			4 lb	100-200		x			228 x 114	950				x	
[137]	2010	x							x	x		103-300	x			x			x		x		
[184]	2009	x								x	2.2 lb	100			x						x		propeller spinner
[165]	2009	x						x		x	0.18 kg	115	x				100 x 50		x				
[190]	2009				RADIOSS					x				x									helicopter blade
[98]	2009			x				x			2 lb	180	x				180 x 90	801					pitot probe
[119]	2009	x			x			x		x	8 lb	129	x	x			268 x 134	950		x			
[121]	2009				x			x			8 lb	129	x							x			
[122]	2009				x			x			8 lb	129	x				268 x 134	950		x			
[181]	2009		x							x	4 lb	170		x			208 x 118		x	x			
[36]	2009	x							x	x	1 kg	95		x				950	x				
[35]	2009	x						x			4 lb	225		x			228 x 114	934	x		x		
[105]	2009	x						x		x	1.5 lb	80		x							x		
[120]	2009			x				x						x						x			
[123]	2009			x				x			4 lb	116		x			228 x 114	938	x	x			
[189]	2009		x							x	4 lb	150		x			224 x 112	990					radome
[81]	2009			x				x			4 lb	95-105		x			228 x 114	938	x			x	
[5]	2008		x							x	4 lb				x					x			
[104]	2008	x						x					x								x		
[116]	2008				x			x			8 lb	129	x				268 x 134	950		x			
[117]	2008	x			x			x	x	x	8 lb	129	x	x			268 x 134	950		x			
[78]	2008				x			x	x		8 lb	135	x					950		x			
[49]	2008		x							x	4 lb	75-200	x	x				950	x	x			stiffened panel
[169]	2008	x								x		100/160		x						x			
[168]	2008	x								x	1kg/4 lb	95/180		x				950	x	x			
[196]	2008	x						x			8 lb	80-160	x				168 x 134	950	x				
[188]	2008		x							x	4 lb	64	x				180 x 120	900				x	
[180]	2008		x							x	4 lb			x			208 x 118		x	x			
[34]	2008	x						x			4/6/8 lb	225	x	x	x		various	934	x		x		

Appendix 2

Longitudinal Tensile Failure Mode at time = 0.0054 sec for Bird Impact at 116 m/s

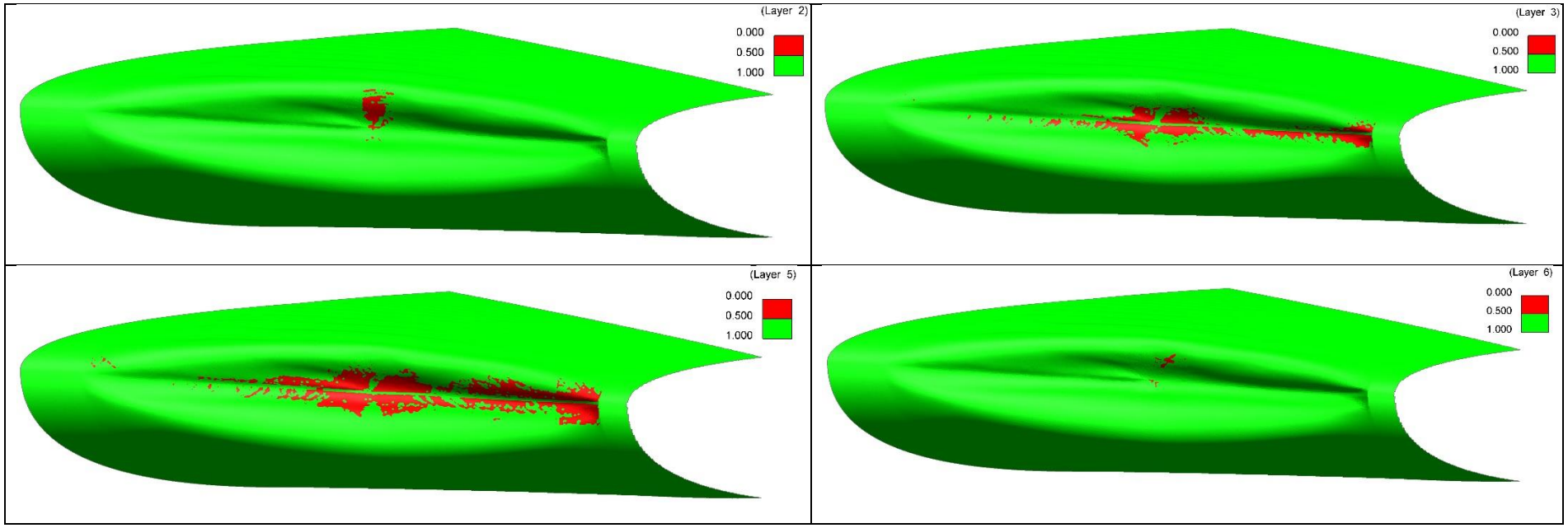

Appendix 3

Transverse Tensile Failure mode at time = 0.0054 sec for bird impact at 116 m/s

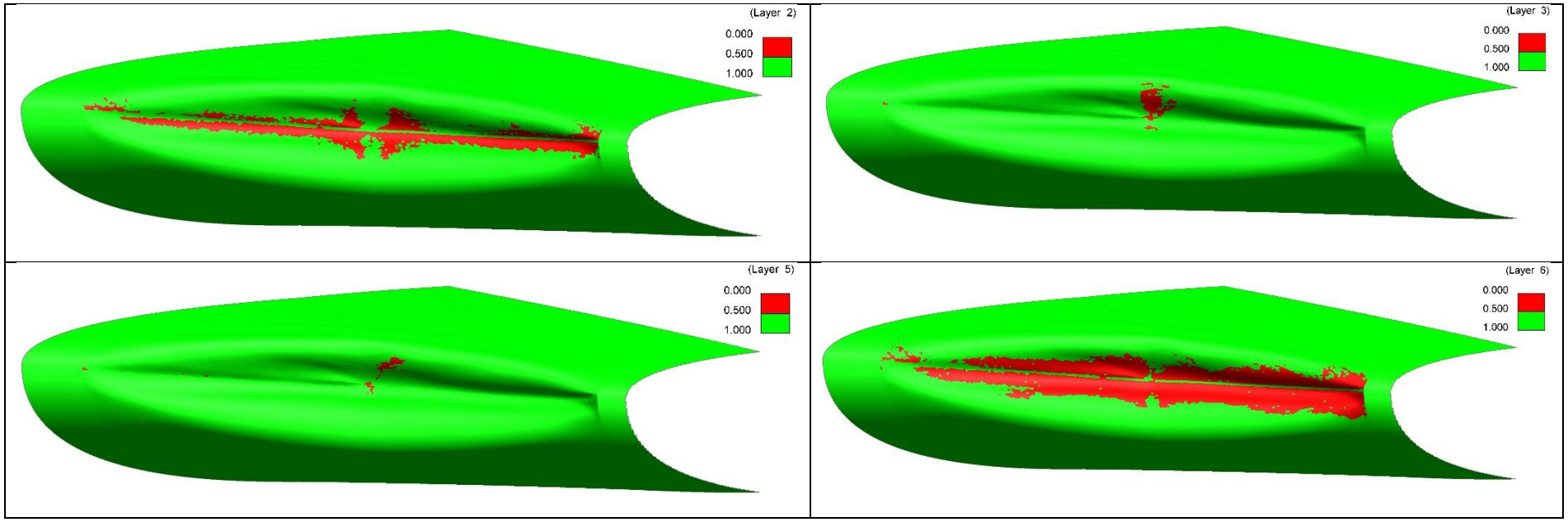

Appendix 4

Transverse Compressive Failure mode at time = 0.0054 sec for bird impact at 116 m/s

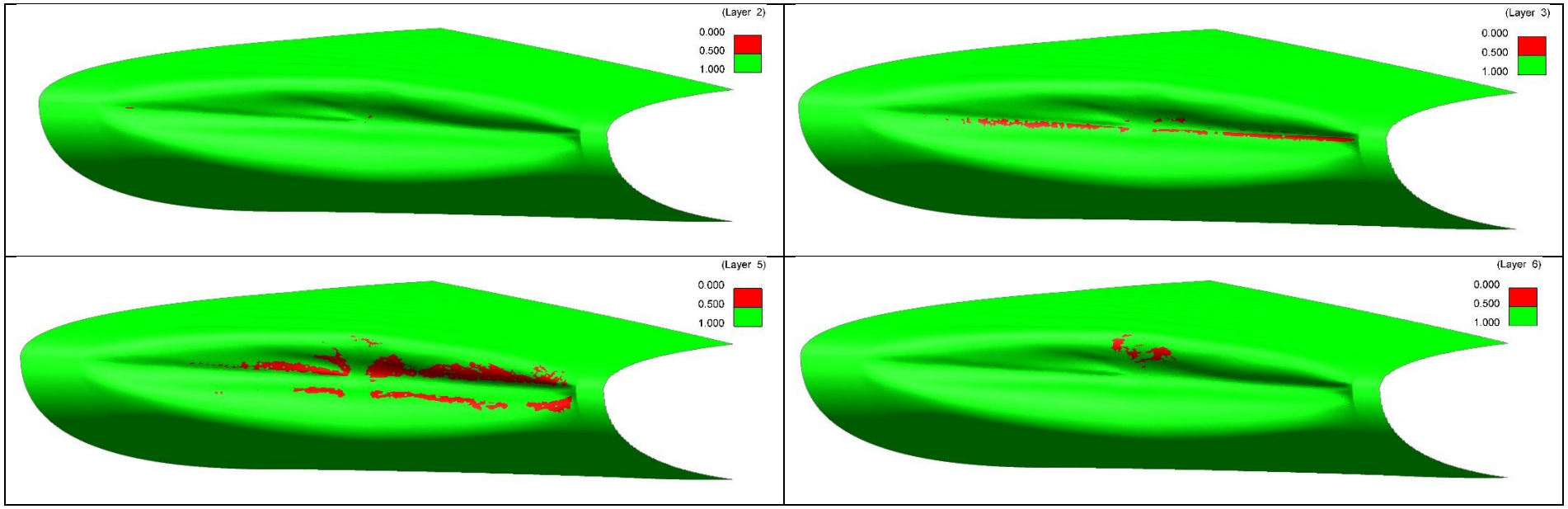

Appendix 5

Longitudinal Tensile Failure Mode at time = 0.0054 sec for Bird Impact at 129 m/s

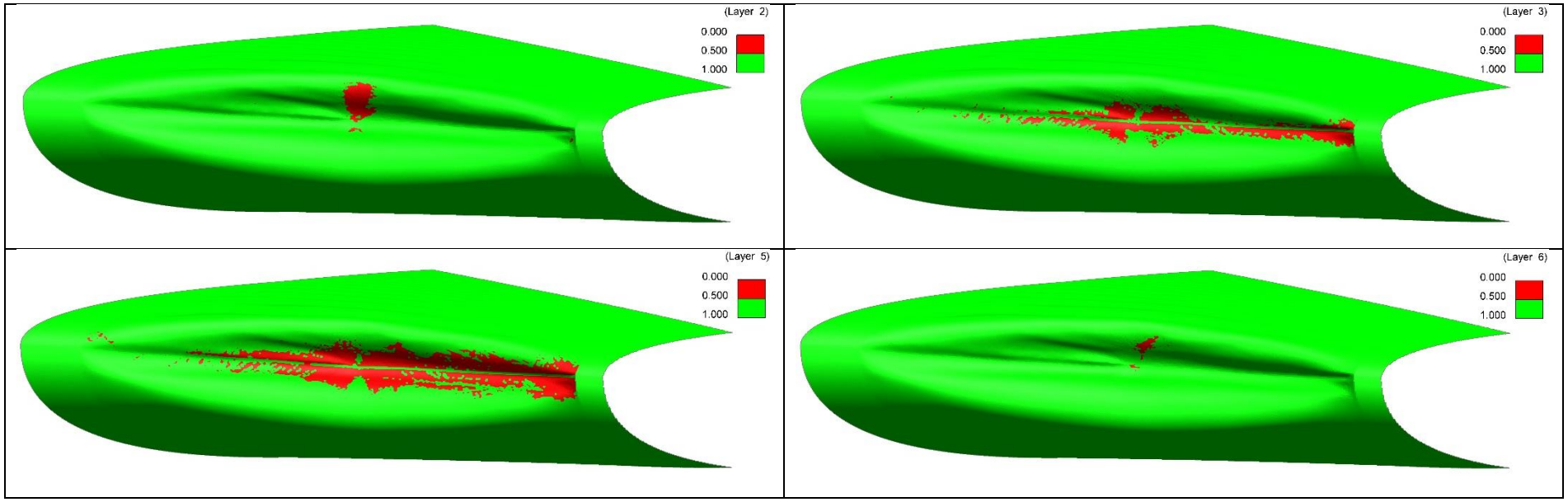

Appendix 6

Transverse Tensile Failure Mode at time = 0.0054 sec for Bird Impact at 129 m/s

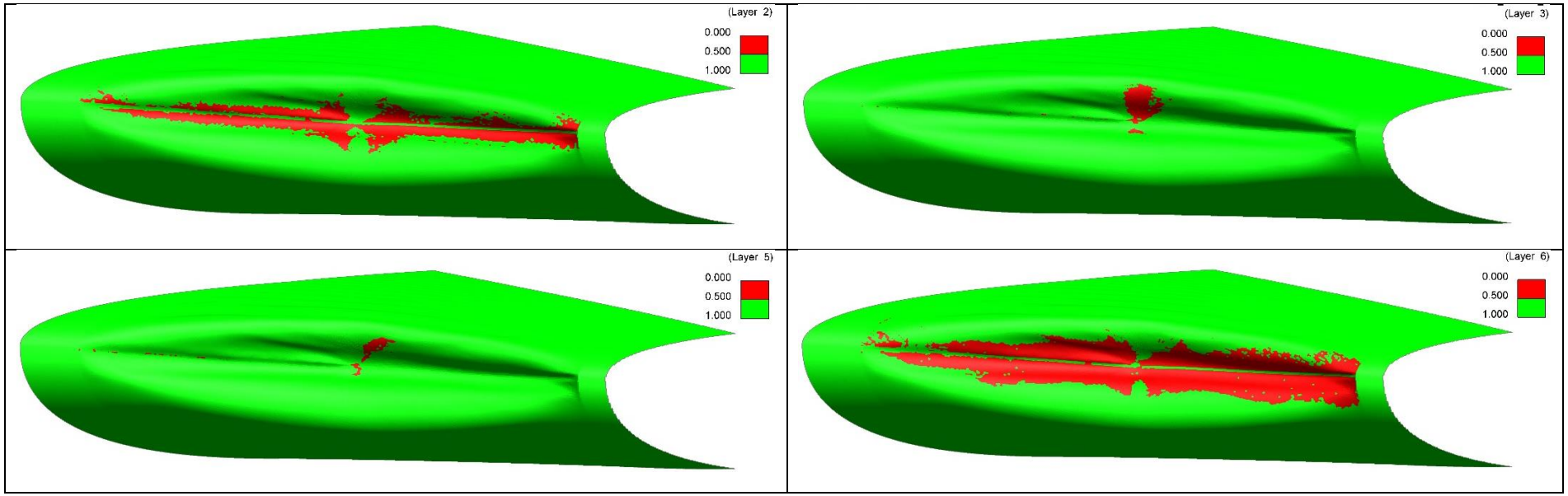

Appendix 7

Transverse Compressive Failure Mode at time = 0.0054 sec for Bird Impact at 129 m/s

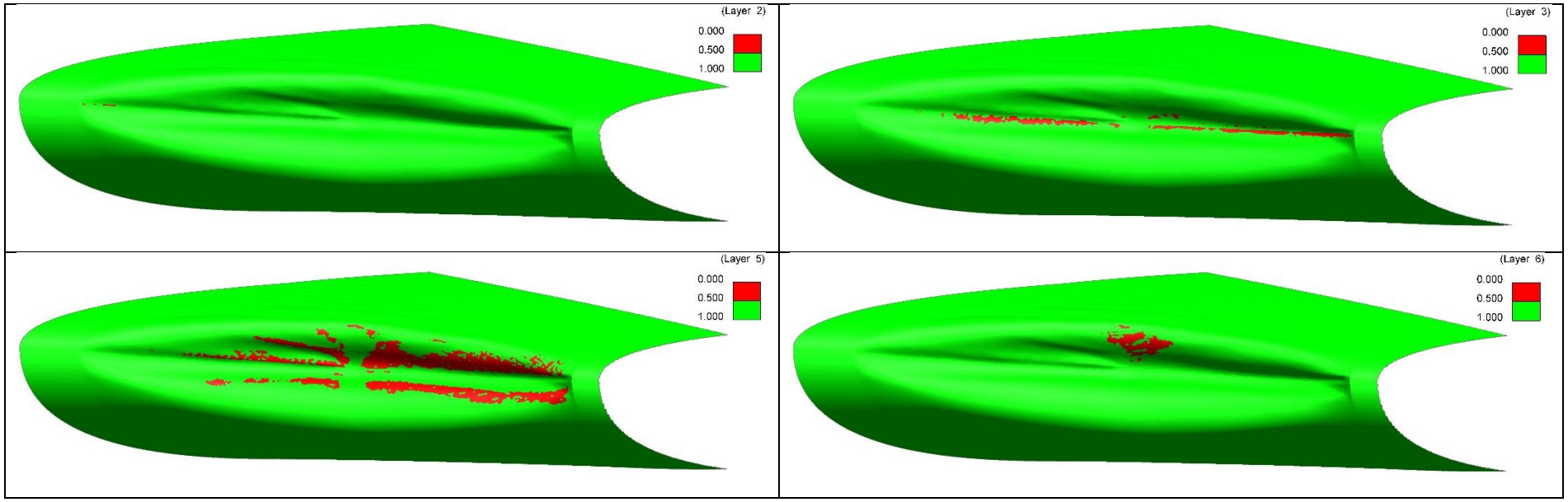

Appendix 8

LSDYNA Code for Bird Impact at 116 m/s

```
$ =============
$ CONTROL cards
$ =============
$
*CONTROL_CONTACT
     0.0      0.0        0        1        1        1        0        0
       0        0        0        0      0.0        0        0        0
*CONTROL_ENERGY
       2        1        2        2
*CONTROL_HOURGLASS
       4    5.0E-2
*CONTROL_SHELL
    20.0        1       -2        0        2        2        0        1
     0.0        0        1        0        0
*CONTROL_SPH
       0        0      0.0        3        0        0      0.0      0.0
       0        0        0        0        0        0        0
*CONTROL_TERMINATION
   1.4E-2        0      0.0      0.0      0.0        0
*CONTROL_TIMESTEP
     0.0     0.67        0      0.0-8.2128E-7        0        0        0
$
$
$ ==============
$ DATABASE cards
$ ==============
$
*DATABASE_BNDOUT
   6.0E-7        3        0        1
*DATABASE_ELOUT
   6.0E-7        3        0        1
*DATABASE_GLSTAT
   6.0E-7        3        0        1
*DATABASE_MATSUM
   6.0E-7        3        0        1
*DATABASE_NODFOR
   6.0E-7        3        0        1
*DATABASE_NODOUT
   6.0E-7        3        0        1      0.0        0
*DATABASE_RCFORC
   6.0E-7        3        0        1
```

```
*DATABASE_SLEOUT
   6.0E-7       3       0       1
*DATABASE_BINARY_D3PLOT
   6.0E-4       0       0       0       0
*DATABASE_BINARY_D3THDT
   6.0E-7       0
*DATABASE_EXTENT_BINARY
       0       0       7       1       0       0       0       0
       1       0       0       0       0       3       2       0
       0       0     0.0       0       0       0     ALL     ALL
       0       0       0
$ $
$ ====================
$ MAT (Material) cards
$ ====================
$
*MAT_NULL_TITLE
SPH_NULL
       1   9.5E-10 -9.974E-2    1.0E-3      0.0      0.0      0.0      0.0
$
*MAT_JOHNSON_COOK_TITLE
AluminiumAlloy
       2    2.7E-9   28000.0   73000.0     0.33      0.0      0.0      0.0
    369.0    684.0     0.73    8.3E-3      1.7    775.0    294.0    1.0E-5
     0.0      0.0      0.0      0.0      0.0      0.0      0.0      0.0
     0.0      0.0      0.0      0.0      0.0
$
*MAT_COMPOSITE_DAMAGE_TITLE
Fiberglass
       3    1.9E-9   53200.0    9300.0    9300.0      0.0      0.0      0.0
   5495.0    5495.0    3121.0       0.0      0.0        0
     0.0      0.0      0.0      0.0      0.0      0.0
     0.0      0.0      0.0      0.0      0.0      0.0      0.0
    75.0    725.0     75.0     75.0      0.0      0.0      0.0      0.0
$
$
$
$ ========================
$ EOS (Eqn of state) cards
$ ========================
$
*EOS_LINEAR_POLYNOMIAL_TITLE
SPH_LINPOLY
       2      0.0    2323.0    5026.0   15180.0      0.0      0.0      0.0
     0.0      0.0
```

```
$
$
$
$ =============
$ SECTION cards
$ =============
$
*SECTION_SPH
       2       1.2       0.2       2.0       0.0       0.0       0.0
$
$
$
$ ==========
$ PART cards
$ ==========
$
*PART_COMPOSITE
$HMNAME COMPS       1Part_1
FiberMetalLaminate
       1         2       1.0       1.0       0.0         0         0         0
       2       0.3       0.0         0
       3     0.125       0.0         0
       3     0.125      90.0         0
       2       0.3       0.0         0
       3     0.125      90.0         0
       3     0.125       0.0         0
       2       0.3       0.0         0
$
*PART
$HMNAME COMPS       2SPH

       2         2         1         2         0         0         0         0
$
$
$ =============
$ CONTACT cards
$ =============
$
*CONTACT_AUTOMATIC_NODES_TO_SURFACE_ID
       1BIRD2WING
       2         1         4         3         0         0         1         1
     0.0       0.0       0.0       0.0       0.0         0       0.0       0.0
     0.0       0.0       0.0       0.0       0.0       0.0       0.0       0.0
       0       0.0         0       0.0       0.0         0         0         0
     0.0         0         0         0         0         0       0.0       0.0
```

```
      0       1      0.0      0.0                    0.0       0
$
$
$
$ =========
$ SET cards
$ =========
$
*END
```